Springless Electromagnetic Vibration Energy Harvesters

by

Mohamed Bendame

A thesis
presented to the University of Waterloo
in fulfillment of the
thesis requirement for the degree of
Doctor of Philosophy
in
Systems Design Engineering

Waterloo, Ontario, Canada, 2015

I hereby declare that I am the sole author of this thesis. This is a true copy of the thesis, including any required final revisions, as accepted by my examiners.

I understand that my thesis may be made electronically available to the public.

Abstract

The abundance of environmental kinetic energy combined with advances in the electronics and MEMS industries have opened a window of opportunities for the design and fabrication of self-powered, battery independent, low-power electronic devices. Kinetic energy harvesting, the process that captures vibrations from the environment or surrounding systems and converts them into electrical power, offers the prospects of unlimited power for such systems. Vibration energy harvesters (VEHs) are vibration-based micro-power generators that utilize mechanical oscillators to capture ambient vibration energy and convert it into electrical power using one of three main transduction mechanisms, electromagnetic, electrostatic, or piezoelectric.

A key feature of VEHs is their ability to harvest maximum environmental vibration energy from low amplitude and low frequency vibrations from a wide spectrum of frequencies. Traditional VEHs use linear mechanical oscillators as their harvesting element and are tuned to harvest environmental vibrations at resonance frequency present within the application environment. These VEHs are usually designed to harvest energy from high frequency vibrations in a narrow band in the vicinity of the natural frequency of the mechanical oscillator, and outside this narrow band of frequencies their output power is significantly reduced. In environments where ambient vibrations are random and only available at low frequencies, conventional harvesters prove to be ineffective.

Although such devices are capable of generating power from vibrations with frequencies close to their resonance frequency, the need for harvesters that can harvest energy from broadband vibration sources has become an interesting research topic in recent years. To overcome the limitations associated with traditional vibration energy harvesters, nonlinear phenomena, such as hardening and softening nonlinearities, magnetic levitation, and impact have been sought as a solution to broadband vibration energy harvesting. In this thesis we aim to address this challenge by investigating a new architecture of an electromagnetic vibration energy harvester, the electromagnetic "Springless" vibration energy harvester (SVEH). The new architecture differs from traditional harvester as it uses a double-impact oscillator as its harvesting element as opposed to the linear model.

Experimental results show that the new SVEH is capable of harvesting vibration energies with frequencies as low as $5\,Hz$ and amplitudes as low as $0.05\,g$ in a frequency band of about $8\,Hz$. The harvester generates maximum output power of 12 mWatt from vibrations with amplitude of 0.5 g and an optimal load of $3.6\,\Omega$. Experimental results also show that the "nonlinear" center frequency of the harvester is not constant, as in the case of conventional harvesters, but depends on the amplitude and frequency of the external vibrations and whether the harvester is operated in the vertical or horizontal position. Experimental as well as the numerical frequency response curves of the SVEH also show the existence of hardening nonlinearity in the horizontal configuration and softening nonlinearity in the vertical configuration in the system. The hardening effect allows harvesting of energy in the high frequency spectrum, about 25 Hz and a bandwidth of 7 Hz, while the softening effect allows harvesting at the lower end of the frequency spectrum, which is around 5 Hz and a bandwidth of 8 Hz.

Models of the SVEH in the vertical and horizontal configurations were developed and nonlinear numerical and analytical methods were used to analyze the system to gain a deeper understanding of the system's behavior. The experimental data is then used to validate the models.

The harvester's ability to harvest vibration energy from low frequency ($\leq 25Hz$) and low amplitude vibrations ($\leq 0.5g$) in a wide band ($\geq 5Hz$) is one of the unique features of the SVEH demonstrated in this work.

Acknowledgements

In the name of GOD the most Gracious the most Merciful.

I would like to express my sincere gratitude to Prof. Eihab Abdel-Rahman, my supervisor, for his guidance, contributions in the development of my research, without his help and support, it would have been impossible for me to accomplish this work. I will always be indebted to him for giving me the opportunity to pursue a PhD, and for introducing me to the nonlinear world of mathematics and the field of energy harvesting. My sincere thanks to Dr. Mostafa Solaiman for his help with FEA analysis and suggestions to improve the harvester's magnetic transducer and for taking the time to read my thesis and provide useful and constructive feedback.

I would like to thank Prof. Glenn Heppler, Prof. Kann Erkorkmaz and Prof. Bryan Tripp, for serving on my dissertation committee.

I am also grateful to my wife Amal and our children Younus, Yasmine and Adam for their, sacrifice, patience, understanding, and for all the support they provided me during the PhD years, I will be forever indebted to them and will never repay them.

I would like to thank all the grad students in the Energy Harvesting group, in particular Bassam Tunker for his help with the experimental work.

Last but not least, I would like to thank my mother from the bottom of my heart, and I pray to GOD to protect her always. She has been a beacon of light that lights my way, and I pray that her light will continue to shine as long as I live. She will always be in my heart.

Table of Contents

List of Tables

List of Figures

Chapter 1

Introduction

This chapter is divided into four sections, the first section gives a general overview about energy harvesting and highlights some of difficulties associated with conventional vibration energy harvesters. The motivations behind this research and its objectives are provided in the second and third sections, and a thesis outline is given at the end of the chapter.

1.1 Energy Harvesting

Energy harvesting, or energy scavenging, is an emerging technology that strives to extract energy from ambient sources and convert it into electrical energy by direct energy conversion techniques [1, 2, 3]. The diagram, shown in Figure 1.1, depicts the four main elements of an energy harvesting system. A source of ambient energy, such as solar, wind, thermal, and kinetic, provides the energy to be harvested. The energy harvesting module consisting of a micro-power generator that captures and transforms ambient energy into electrical energy. The power management circuitry conditions and stores the harvested power. The harvested power is then delivered to a load in the form of a low-power electronic device.

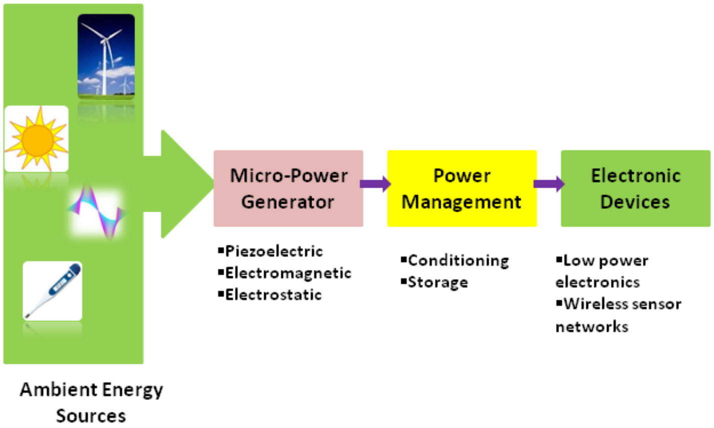

Figure 1.1: Energy harvesting process

Energy exists in various forms almost everywhere in the environment surrounding us. It can be found in the form of solar, wind, thermal, and kinetic energy. Technologies associated with solar and wind energies have made great strides over the last few years. Solar panels and wind turbines have become a familiar sight in our daily life and have become a major source of alternative and clean energy. However, with advances in the electronics and MEMS industries, which led to the development of low-power electronic systems, another source of energy that has attracted the attention of the research community in recent years is ambient kinetic energy [4, 5].

Sources of ambient vibrations can be found in numerous applications including common household appliances (such as fridges, washing machines, microwave ovens, laptops etc...), industrial plant equipments, moving structures such as automobiles, airplanes, and structures such as buildings and bridges [6]. The low-power consumption of small scale electronic devices combined with the abundance of vibration energy and the need for autonomous electronic goods made vibration based energy harvesting a potential alternative source of energy to replace or complement batteries [5]. A range of wireless devices with different amplitudes of power consumption and typical battery life are shown in Table 1.1 [7].

Device Type	Power Consumption	Duration
Smartphone	1 W	5 h
MP3 Player	50 mW	15 h
Hearing aid	1 mW	5 days
Wireless sensor	100 μW	Lifetime
Cardiac pacemaker	50 μW	7 years
Quartz watch	5 μW	5 years

Table 1.1: Selected battery-operated systems

To tap into this unlimited source of energy, Several academic and commercial research groups have been involved in the analysis and development of vibration energy harvesters (VEHs). VEHs are micro-power generators that capture and convert vibration energy into electrical energy. The conversion process is accomplished using one of three main transduction mechanisms, electrostatic, electromagnetic, and piezoelectric, and their choice depends on the type of the application and the environment of their deployment. A full description of the three transduction mechanism is given in chapter 2. The voltage generated by these micro-power generators is in AC form, hence conditioning is required to convert it into DC voltage. Voltage conditioning is achieved using a rectifier circuit, usually a bridge diode or MOSFET rectifier as shown in Figure 1.2. As the harvested energy is low and might not be used right away, energy storage devices are needed to accumulate the energy for intermittent use. Capacitors and super capacitors are usually used as storage devices for the energy harvester.

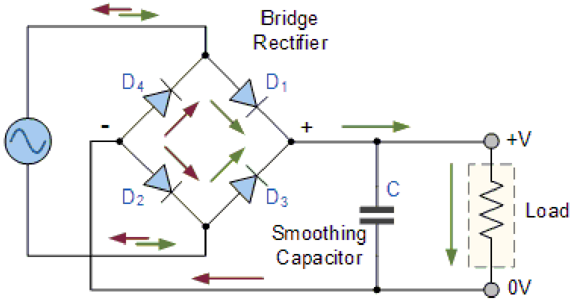

Figure 1.2: Full-wave bridge rectifier

Vibration energy harvesters are classified as resonance and non-resonance based harvesters. In the resonance-based approach, the mechanical oscillator is a single-degree-of-freedom (SDOF) oscillator designed to be in resonance with the environmental vibration to maximize the harvested energy [5, 6]. In this type of design, the natural frequency of the harvester, which depends on the stiffness and mass of the mechanical oscillator, is often chosen to coincide with the frequency of the environmental vibration. In the early literature, the vast majority of mechanical oscillators used in vibration energy harvesting are of the resonance type. They are usually designed to maximize the coupling between the mechanical system and the transduction mechanism and depends entirely upon the characteristics of the environmental vibration. The non-resonance based approach is the new trend in vibration energy harvesting, and its main objective is to explore nonlinear phenomena, such as hardening and softening nonlinearities, impact, and different geometries of structures used in the design of VEHs to overcome some of the challenges, such as low power density and narrow frequency bandwidth, associated with the resonance-based harvesters.

1.2 Motivation

As stated earlier, advances in the IC and micro-electronics technologies reduced the size and power consumption of electronic devices significantly. The power needs for many of these devices, such as wireless sensors, biomedical implants, portable and wearable electronic devices require only few to hundreds of milliwatts to operate[1, 8]. At the same time a large number of applications where these devices are used are either placed in remote locations or in areas that are not easily accessible. Most, if not all, of these low-power systems rely heavily on electrochemical batteries as a source of power. Modern battery technologies offer a relatively high specific energy density at a low cost. However, the drawback to battery power is that they have a limited lifespan and they constantly need to be recharged or replaced. For certain applications, such as wireless sensing, and remote monitoring, replacing batteries or recharging them can be expensive, challenging, or impossible at times. Examples include biomedical implants, wireless sensor networks intended for long durations, and systems that are physically remote [9]. Another serious problem with batteries is the fact that they contain hazardous chemical materials that are harmful to the environment if not recycled. In Canada, for instance, over 600 million primary consumer batteries were used in 2007 and about 90% of them end up in landfills [10].

The low-power electronics design trends combined with self-sustainability needs presented an opportunity for researchers to seek alternative ways to power such devices in order to eliminate or reduce dependency on batteries. One promising avenue to achieve this goal is to exploit ambient vibration energy sources to provide an environmentally friendly and a durable source of energy. Vibration energy harvesting technology has been making significant strides over the last few years as it aims to provide a continuous and uninterrupted source of power for low-power electronic devices and wireless sensors. While the idea of converting environmental vibration energy into electrical energy has been used before, advances in micro-electronics and low power consumption of silicon-based electronics and sensors have given it an added significance.

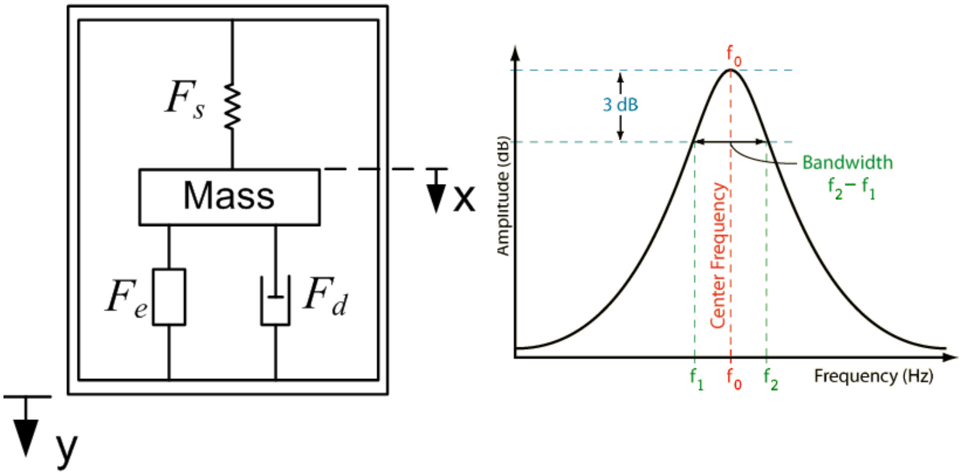

Figure 1.3: Linear vibration energy harvester and corresponding resonance phenomena

A number of vibration energy harvesters (VEHs) have been proposed over the last few years and most of them are resonance-based energy harvesters [11, 12, 13]. These implement a single degree-of-freedom linear spring-mass-damper as the harvesting element as show in Figure 1.3. In this setup, the seismic mass moves under the influence of base excitation supported by a spring. The oscillator attains maximum velocity, and thus input kinetic energy, in a frequency band close to its natural frequency. While these types of energy harvesters are capable of generating electrical energy with output power on the order of few milli-Watts [14, 15], their natural frequency must be tuned to match the frequency of ambient vibrations. The limitation to this approach is that the generator is, by definition, designed to work at a single frequency. A high Q-resonance to limit energy losses means a very limited practical bandwidths over which energy can be harvested. If the resonant frequency does not match the ambient vibration frequency, output power of the generator drops significantly. In some applications the frequency of the environmental vibration is known before the harvester is designed and fabricated, in such cases the harvester can be built with appropriate resonance characteristics. However, in other situations, the frequency is not known or might change over time, therefore, frequency tuning of the harvester is not always possible [6]. Another challenge that faces linear VEHs is that ambient vibrations are distributed over a wide spectrum of frequencies, with significant predominance of low frequency components [16], which means that building linear VEHs to harvest low frequency vibrations can be an onerous task.

Due to these challenges, there has been a great deal of research to realize low frequency, self-tuning, and wideband VEHs. To overcome these limitations, many researchers have followed different approaches by exploiting the properties of nonlinear phenomena. Over the past few years there has been a number of research papers that demonstrated the efficacy of nonlinear systems to overcome modern challenges in vibratory energy harvesting [17]. To date, strategies to widen the frequency bandwidth include:

- Use of active and passive frequency tuning techniques.
- Use of an array of mechanical oscillators with different resonant frequencies. The oscillators are designed to resonate at different environmental frequencies to enhance the harvester's bandwidth.
- Introduction of mechanical stoppers (impact) to limit the harvester's displacement and abruptly change its stiffness (hardening).
- Introduction of nonlinear stiffness (mechanical and magnetic), such as hardening and

softening, in the design of the harvester and exploit some of the frequency widening properties of nonlinear systems.

In this work we propose a new architecture to address the aforementioned challenges of limitation of frequency bandwidth, and harvesting low frequency vibrations, encountered in linear VEH, namely the "Springless" vibration energy harvester (SVEH). In this design, the harvester uses a double-impact oscillator as the harvesting element. The oscillator consists of a seismic mass comprising four magnets placed in a ferromagnetic cage that moves freely (not connected to springs) between two end limiters (springs) along a linear guide. The nonlinearities due to impacting in the "Springless" vibration energy harvester are exploited to enable wideband and low frequency energy harvesting.

1.3 Objectives

The main objectives of this research can be summarized as follows:

- Implementation of a non-resonance based vibration energy harvester to realize a low frequency (5 to 25 Hz) and broadband vibration energy harvester (VEH) capable of harvesting low vibration energy from the surrounding environment.
- Develop and simulate nonlinear models of the SVEH in two configurations, horizontal and vertical.
- Testing and validation of the SVEH in the horizontal and vertical configurations.
- Use of nonlinear methods, namely shooting and averaging, to analyze the model.

1.4 Outline

This work is organized in seven chapters. The first chapter gives a general overview of energy harvesting and the research motivations and objectives. Literature review of existing vibration energy harvesters and their applications, with a focus on electromagnetic and nonlinear harvesters, will be presented in chapter 2.

In chapter 3, we describe the new SVEH architecture, in particular we model and analyze its magnetic field and investigate how it interacts with the coil. In chapters 4 and 5 we develop models of the VEH in the horizontal and vertical configurations, and identify their regions of operations. Numerical and experimental results of the two configurations are presented, analyzed, and discussed. In chapter 6, we present experimental results of an earlier prototype of the harvester to show limitations associated with other coil configurations. Results are analyzed, limitations identified, and recommendations for best design are made. In chapter 7, a summary of the results of this research and future work will be presented.

Chapter 2

Background

In this chapter we review vibration energy harvesting and the different types of vibration energy harvesters (VEHs) that have been proposed over the years. A brief overview of the three main transduction mechanisms used in vibration energy harvesting is given along with a detailed analysis of electromagnetic vibration energy harvesting. Examples of applications where vibration energy harvesting has been used along with examples of commercial vibration energy harvesters will be presented. We will examine the current state of the art and the ongoing challenges preventing a breakthrough of vibration energy harvesting technology, and survey different strategies that have been proposed for the design of wideband vibration energy harvesters.

2.1 Literature Review

Environmental vibration energy, also referred to in the literature as kinetic energy, is ubiquitous, freely available, and comes from various sources, both human-made and natural

[18, 19]. These include transportation, such as rail, aviation, and highway traffic; machinery at adjacent facilities; structures such as buildings, bridges and construction work; and human vibrations such as walking, blood pressure and heart beat. Table 2.1 [20] lists sample sources of vibration energy according to the magnitude of the frequency and acceleration of the fundamental vibration mode.

Vibration Source	Acceleration (m/s^2)	Mean Frequency (Hz)
Car engine compartment	12	200
Base of a 3-axis machine tool	10	70
Blender casing	6.4	121
Dryer	3.5	121
Microwave Oven	2.5	120
Laptop CD	0.7	75
HVAC System	0.2-1.5	60

Table 2.1: Magnitude and frequency of sample vibration sources

2.1.1 Transduction Mechanisms

The principle behind vibration energy harvesting is the displacement of a moving mass or the mechanical deformation of some structure inside the energy harvesting device. This displacement or deformation can be converted into electrical energy by one of three main transduction mechanisms; electromagnetic, electrostatic, and piezoelectric as shown in Figure 2.1 [14]. A mechanical system is required to couple the environmental vibration to the transduction mechanism. Relative displacement is used in electromagnetic and electrostatic transducers while deformation is used in piezoelectric transducer. In the next section, the underlying principles that are the basis of vibration energy harvesting are outlined, and a brief comparison of the three transduction mechanisms, piezoelectric, electrostatic and electromagnetic is provided.

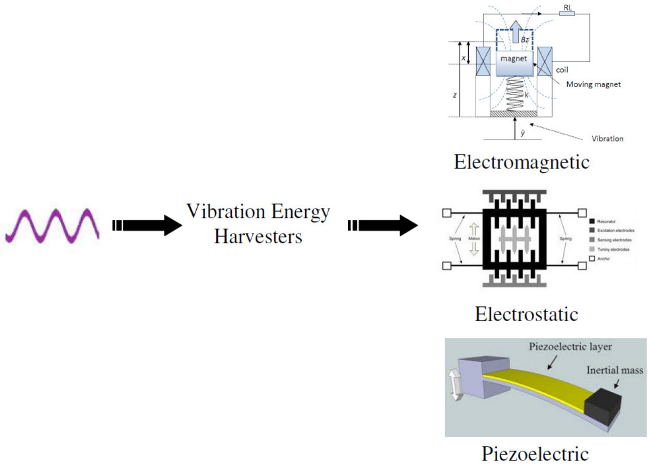

Figure 2.1: Vibration energy harvesting transduction mechanisms

Piezoelectric Piezoelectric materials are materials that deform when subjected to differences in electrical potential or alternatively, produce potential difference when subjected to input mechanical deformation. The piezoelectric effect is used by piezoelectric harvesters to converts mechanical strain into electric current or voltage. Piezoelectric materials are found in a variety of forms, such as single crystal, piezoceramics, and thin or thick films [21]. In piezoelectric energy harvesting from vibration, a mass is suspended by a beam, with a piezoelectric layer on top of the beam. When the mass is subjected to external vibrations, the piezoelectric layer is mechanically deformed and a voltage is generated.

The most common energy harvesting piezoelectric systems are cantilever structures that are mainly designed to operate at their resonance frequencies [22, 23]. Such structures (unimorph or bimorph cantilevers) are popular because they enable relatively high stress levels on the piezoelectric material while minimizing the dimensions of the devices [24]. A typical setup of the piezoelectric vibration energy harvester is shown in Figure 2.2.

A simplified piezoelectric energy harvester can be modeled by a coupled spring-mass-damper system depicted in Figure 2.3, where M refers to the seismic mass, C to the structural damping coefficient, K_e the stiffness of the beam carrying the piezoelectric material, α and C_0 stand for the force factor and clamped capacitance of the piezoelectric insert. A piezoelectric vibration energy harvester can be modeled by the following system

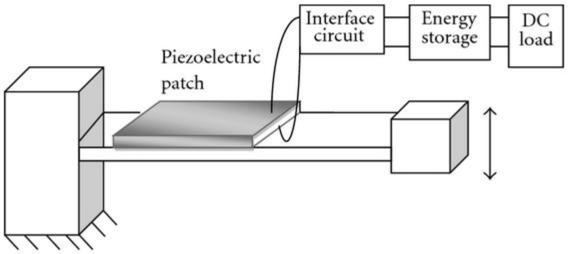

Figure 2.2: Piezoelectric Harvester Schematic

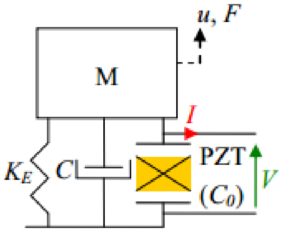

Figure 2.3: Simplified Schematic of a Piezoelectric Harvester

of differential equations:

$$\begin{aligned} M\,\ddot{u} + C\,\dot{u} + K_e\,u &= F - \alpha\,V \\ I &= \alpha\,\dot{u} - C_0\,\dot{V} \end{aligned} \tag{2.1}$$

where u, F, V and I respectively represent the displacement, applied force, piezoelectric output voltage and current flowing out of the piezoelement. The energy analysis of such a system over a time range $[t_0; t_0 + \tau]$ is obtained by integrating in the time domain the product of the equation of motion by the velocity and the product of the electrical equation by the voltage:

$$\begin{aligned} &\frac{1}{2}\,M[\dot{u}]_{t_0}^{t_0+\tau} + C\int_{t_0}^{t_0+\tau} \dot{u}^2\,dt + K_e\,[(u)^2]_{t_0}^{t_0+\tau} = \int_{t_0}^{t_0+\tau} F\,\dot{u}\,dt - \alpha\int_{t_0}^{t_0+\tau} V\,\dot{u}\,dt \\ &\int_{t_0}^{t_0+\tau} V\,I\,dt + \frac{1}{2}\,C\,[V^2]_{t_0}^{t_0+\tau} = \alpha\int_{t_0}^{t_0+\tau} V\,\dot{u}\,dt \end{aligned} \tag{2.2}$$

From Equation (2.2), it can be shown that the converted energy is represented by the time integral of the product of the voltage by the speed (with a multiplying coefficient α), which can be decomposed into the electrostatic energy on the piezoelectric element and energy transferred to the electrical system [25].

Electrostatic The basis of electrostatic generator is the variable capacitor. Electrostatic vibration energy harvesters produce electrical energy by employing two conductive plates moving relative to one another that are electrically isolated by air, vacuum, or dielectric insulator to form a capacitor. Electrostatic transduction is based on electrostatic conversion and relies on capacitive transducers in which the electrical energy stored in variable capacitors is increased by changing the capacitance value of such capacitors through vibration [26]. The work done against the electrostatic force between the charged electrodes of the capacitor is part of the harvested mechanical energy. Electrostatic generators can be classified into three types, i.e. in-plane overlap, Figure 2.4 (a)[11], which varies the overlap area between electrode fingers, in-plane gap closing, Figure 2.4 (b), which varies the gap between electrode fingers and out-of-plane gap closing, Figure 2.4 (c), which varies the gap between two large electrode plates. The electrostatic energy harvester can be modeled by

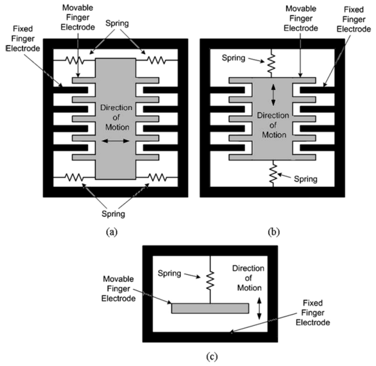

Figure 2.4: Electrostatic generators: (a) in-plane overlap (b) in-plane gap closing and (c) out-of-plane gap closing

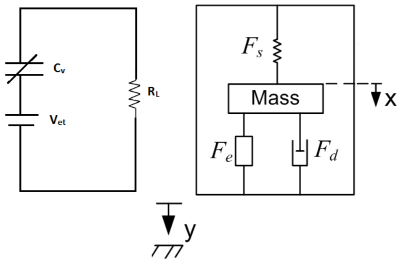

Figure 2.5: Simplified Schematic of a Piezoelectric Harvester

a coupled mechanical spring-mass-damper system and an electrical oscillator with a variable capacitor as depicted in Figure 2.5, and the electrostatic harvester model equations are derived using Kirchhoff's law and Newton's law of motion. The system's equations are usually defined as [27]:

$$
\begin{aligned}
V_{et} &= V_{RL} + V_C \\
m\,\ddot{x} &= -m\,\ddot{y} - F_s - F_e - F_d
\end{aligned}
\tag{2.3}
$$

where V_{RL}, F_s, F_d, and $\ddot{y}$ are the voltage across the load resistor, the spring force, the damping force, and the input vibration acceleration, respectively. The voltage across the variable capacitor V_C and the electrostatic force F_e are given by [27]:

$$
\begin{aligned}
V_C &= \frac{q}{C_v} \\
F_e &= -\frac{1}{2}\,\frac{d}{dx}\,\frac{q^2}{C_v}
\end{aligned}
\tag{2.4}
$$

where C_v is the variable capacitor capacitance defined as:

$$
C_v = \frac{C_0}{1 - \frac{x}{g}} \tag{2.5}
$$

where C_0 is the nominal capacitance and x is the distance separating the capacitor electrodes.

Electromagnetic Electromagnetic transduction mechanism is based on Faraday's law of electromagnetic induction which states that: "an electrical current will be induced in any closed circuit when the magnetic flux through a surface bounded by the conductor changes", and explains the conversion from mechanical to electrical energy and vice versa. According to the law of induction, a voltage is induced across the transducer's coil, and the generated electrical energy is supplied to an attached load while some is partly dissipated as heat in the coil's resistance. Electromagnetic vibration energy harvesters consist of permanent magnets that provide a strong magnetic field and a coil used as a conductor. Either the permanent magnet or the coil is fixed to the frame while the other is attached to the inertial mass as shown in Figure 2.6. The relative displacement caused by the external vibration makes the transduction mechanism work and induces an electromotive force (emf) across the coil terminals. According to the Faraday's Law, the induced voltage, or emf, across the coil terminals is proportional to the time rate of change of the magnetic flux within the coil [15];

$$V = \frac{d\phi}{dt} \tag{2.6}$$

where ϕ is the linkage magnetic field given by;

$$\phi = \mathbf{B}\,\mathbf{A} \tag{2.7}$$

where $\mathbf{A}$ is the area vector and $\mathbf{B}$ is the magnetic flux density vector. For a coil that consists of N loops, the total induced voltage would be N times as large, and Equation (2.6) becomes;

$$V = N\,\frac{d}{dt}(B\,A\,\cos\theta) \tag{2.8}$$

Differentiating Equation (2.8) with respect to time we obtain:

$$V = N\left(\frac{dB}{dt}\,A\,\cos\theta + B\,\frac{dA}{dt}\,\cos(\theta) + B\,A\,\sin(\theta)\frac{d\theta}{dt}\right) \tag{2.9}$$

From Equation (2.9), the harvested energy depends on the magnetic field density $\mathbf{B}$ provided by the permanent magnets, the cross-section area $\mathbf{A}$ of the coil, and the angle θ between the magnetic field $\mathbf{B}$ and the normal to the coil's cross section area $\mathbf{A}$. It is desired to maximize the output voltage by operating with an angle $\theta = 0$ in order to maximize the constant field density $\mathbf{B}$. In this case, the first and third terms of Equation (2.9), where $\cos(\theta)$ appears, will be suppressed and the equation reduces to:

$$V = N\,B\,\frac{dA}{dt} \tag{2.10}$$

The coil's shape is rectangular with length l and width x, during operation the length l remains constant and the width x, where the magnetic flux is active, varies with respect

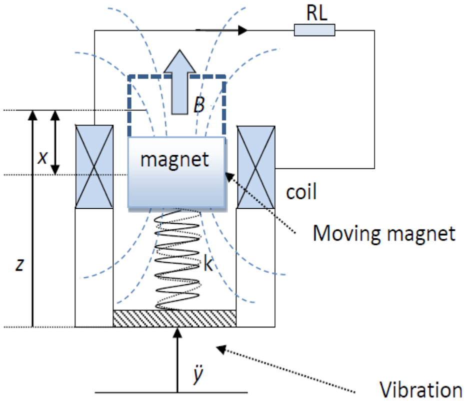

Figure 2.6: Electromagnetic Vibration Energy Harvester

to the moving mass. This reduces Equation (2.10) further to the following:

$$V = N\,B\,l\,\frac{dx}{dt} \tag{2.11}$$

From Equation (2.11), the voltage V induced across the coil terminals depends on the strength of the magnetic field density B, the coil length l, and the relative velocity between the magnetic field and the coil.

2.1.2 Transduction Mechanisms Comparison

The use of the three transduction mechanisms in vibration energy harvesting depends on the type of application where they are to be used. It has been argued in review articles that piezoelectric energy harvesting is the most widely researched harvesting method due to its ease of use, high voltage output, high power density, as well as relatively mature thin-film and think-film manufacturing methods. However, electromagnetic and electrostatic energy harvesters have specific advantages [13]. A summary of the advantages and disadvantages of the three main transduction mechanisms are provided in Table 2.2.

Induction	Advantages	Disadvantages
Electromagnetic	Self contained (requires no external supporting accruements) Can have reduced mechanical damping over piezoelectric converters, depending on configuration (i.e. if not cantilever-based) High ouput current	Voltage output levels can be rather low (hundreds of mV to $\approx$ 2V) Can require complex fabrication and assembly of multiple small components Performance is reduced significantly in micro scale Not easily compatible with microelectronics and MEMS
Electrostatic	Can be fabricated with existing silicon-based IC processes, and easy to integrate with microelectronics Can be miniaturised easily, including to MEMS-scale	May require relatively complex circuitry, in order to operate switches that are synchronized to the vibration Low output current External voltage source or pre-charged electrets is also necessary High output impedance
Piezoelectric	Self contained High output voltage Compatible with MEMS	High input impedence Low current Susceptible to fatigue over time and possible cracking due to the britle nature of piezoelectric materials

Table 2.2: A comparison of the advantages and disadvantages of the three main vibration conversion methods

2.1.3 Vibration Energy Harvesting Applications

A wide range of applications are targeted for vibration energy harvesters, including wireless sensor networks for structural health monitoring, embedded and implanted biomedical devices for medical applications, recharging the batteries of electronic systems, monitoring tire pressure in automobiles, powering unmanned vehicles, and running security systems in household conditions [28]. In the next subsections we will examine some applications where vibration energy harvesters have been used, along with some existing commercial harvesters.

Battery-less TV Remote Control: Many electronic devices such as TVs, DVDs, computer games, and other utilities, use battery powered remote controls. In every household one can find at least two or three remote controls, if not more. If all the remote controls were to be powered using vibration energy harvesting techniques, a great deal of batteries would not be needed, which would save the environment having to deal with a huge amount of hazardous waste. Arveni is a company that, designs, produces, and sells piezoelectric micro-power generators. In 2011, the company [29] developed a battery-less TV remote control, Figure 2.7, that uses kinetic energy from a push of a button on the remote control to generate enough electrical energy to change a TV channel, turn up the volume, or switch on/off the TV. In many hotels across North America the battery-less TV remote control is already in use.

Figure 2.7: Batteryless TV Remote Control

Induction Flashlight: The inductive flashlight, also known as Faraday or shake flashlight, is another application of mechanically powered devices. This design contains a linear electrical generator which charges a battery-like super-capacitor when the flashlight is shaken lengthwise. The linear generator consists of a sliding magnet which moves back and forth through the center of a coil of copper wire, when it is shaken. A current is induced in the loops of wire by Faraday's law of induction each time the magnet slides through, which charges a super-capacitor which is used instead of a rechargeable battery.

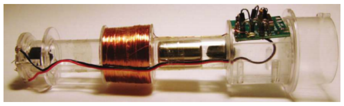

Figure 2.8: Induction flashlight

Self-Sustaining Power Faucet: Self-sustaining faucets, Figure 2.9, are designed to require no electricity or routine disposable battery replacement. A number of companies, such as ChicagoFaucets [30] and Toto EcoPower, have started implementing the idea of self-sustaining faucets in their products. Toto EcoPower products such as sensor faucets and flush valves are examples of such designs. These self-sustaining power systems use the flow of water to power the sensor that operate these electronic faucets. The water flow that spins the high-efficiency turbine converts the flow into electrical energy and produces enough power to operate the electronic faucet.

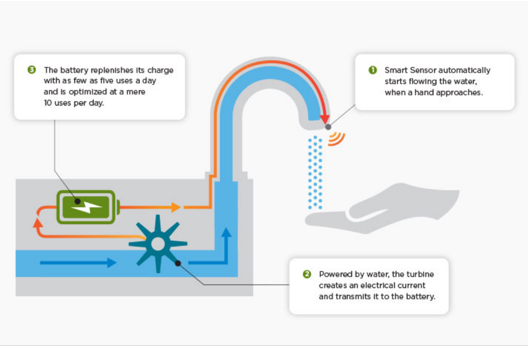

Figure 2.9: Self sustaining power faucet

Rechargeable Micro-Energy Cells: Another area where vibration energy harvesting is used is to recharge micro-energy cells to provide continuous supply to low-power electronic devices. Infinite Power Solutions, for instance, produces solid-state, rechargeable, thin-film micro-energy storage devices for embedded applications. Their products Micro-Energy Cells (MECs) come in four different sizes, the smallest is $12.7mm \times 12.7mm \times 0.17mm$, and are able to generate up $4.1V$ and a current of $15mA$. The MECs, see Figure 2.10 [31], can be recharged by different energy harvesting methods including, solar, RF, kinetic, and thermoelectric.

Figure 2.10: Thin-film Micro-Energy Cell

2.1.4 Commercial Vibration Energy Harvesters

A number of start up companies, specializing in the development and manufacturing of vibration energy harvesters, have established themselves as providers of perpetual source of energy harvested from ambient vibrations. Companies such as Perpetuum, EnOcean, MicroStrain, and Kinetron are just some examples.

Energy Harvester Powered Wireless Sensors: Wireless sensor networks (WSNs), due to their low power consumption, are one of the most attractive applications for vibration energy harvesting. Many companies are now producing WSNs powered by vibration energy harvesters. For instance, EnOcean GmbH [32], manufactures wireless sensors powered by energy harvesters. The ECO 200 for example, Figure 2.11, is a $29.3mm \times 19.5mm \times 7.0mm$ vibration energy harvester that is able to generate about 2 V and an energy of up to $210\mu J$ and is designed for use with radio modules produced by EnOcean. The ECO 200 is based on a linear resonator and is designed to operate at a high frequency $f = 868$ MHz. EnOcean energy harvesting solutions are also used to power devices such as wireless switches, wireless controllers, and wireless transceivers.

Figure 2.11: EnOcean Vibration Energy Harvester

Perpetuum Vibration Energy Harvesters: Perpetuum [33], specializes in engineering, producing and commercialization of electromagnetic vibration energy harvesting micro-power-generators to power autonomous wireless sensor and transmit data from remotely monitored sites. Perpetuum electromagnetic-energy harvesters convert unused mechanical energy from a plant where they are deployed to electrical energy via an oscillating magnetic mass which traverses across a fixed coil creating a varying amount of magnetic flux, inducing a voltage across the coil. To maximize power output, the harvester is mechanically tuned to an optimized resonant frequency present within the application environment.

Perpetuum Vibration Energy Harvester (VEH), shown in Figure 2.12, can generate a maximum power of 27 mW and output power of 5 V, or 24 mW and an output voltage of 8 V. The harvester comes in six off-the-shelf predefined frequency models: 25 Hz, 30 Hz, 50 Hz, 60 Hz, 100 Hz, and 120 Hz. Perpetuum harvesters are used as a power source for Wireless Sensor Nodes (WSNs) used for process monitoring and equipment condition-based monitoring in industrial environments. One certain application is to predict failure of rotating components on trains such as wheel bearings, gearboxes, etc. We note that as in the case of the EnOcean products, all the harvesters provided by Perpetuum operate at a predefined frequency.

Figure 2.12: Perpetuum vibration energy harvester

MicroStrain Energy Harvester: MicroStrain [34] designs and manufactures adaptive energy harvesting electronics for wireless sensor networks. The MagnetoInductive Vibration energy harvester (MVEH), Figure 2.13, designed to harvest low frequency vibrational energy inherent in machines and structures. The MVEH provides a regulated 3.2 VDC output at ≈ 4 mW from input vibrations of 200 mg amplitude when tuned from 15–60 Hz.

The frequency tuning of the harvester is accomplished by adjusting precision flexure elements, which resonate small coils around rare-earth magnets to create energy. The PVEH is a piezoelectric vibration energy harvester and provides a regulated 3.2 VDC output at ≈ 30 mW from input vibrations of 1.5 g amplitude when tuned to 1000 Hz.

Figure 2.13: Microtrain electromagnetic vibration energy harvester

Micro Generator with Ferrite Magnet: Kinetron [35] on the other hand specializes in rotary micro-power-generators. The micro generator shown in Figure 2.14 consists of a 14-pole resin bonded Sm2Co17 magnet and a claw pole stator that encloses a coil with 1140 windings at a resistance of 320 Ω. At a rotational speed of 15000 rpm an AC voltage with an amplitude of 7.8 V and a frequency of 1750 Hz is generated. At this speed the typical output power is 10 mW.

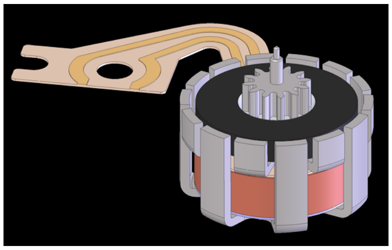

Figure 2.14: Kinetron electromagnetic micro-power generator

All of the examples mentioned in this section were realized using a linear, or resonance-based, vibration energy harvester. In this type of applications, when the resonant frequency of the energy harvester does not match the ambient frequency, the output power is reduced significantly. This limitation severely restricts the use of linear energy harvesters. To overcome this drawback, there has been in recent years an interest in designing harvesters that are self-tuning or possess a broadband. In the next section, we will examine strategies and techniques used to produce broadband vibration energy harvesters.

2.2 Electromagnetic Energy Harvesting

Electromagnetic vibration energy harvesters consist of mechanical oscillators and electromagnetic transducers. Typically, the mechanical oscillator is designed to have a magnet-coil arrangement, which move relative to each other in response to environmental excitations. In this arrangement, the variation in the magnetic flux, ϕ, through an electrical circuit causes an electric field. The flux variation can be realized with a moving magnet whose flux is linked with a fixed coil or with a fixed magnet whose flux is linked with a moving coil. The first configuration is preferred to the second one for two main reasons; fixed electrical wires are preferable to avoid damaging the usually fragile coil, and magnets are heavier than the coil which means more generated power. A simplified schematic of the electromagnetic energy harvester is shown in Figure 2.15.

Next we explore the modeling of electromagnetic vibration energy harvesters.

Damping in vibration energy harvesters comes from two main sources, mechanical and electrical energy losses. In the case of a linear electromagnetic vibration energy harvester, mechanical damping is usually approximated as viscous damping, and electrical damping is due to mechanical energy converted into electrical energy.

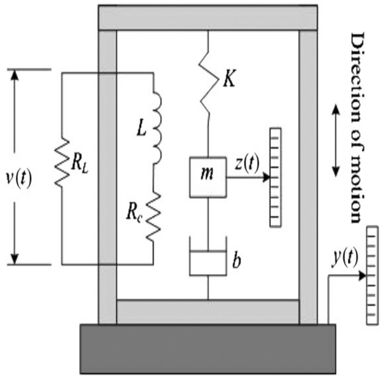

Figure 2.15: Schematic of an electromagnetic vibration energy harvester

Electrical Damping: When the mass moves inside the magnetic field, the current induced across the coil terminals creates a magnetic field that opposes the magnetic field of the magnets. The interaction between the two fields results in the electrical damping, or emf force, that opposes the motion of the seismic mass and is given by:

$$F_{em} = b_e\,\dot{x}, \tag{2.12}$$

where b_e is the electromagnetic damping. The emf results in the electrical power that is extracted from the mechanical oscillator

$$P_{em} = F_{em}\,\dot{x} = b_e\,\dot{x}^2. \tag{2.13}$$

This generated power is dissipated in a parasitic coil resistance R_p and consumed by the load resistance R_L, and is equal to;

$$P_{diss} = \frac{V^2}{R_L + R_p + j\omega L} \tag{2.14}$$

where L is the coil inductance. Equating the electrical power dissipated to that extracted from the oscillator gives

$$b_e\,\dot{x}^2 = \frac{V^2}{R_L + R_p + j\omega L} \tag{2.15}$$

Substituting Equation (2.6) in Equation (2.15) we obtain

$$b_e = \frac{1}{R_L + R_p + j\omega L}\left(\frac{d\phi}{dx}\right)^2 \tag{2.16}$$

Following the assumption that the coil inductance is negligible [36, 37] and assuming that the coil moves in a region of constant magnetic field density B, the electromagnetic damping coefficient can be expressed as;

$$b_e = \frac{(B\, l)^2}{R_L + R_p} \tag{2.17}$$

Mechanical Damping: Mechanical damping can be found from the open-circuit frequency-response curve of the harvester. The mechanical quality factor Q_m of a linear VEH is found from the two half-power cut-off frequencies,f_1 and f_2, and the center frequency $f_\circ$ of the its mechanical oscillator, and is given by:

$$\begin{aligned} Q_m &= \frac{f_\circ}{\Delta f} \\ &= \frac{\sqrt{m\, k}}{b_m} \end{aligned} \tag{2.18}$$

where $\Delta f = f_2 - f_1$. The mechanical damping coefficient is related to the quality factor by the given expression:

$$b_m = \frac{2\,\pi\, f_0\, m}{Q_m} \tag{2.19}$$

The VEH shown in Figure 2.15 can be described by a simple model that describes the dynamic interaction of the two relevant quantities: the seismic mass relative displacement with respect to the base $x(t)$ and the voltage V across its coil. The dynamics of the seismic mass is modeled by Newton's second law of motion as the second order differential equation::

$$m\,\ddot{x}(t) = -\,b_m\,\dot{x}(t) - F(x) - F_{em} - m\,\ddot{y}(t) \tag{2.20}$$

where $y(t)$ is the frame absolute displacement, $F(x)$ the spring's restoring force, F_{em} is the electromagnetic force due to the transduction mechanism, and b_m is the mechanical damping coefficient.

Substituting for F_{em} with Equation (2.12) in Equation (2.20), we obtain the equation of motion of the electromagnetic energy harvester,

$$m\,\ddot{x} + \,(b_e + b_m)\,\dot{x} + F = -m\,\ddot{y} \tag{2.21}$$

Setting the total damping to $b_t = b_e + b_m$, the total electromechanical damping ratio can be written as

$$\zeta_t = \frac{b_t}{2m\omega_n} \tag{2.22}$$

The total damping can also be expressed in terms of the quality factor

$$\zeta_t = \frac{1}{2Q} \tag{2.23}$$

2.2.1 Power Flow in Linear VEHs

The instantaneous dissipated power in the harvester is

$$P_{in} = b_t\,\dot{x}^2 \tag{2.24}$$

and the average input power into the harvester over one excitation period T is

$$(P_{in})_{Ave} = \frac{1}{T}\int_0^T b_t\dot{x}^2 dt = \frac{1}{T}\frac{\omega_n}{Q}m\int_0^T \dot{x}^2 dt \tag{2.25}$$

For a sinusoidal base excitation $y(t) = Y_\circ \cos(\omega\,t)$, the seismic mass displacement at resonance, $\omega = \omega_n$, is $x(t) = Y_\circ\,Q\,\cos(\omega_n\,t - \phi)$. Without a loss of generality, we can set the phase angle to zero $\phi = 0$ and write

$$\begin{aligned}(P_{in})_{Ave} &= \frac{1}{T_n} Y_\circ^2 \omega_n^3 Q m \int_0^{T_n} \sin^2(\omega_n\, t) dt \\ &= \frac{1}{T_n} Y_\circ^2 \omega_n^3 Q m \big[\frac{1}{2} t + \frac{1}{2\omega_n} \sin 2(\omega_n\, t)\big]_0^{T_n} \\ &= \tfrac{1}{2} Y_\circ^2 \omega_n^3 Q m \end{aligned} \tag{2.26}$$

Performance of energy harvester is typically evaluated in terms of base acceleration. Rewriting the input power in terms of the acceleration amplitude $A_\circ$, we obtain

$$(P_{in})_{Ave} = \tfrac{1}{2} Q A_\circ^2 \omega_n m \tag{2.27}$$

Similarly, the average power harvested over one at resonant excitation period T_n is

$$\begin{aligned}(P_{el})_{Ave} &= \frac{1}{T_n} \int_0^{T_n} b_e \dot{x}^2 dt = \frac{2}{T_n} \zeta_e \omega_n m \int_0^{T} \dot{x}^2 dt \\ &= \frac{1}{2T_n} \frac{Y_\circ^2}{\zeta_t^2} \zeta_e \omega_n^3 m \int_0^{T_n} \sin^2(\omega_n\, t) dt \\ &= \frac{1}{2T_n} \frac{\zeta_e}{\zeta_t^2} Y_\circ^2 \omega_n^3 m \big[\frac{1}{2} t + \frac{1}{2\omega_n} \sin 2(\omega_n\, t)\big]_0^{T_n} \\ &= \frac{\zeta_e}{4\zeta_t^2} Y_\circ^2 \omega_n^3 m \end{aligned} \tag{2.28}$$

or in terms of the acceleration amplitude $A_\circ$

$$(P_{el})_{Ave} = \frac{\zeta_e}{4(\zeta_e + \zeta_m)^2} A_\circ^2 \omega_n m \tag{2.29}$$

To determine the electric load ζ_e leading to maximum harvested power, we differentiate the electrical power $(P_{el})_{Ave}$ with respect to ζ_e and set the derivative equal to zero

$$\frac{dP_{el}}{d\zeta_e} = -\frac{m {A_\circ}^2 \omega_n (\zeta_e - \zeta_m)}{4(\zeta_e + \zeta_m)^3} = 0 \tag{2.30}$$

which results in the so-called ‘impedance matching’ condition $\zeta_e = \zeta_m$ for maximum harvested power. The impedance-matching condition corresponds to an input power at resonance of

$$(P_{el})_{max} = \frac{A_\circ^2 \omega_n m}{16\,\zeta_e} \tag{2.31}$$

which means that input power is split evenly between mechanical and electrical dissipation processes (damping). Using the voltage divider rule, the power delivered to the load can be written as

$$P_{Load} = \frac{A_\circ^2 \omega_n m}{16\,\zeta_e} \frac{R_L}{R_L + R_p} \tag{2.32}$$

We deduce that the maximum electrical power generated by the harvester depends on the seismic mass m, the magnitude $A_\circ$ of the input base excitation, the natural frequency ω_n of the oscillator, and the electrical damping ζ_e. Therefore, when designing a VEH one has to take into account all of these parameters and the constraints, such as the size and weight of the VEH, and the frequency of ambient vibration to be harvested.

Equation (2.32), shows that not all power generated by the VEH can be delivered into the load, some power is lost within the coil.

We define the power harvesting FoM as the ratio of the electrical power harvested to the mechanical power supplied, so that

$$FoM = \frac{(P_{el})_{Ave}}{(P_{in})_{Ave}} \tag{2.33}$$

substituting for $(P_{el})_{Ave}$ and $(P_{in})_{Ave}$ using Equations (2.29) and (2.27), we obtain

$$FoM = \frac{(B\,l)^2}{(B\,l)^2 + b_m\,(R_L + R_p)} \tag{2.34}$$

In the next section we examine applications where vibration energy harvesting technology has been implemented.

2.3 Broadband Vibration Energy Harvesting

Over the past few years vibration energy harvesting has attracted the attention of the research community as a potential source of power for low-power electronic devices. In the research literature, the first description of an inertial micro-power-generator was an electromagnetic vibration energy harvester presented by Williams and Yates in 1996 [38]. Since then, a great deal of research has been conducted in the area of vibration energy harvesting. Earlier works by Beeby, Glynne-Jones, Roundy [39, 40] and others focused on the implementation of linear oscillators that can harvest maximum energy at resonance. In this type of harvesters, the seismic mass of the VEH moves under the influence of base excitation supported by a spring. The oscillator attains maximum velocity, and thus input kinetic energy, when the harvester's natural frequency matches the frequency of environmental vibration. If the excitation frequency deviates from the harvester's natural frequency very little power is harvested.

Generator	ω (Hz)	Accel ($m\,s^{-2}$)	m (g)	Power (μW)
Beeby [15]	52	0.589	0.66	45
Glynne-Jones [39]	99	6.85	2.96	4990
Ching [41]	110	95.5	-	830

Table 2.3: Electromagnetic micro-power generators

Harvesters in this arrangement are designed to harvest environmental vibrations at a single frequency. While they are capable of generating electrical energy with output power on the order of few milli-Watts [15], their natural frequency must be tuned to match the frequency of ambient vibrations. However, in environments where ambient vibrations are distributed over a wide spectrum of frequencies, with significant predominance of low frequency components, these harvesters prove to be ineffective because of their high center frequencies and narrow bandwidth [42, 43, 12]. It is therefore impractical to use linear VEHs that have relatively high center frequency ($\geq 20Hz$) to harvest low frequency ($< 20Hz$) vibrations. Some of the harvesters that have been proposed over the years are listed in Table (2.3), a more comprehensive lists of electromagnetic energy harvesters can be found in [6]. We remark that the proposed harvesters have high frequencies and low power densities. For example, the VIBES harvester (first harvester in Table 2.3), which is an electromagnetic type harvester, has a center frequency of $52\,Hz$ and a maximum power of $45\mu W$. To address the issues associated with these type of harvesters, in recent years the attention has focused on the implementation of self-tuning and nonlinear methods to develop wideband vibration energy harvesters.

Nonlinear vibration energy harvesters use mechanisms to adjust or tune the resonant frequency of the harvester so that it matches the frequency of the ambient vibration and/or widen its bandwidth [44, 45, 46]. A number of approaches have been used for this purpose including nonlinear stiffness, resonant frequency tuning, mechanical stoppers and exploitation of nonlinear phenomena to widen the frequency bandwidth of the energy harvester. These approaches lead to three main types of nonlinear vibration energy harvesters, the Duffing, the array and the impact harvester. The Duffing type gets its name from the Duffing oscillator because its governing equation reduces to a Duffing equation. In this type of harvesters, the nonlinearity is added to the harvester either by using nonlinear springs or by introducing magnetic forces to alter the overall stiffness of the harvesting device. On the other hand, the impact harvester is realized using impact oscillators or mechanical stoppers to limit the seismic mass displacement. In impact harvesters, the overall stiffness of the system is a piecewise function, that results in a non-smooth system, due to the change in stiffness when impact occurs [47]. The third approach is the array harvester, which is resonant frequency tuning approach that attempts to achieved widband energy harvesting by employing an array of structures with different resonant frequencies [6]. In the next subsections we will present examples of vibration energy harvesters where some of the techniques were used to improve the frequency bandwidth of the harvester.

2.3.1 Duffing Oscillator

Duffing harvesters use mechanical oscillators with cubic and/or quadratic nonlinearities as the vibration energy harvesting element. In this type of harvesters, the nonlinearity is introduced in the harvester either by using nonlinear springs or by introducing magnetic forces to alter the overall system stiffness and make it appear as a nonlinear quantity in the system's model. The Duffing harvester can be classified in three categories: Hardening, bistable, and softening [48, 49, 50].

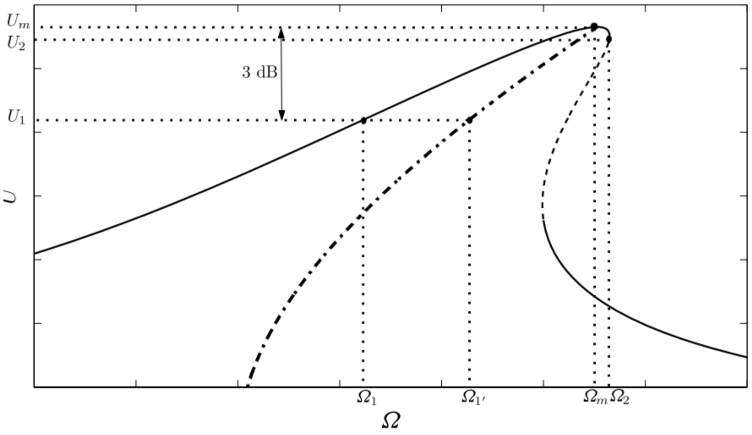

Figure 2.16: Frequency-response curve for a hardening system

Duffing harvesters with magnetic nonlinear stiffness are achieved by applying magnetic forces to alter the effective stiffness of the harvester. Barrow et al [51], proposed a harvester with nonlinearities added in the form of magnetic reluctance forces to the linear spring compliance. The frequency response curve of the harvester measured at frequencies between 20 and 60 Hz exhibits nonlinear characteristics usually seen in the response of nonlinear dynamical systems. We note the hysteresis band between the frequency up and down sweeps, the sudden jumps in the frequency response curve, and the emf reaching a peak value at the high end of the frequency spectrum before taking a significant fall, see Figure 2.17. Figure 2.18 shows the The harvester's waveform for an input excitation with frequency 32 Hz. We see from the figure the presence of two peaks that are attributed to the nonlinear compliance characteristics of the harvester. At this frequency the harvester achieved a maximum AC power of 100 mW. In chapter 4, see subsection 4.5.1, experimental and numerical waveforms of the proposed harvester exhibit similar characteristics.

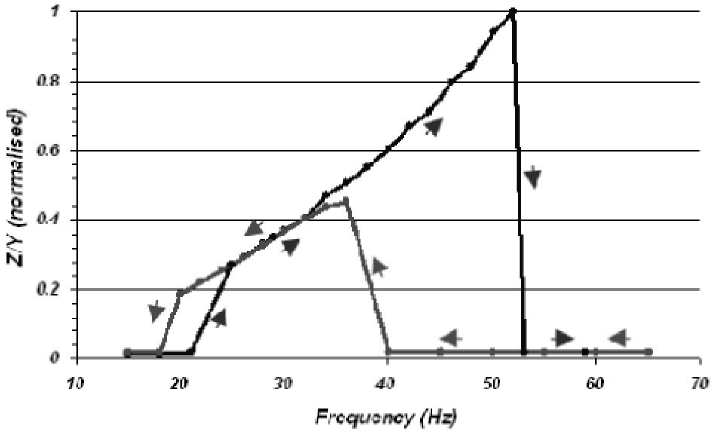

Figure 2.17: Frequency-response curve of harvester with nonlinear magnetic stiffness

In 2009, Mann et al [3], described the design and analysis of a novel energy harvesting device, Figure 2.19, that uses nonlinear magnetic forces to levitate an oscillating center magnet. They showed that intentionally introduced nonlinearity allows the linear resonance

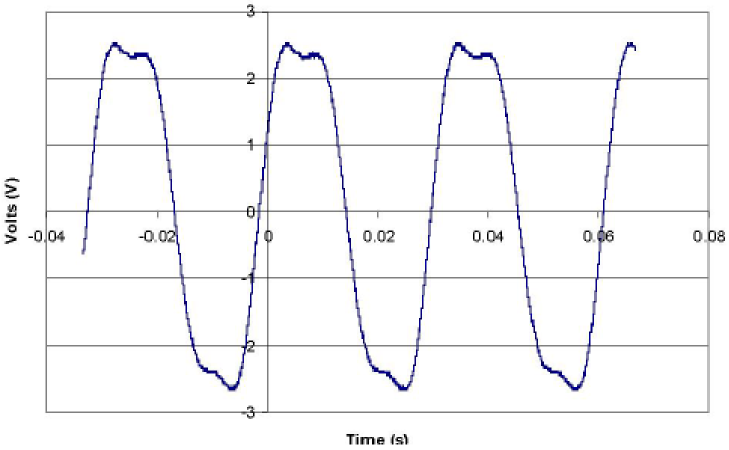

Figure 2.18: Waveform of harvester with nonlinear magnetic stiffness

to be tuned by simply changing the spacing between the upper and lower magnets. The added nonlinearity resulted in the governing equation for relative displacement of the magnetic mass reducing to the form of Duffing's equation. In particular, the authors showed that the introduction of nonlinear restoring magnetic levitation resulted in relatively large excitations over a wide range of frequencies.

Using a similar approach, Owens et al [52] presented a nonlinear vibration energy harvester that exploits the interaction between a moving magnet and a fix magnet to tailor the harvester's bistable potential well. Theoretical and experimental results reveal that the nonlinear generator with a bistable potential well can be used to broaden the frequency response of the harvester. The output power of the proposed harvester varied from 5 mWatt to 200 mWatt for input accelerations ranging from 5 to 10 m/s^2. The proposed harvester design resulted in the following frequency bandwidths; 1, 2, and 3 Hz for input accelerations between 5 and 6.5 m/s^2, and 2 Hz for 10 m/s^2 respectively. Analysis of the results, Figure 2.20, shows that engaging nonlinearity in the system results in relatively large oscillations

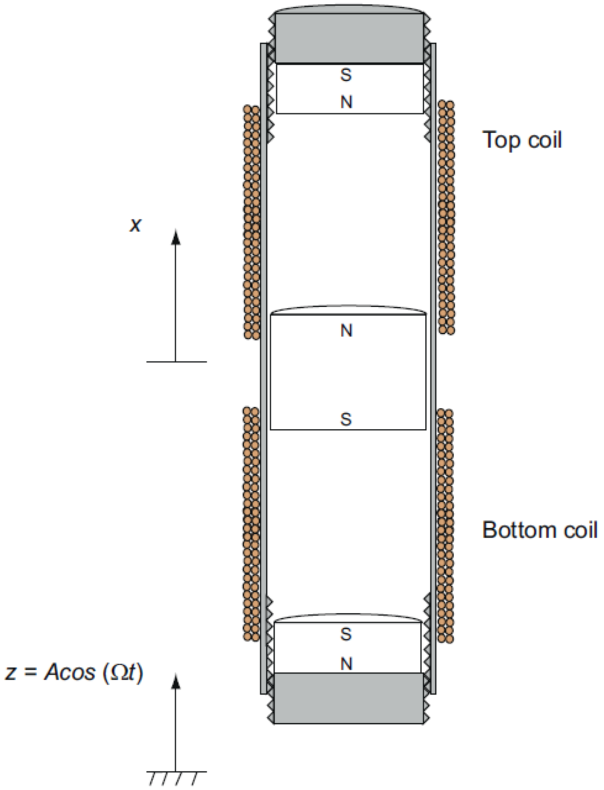

Figure 2.19: Schematic diagram of the magnetic levitation system

over a wider range of frequencies, thus potentially improving the ability to harvest energy under certain circumstances.

Duffing harvesters with nonlinear springs on the other hand, where the nonlinearity is usually defined as a cubic function of the displacement $x(t)$ given by Equation (2.35)

$$f(x) = k\,x(t) + \alpha\;x(t)^3 \tag{2.35}$$

where k is the spring's linear stiffness and α is the nonlinearity parameter, are modeled as a Duffing Equation given by;

$$m\,\ddot{x} + b\,\dot{x} + k\,x + \alpha\,x^3 = A_o\,\sin(\Omega\,t) \tag{2.36}$$

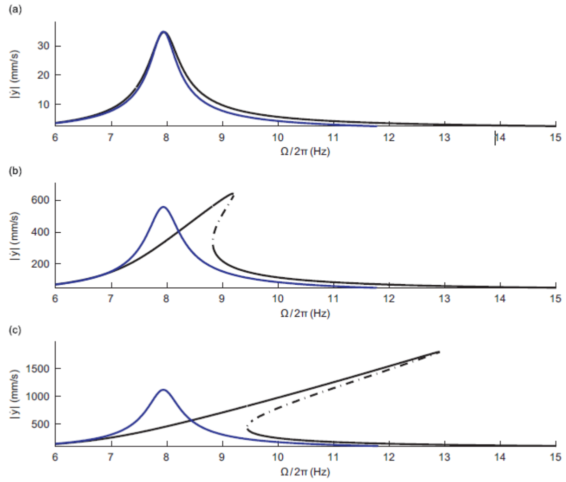

Figure 2.20: Frequency response curves of the magnetic levitation system for different base excitation amplitudes

The parameter α can be used to introduce hardening or softening type nonlinearities depending on whether the targeted vibrations frequencies are high or low. If the parameter $\alpha > 0$ there is hardening nonlinearity (hard spring) and when $\alpha < 0$ there is softening nonlinearity (soft spring).

Ramlan et al [53] investigated the hardening type nonlinearity that has the effect of shifting the resonance frequency of the harvester. This results in widening the frequency bandwidth over which power can be harvested. Using harmonic balance method and the backbone curve, it was shown that the harvester's bandwidth increases with the hardening nonlinearity parameter α, see Figure 2.21.

Nguyen et al, [48], also showed the potential benefits of nonlinear stiffness utilizing soft and hard springs in vibration energy harvesters. Their results, shown in Figures 2.22, showed that energy harvesters using nonlinear springs have wider bandwidth compared to energy harvesters with linear springs.

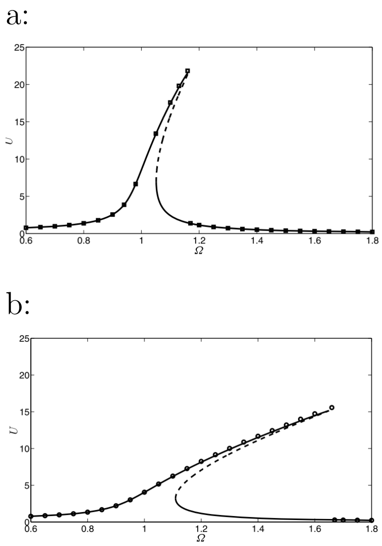

Figure 2.21: Frequency-response curves for a: $\alpha = 0.001$ and b: $\alpha = 0.01$

Further examples of Duffing type harvesters and nonlinear vibration energy harvesters can be found in reviews of recently published work [50, 54].

2.3.2 Impact Oscillator

It has been shown that impact harvesters increase the frequency bandwidth and output power of vibration energy harvesters [55, 56]. Impact harvesters use mechanical stoppers to restrict the seismic mass displacement and modify the overall harvester's stiffness from linear to a piecewise linear function. A typical setup of a vibration energy harvester with a mechanical stopper and its nonlinear stiffness are illustrated Figure 2.23.

Soliman et al [21] designed an electromagnetic energy harvester using a mechanical stopper as shown in Figure 2.23. The piecewise linear stiffness of the energy harvester is dominated by the changes of the spring stiffness during impact between the harvester and

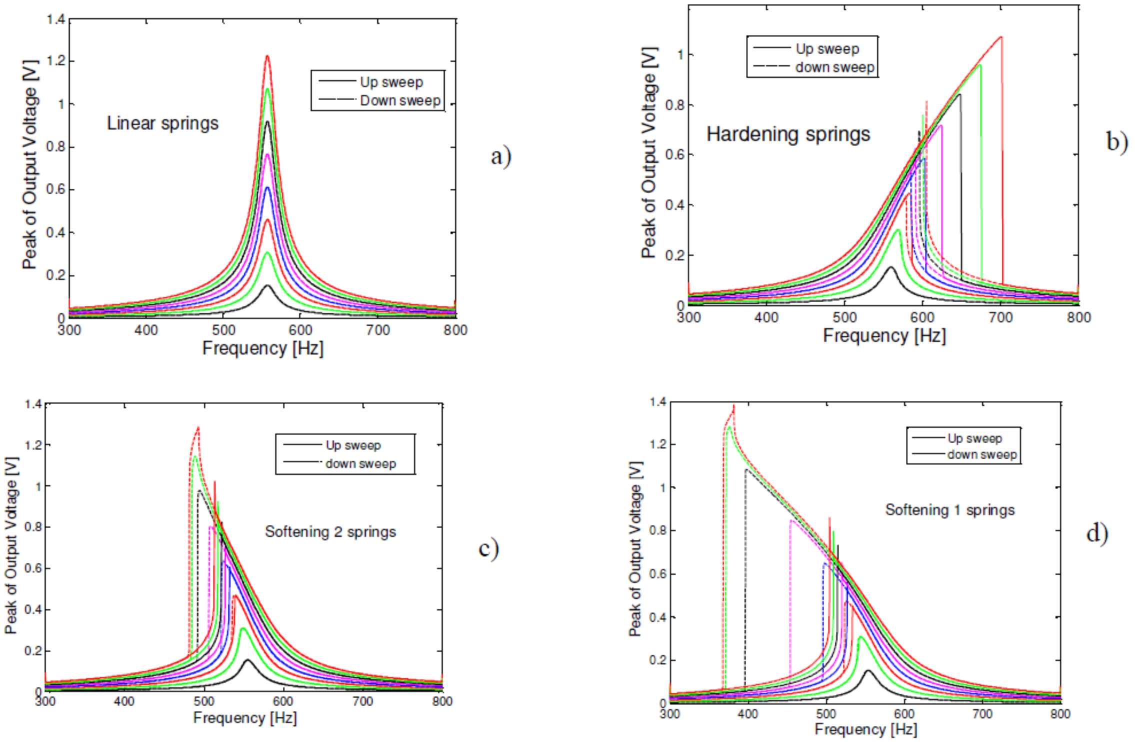

Figure 2.22: The frequency response curves for base acceleration amplitudes of 0.05 g, 0.10 g, 0.15 g, 0.20 g, 0.25 g, 0.30 g, 0.35 g and 0.40 g. a) linear springs b) hardening springs c) softening spring 2 d) softening springs 1

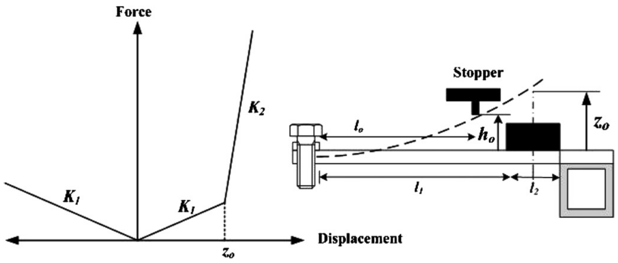

Figure 2.23: Schematic of a one stopper vibration energy harvester

the stopper. The one stopper vibration energy harvester improved the frequency bandwidth significantly compared to the linear type harvester as shown in Figure 2.24. Jacquelin et al [55] on the other hand presented an impact harvester that consisted of a box that enclosed two identical piezoelectric cantilever beams separated by a distance d from each other. A sliding mass impacts the tip of each beam causing the beams to deform. Each beam has its tip displacement limited by a stop between the beam and the box internal wall. The results shown in this study indicate that this type of harvester can widen the frequency bandwidth, however, the harvested power is in the μW range which is way too low.

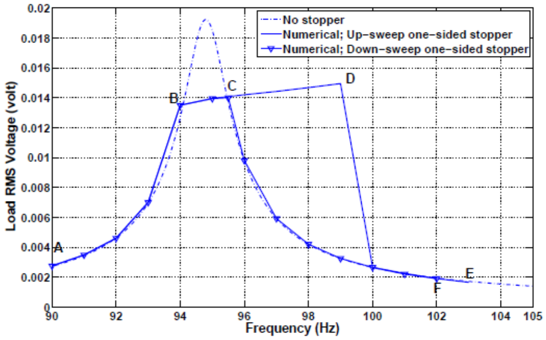

Figure 2.24: Frequency response curve of a one stopper vibration energy harvester

2.3.3 Array Harvester

Figure 2.25 shows a typical setup of an array harvester. These type of harvesters employ a series of mechanical oscillators with different center frequencies integrated in one energy harvesting device. Usually in this type of setup, a series of cantilever beams with varying length and center frequencies are employed [57]. The cantilevers are chosen in a way that all resonance frequencies are close to each other. The resonance frequencies are adjusted by tuning the geometry of each energy scavenger or by applying a proof mass. As long as the source vibration has dominant frequency within the band of the array, at least one of the beams will operate at its resonance frequency which results in maximum energy harvesting. Hence, the more beams are added to the array, the much bigger is the possible bandwidth [58]. In 2008, Sari et al [59] proposed a wideband vibration energy harvester

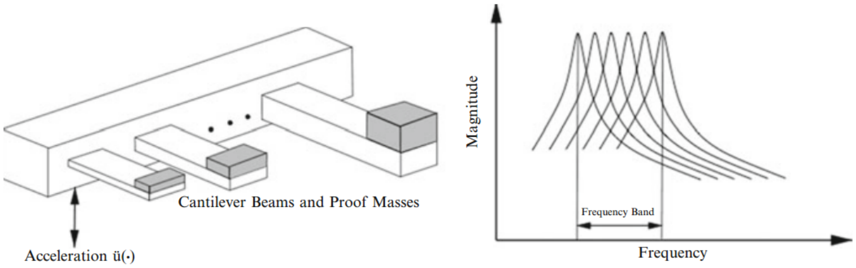

Figure 2.25: Frequency response curve of a one stopper vibration energy harvester

comprised of an array of oscillators made of cantilever beams. The cantilever beams were fabricated from three layers of parylene where coil turns are sandwiched in between and connected in series. The cantilevers and the coils move as a single body and oscillate with respect to a stationary magnet to generate power from environmental vibrations. The reported generator covers a wide band of external vibration frequencies as a result of implementing an array of oscillators with varying natural frequencies. The proposed harvester generated a reported power of 0.4 μW in a frequency band of 800 Hz. Even though the proposed harvester possess a wide band, its output power is significantly low and can only harvest power at very high frequencies between 4.5 and 5 kHz, which makes the harvester unsuitable for environmental vibrations that are mainly low frequencies.

To address the high frequency band issue encountered in the design of Sari, Challa et al proposed [5] a vibration energy harvester, Figure 2.27, with "autonomous" resonance

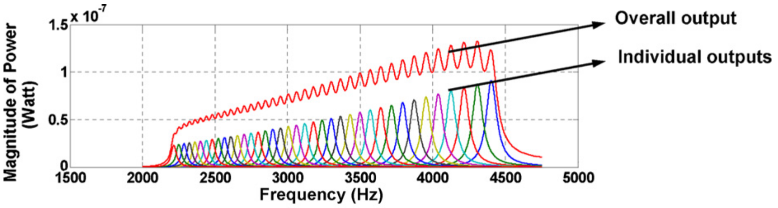

(a) 10 μm length increment

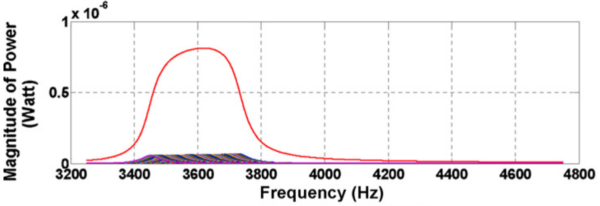

(b) 1 μm length increment

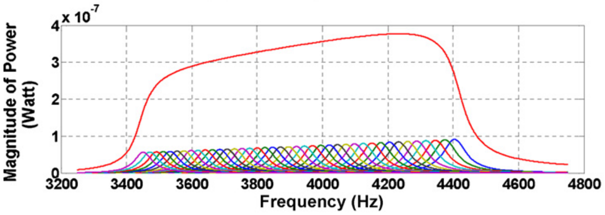

(c) 3 μm length increment

Figure 2.26: Frequency response curve of wideband vibration energy harvester with an array of cantilever beams

frequency tuning capability. In this design, a magnetic force is used to alter the overall stiffness of the energy harvesting device enabling the increase or decrease of the overall stiffness of the device which results in a change in harvester's the natural frequency. Using this techniques, the authors reported an output power in the range 240–280 μW in the low frequency range 22–32 Hz. The suggested technique addressed the high frequency issue with an improved output power, but the power remains low.

Yang et al [60] on the other hand, proposed a multi-frequency energy harvester consisting of three permanent magnets and three sets of two-layer coils supported by a beam. The idea here is that energy is harvested under the first, second, and third resonant modes

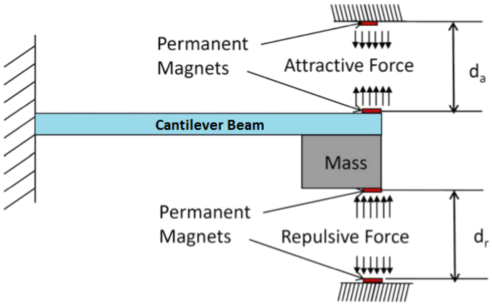

Figure 2.27: Schematic of the variable magnetic stiffness resonant frequency tuning technique

corresponding to the beams resonance frequencies of $369, 938$ and 1184 Hz. Even though the harvester does harvest at three different frequencies, it is yet again another example of resonance-based vibration energy harvesting which has the same limitations when it comes to harvesting vibration energy from a widband of frequencies.

2.4 Summary

In this chapter we reviewed different forms of energy harvesting and vibration energy harvesting in particular. We discussed the differences between the three main transduction mechanisms used in vibration energy harvesting and highlighted their advantages and disadvantages. A detailed analysis of linear electromagnetic energy harvesting and its fundamental principles were presented. We also reviewed different applications such as household items such as TV remote controls, flashlights and power faucets and wireless sensors networks for failure detection in rails and structures. We identified and discussed the limitations of linear vibration energy harvesters and why they are not suitable for harvesting energy from environmental vibrations. At the end of the chapter we surveyed different frequency widening techniques that have been proposed over the last few years as vibration energy harvesting technology tries to address some of the limitations still facing vibration energy harvesting.

In the next chapter we present a new architecture of electromagnetic vibration energy harvesting, namely the Springless vibration energy harvester. The harvester's physical model as well as its experimental and numerical results will be presented and discussed.

Chapter 3

The Springless Electromagnetic Vibration Energy Harvester

This chapter describes and analyzes the prototype of the Springless vibration energy harvester. A generalized mathematical model of the SVEH is then developed. The model will be adapted for different configurations of the harvester in subsequent chapters.

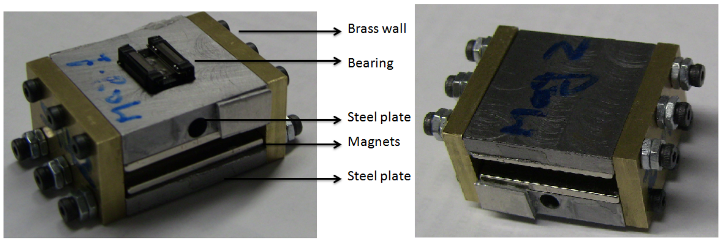

Figure 3.1: Top view and bottom view of SVEH steel cage

3.1 Prototype

The Springless vibration energy harvester (SVEH) is based on earlier work [27] on electrostatic VEH. The SVEH prototype consists of an electromagnetic transducer and a mechanical oscillator. The oscillator is made of a seismic mass made of four rare earth magnets, Sintered Neodymium (NdFeB), two mounted on the upper plate and two on the bottom steel plate held together by two brass walls to form a steel cage as shown in Figures 3.2 and 3.1. The seismic mass comprised of magnets, steel plates, and the brass walls, has a mass $m = 120\,\text{g}$. The mass is constrained to move between end-stoppers at either end of the track, each stopper is made of two identical springs embedded in a Lexan wall and fastened to the edge of an aluminum base shown in Figure 3.3.

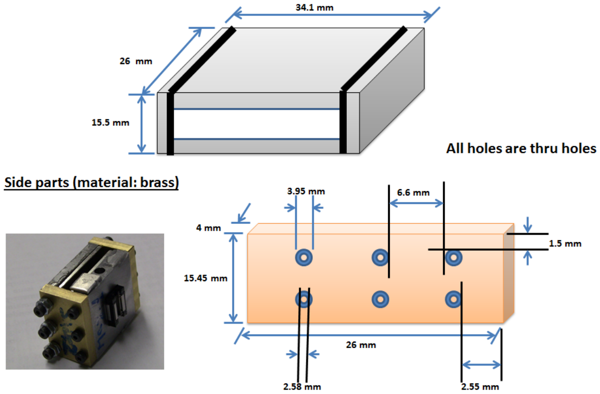

Figure 3.2: Schematic of the SVEH steel cage and side wall

A linear guide is also fastened to the base extends between the two end stoppers. The carriage carrying the seismic mass moves freely along the linear guide with respect to a stationary concentric coil in response to base excitations. The dimensions of the steel cage and aluminum base of the SVEH prototype, shown in Figure 3.4, are listed in Table 3.1.

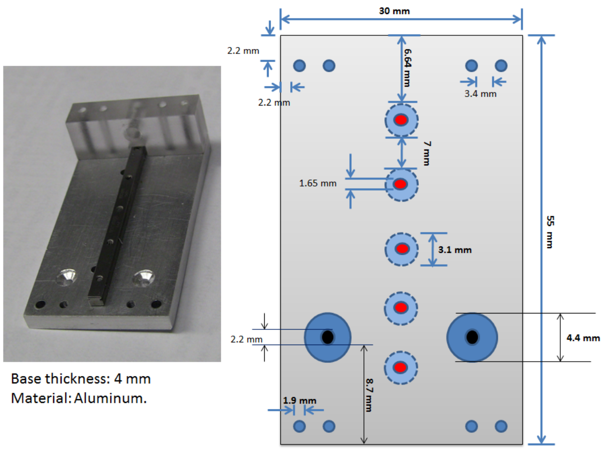

Figure 3.3: SVEH base with one wall attached

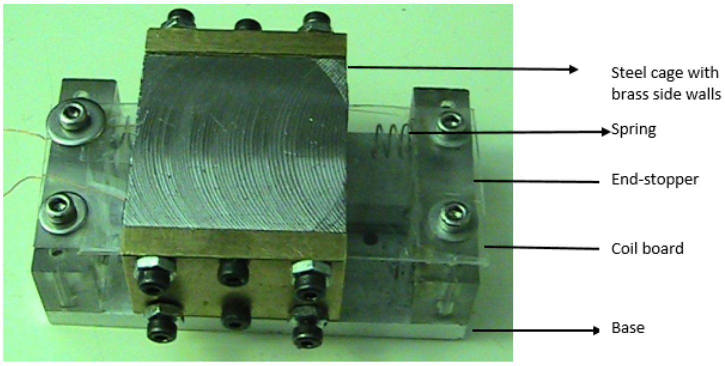

Figure 3.4: Prototype of the SVEH

The magnetic circuit of the harvester determines the strength of the electromechanical coupling between the electromagnetic transducer and the mechanical oscillator. It is therefore of great importance to accurately design the magnetic circuit with the objective to maximize the flux density around the coil during operation of the harvester. A finite element (FE) model of the magnetic circuit is developed and simulated using ANSYS software. In the next section the electromagnetic transducer is analyzed.

Table 3.1: Harvester Dimensions

Parameter	Value (mm)
Base Length	55
Base Width	30
Cage Length	25.41
Cage Width	25.39
Wall Length	30
Wall Thickness	7.6

3.2 Electromagnetic Transducer

The SVEH electromagnetic transducer consists of a magnetic circuit comprising four magnets, steel cage, and concentric coil. The ferromagnetic steel cage provides a return path for the magnetic field to maximize flux density inside the cage.

Table 3.2: Properties of the 25, 40 and 60 turns coils

Number of turns	Parasitic Resistance (Ω)	Inductance (μ H)	Length (m)
25	2.4	21	1.75
40	3.6	45	2.8
60	4.4	83	4.2

The coil, Figure 3.5, is hand wound out of 34 American Wire Gauge (AWG) magnetic wire. Only those stretches lying in the plane of the of the coil carrier, Figure 3.5, cut the magnetic field and produce an electromotive force (emf). The sum of those stretches is dubbed the effective coil length (l). Three coils withe different number of turns were used in this study, their effective length were calculated and listed in Table 3.2. The coil parasitic resistance and inductance were measured and are also listed in Table 3.2

Figure 3.5: Picture of the concentric coil

Magnetic Circuit The finite element modeling software ANSYS is used to investigate the magnetic flux density in the air gap of the SVEH and its vicinity. The FE model describes the geometry, material properties, boundary conditions, and the field system equations of the magnetic circuit. The FE model is comprised of permanent magnets arranged with alternating polarities between N and S, the steel cage, the air gap separating the magnets, and the air region surrounding the SVEH. Two dimensional elements,

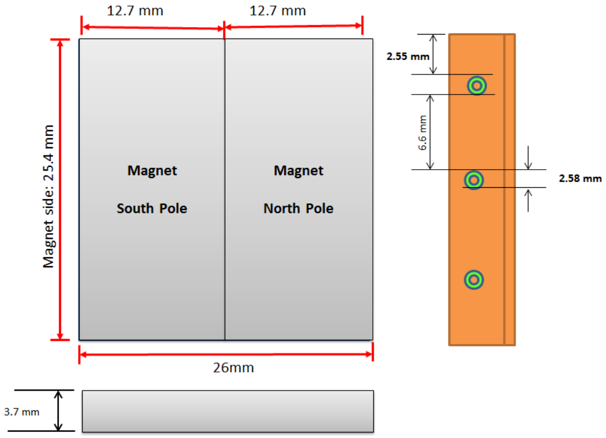

Figure 3.6: Top side view of the magnets, as well as view of the cage brass wall

PLANE53, were deployed to model the magnetic field with an average edge size of 0.5 mm. The magnet dimensions are listed in Table 3.3. The boundaries of the meshed area were set at four times the permanent magnet width to account for stray magnetic field lines. The relative permeabilities of air, steel, and permanent magnets were set to $\mu_a = 1$, $\mu_s = 100$, and $\mu_m = 1.05$, respectively.

A schematic of the SVEH magnetic circuit is shown in Figure 3.7.

Table 3.3: Magnet specifications

Dimensions (mm)	25.4 x 12.7 x 1.588
Material	Sintered Neodymium
Mass	4 gr
Surface Field (B)	12600 Gauss

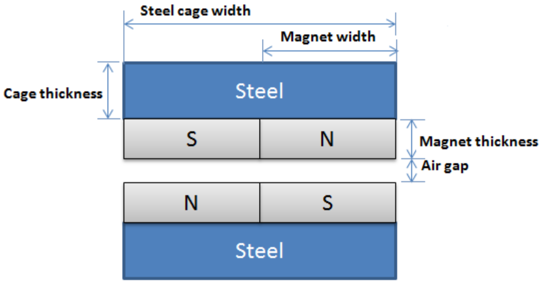

Figure 3.7: SVEH magnetic circuit

A top view of the simulated magnetic flux density within the cage is shown in Figure 3.8. The figure shows the variation of the magnetic flux density where field lines pointing into the page are represented in red hue and field lines pointing out of the page are represented in blue hue. The magnetic flux density along the centerline of the cage, where the coil is located, is almost constant at $B = 0.749$ T in the left and right halves of the cage. The flux density switches polarity at the center of the cage, Figure 3.8, due to the opposite (S-N and N-S) polarities of the two sets of magnets.

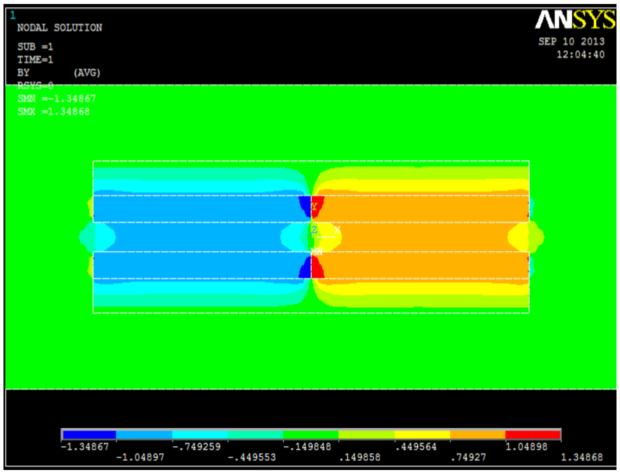

Figure 3.8: Magnetic flux density

This setup allows the induced voltage across the two sides of the coil to interact constructively and, hence, maximize harvested power. For validation purposes, we measured the magnetic flux density in the cage by placing the probe of a Gaussmeter at 13 different points along its centerline. The measured and simulated flux density, Figure 3.9, reach maximum of $B = 0.75$ T. Comparing measured and simulated magnetic flux density results shows close qualitative and quantitative agreement. The flux density is reaches a maximum over 6–7 mm range, where the coil is located, while the magnets oscillate with respect to it, thereby maximizing harvested power.

To study the dynamics of the harvester, a mathematical model of the system is developed and simulated. All mathematical simulations presented in this work were carried out using Mathematica software. In the next section, a generalized model of the harvester is presented.

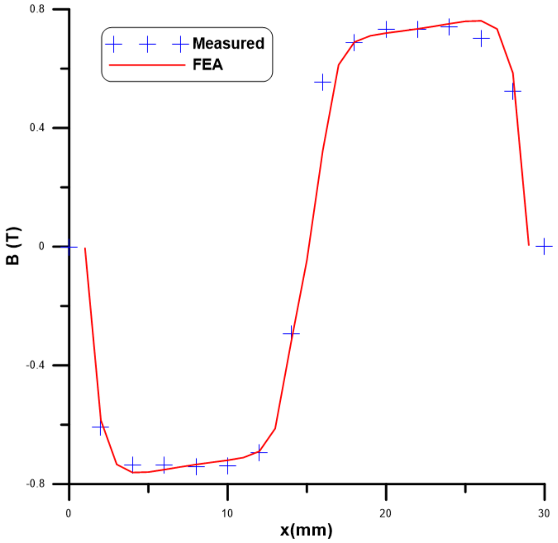

Figure 3.9: Measured and simulated magnetic flux density

3.3 SVEH Model

The schematic of the SVEH in Figure 3.10 depicts a simplified model of the harvester. The harvester can be modeled as a single degree of freedom (SDOF) oscillator, with the mechanical and electrical damping opposing the motion of the seismic mass m. The mechanical damping representing mechanical energy losses along the linear guide, and nonlinear damping representing energy losses during impact with end walls. The electrical damping is due to interaction between electrical and magnetic fields and energy losses in the coil resistance and load resistance. During motion, the seismic mass makes intermittent contacts with the motion-limiting end-stoppers. The sequence of collisions with the end-stoppers introduce nonlinearities in the harvester, which give rise to a non-smooth differential equation containing piecewise linear terms representing change in the spring stiffness.

The mass moves freely along the linear guide in the free distance (actual rail length -

cage length) between the uncompressed end springs denoted x_t. The uncompressed length of the end springs is denoted x_s and their fully compressed length is denoted x_c. These prototype dimensions are listed in Table 3.4. When the mass m engages the springs, they react with linear stiffness k_1. When the springs are fully compressed, the harvester essentially encounters a hard stop represented by a linear spring with a much higher stiffness $k_2 >> k_1$ [61].

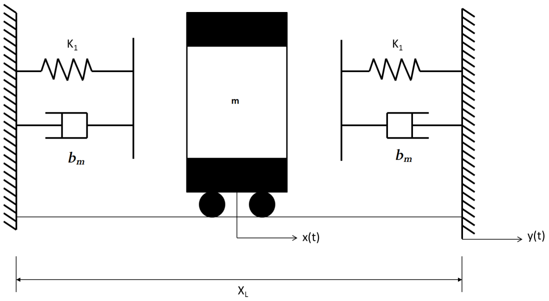

Figure 3.10: Force-displacement relationship

Table 3.4: Harvester dimensions

Parameter	Value (mm)
x_c	2
x_s	6
x_t	7.8

A general model for the harvester motion can be written as:

$$m\,\ddot{x} + b_m\,\dot{x} + f_n(x,\dot{x}) + F_e + F_{st}(x) + m\,g\,\sin\theta = -m\,\ddot{y} \tag{3.1}$$

where y is the displacement of the housing unit and x is the relative displacement of m with respect to the housing, b_m is the linear damping coefficient, $F_{st}(x)$ is a piecewise-linear function describing the harvester stiffness, $f_n(x, \dot{x})$ is the nonlinear damping due to impact energy losses, $F_e = b_m\, \dot{x}$ is the electrical damping force due to induced emf. The angle θ is describes the inclination of the harvester with respect to the surface. Therefore, the equation of motion can be written as:

$$m\, \ddot{x} + (b_m + b_e)\, \dot{x} + f_n(x, \dot{x}) + F_{st}(x) + m\, g\, \sin\theta = -m\, \ddot{y} \tag{3.2}$$

3.4 Summary

In this chapter, a description of the proposed harvester was provided and its components were analyzed. The magnetic circuit was simulated using the FE software ANSYS, and the field strength was measured experimentally using a Gaussmeter. From the numerical and experimental results, we conclude that the magnetic flux density in the cage regions occupied by the coil is almost constant at approximately 0.749 T. We finished the chapter by developing a general model of the harvester for further analysis.

In the next chapters we consider the dynamic response of the harvester in two configurations corresponding to the two extreme positions of the harvester. In the first configuration, the harvester is positioned horizontally and the mass m moves laterally when excited. In the second configuration, the harvester is positioned vertically and the mass is allowed to move up and down in response to base excitations.

Chapter 4

Horizontal SVEH

This chapter analyzes the horizontal configuration of the SVEH. A model, as well as experimental, analytical, and numerical results of the harvester are presented. Stability and bifurcation analyses of the harvester are carried out to characterize the harvesting parameter space, namely the frequency and amplitude of base acceleration.

4.1 Horizontal SVEH Model

Figure 4.1 shows a schematic of the horizontally aligned harvester. The seismic mass m is treated as a point mass, which reduces the model to that shown in Figure 4.2. We set the origin of the inertial coordinate system at the track midpoint.

In this configuration, the component of the weight along the track is zero ($\theta = 0$), therefore the harvester equation of motion can be obtained from Equation 3.2 as

$$m\,\ddot{x} + (b_m + b_e)\,\dot{x} + b_n\,x^2\dot{x} + F_{st}(x) = -m\,\ddot{y} \tag{4.1}$$

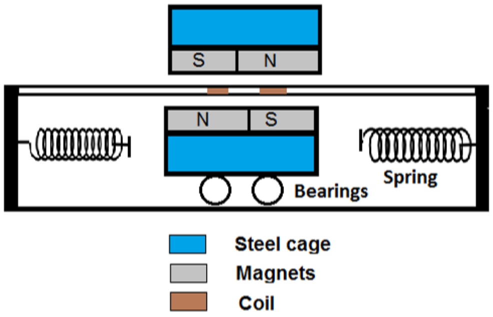

Figure 4.1: Schematic of the horizontally aligned SVEH

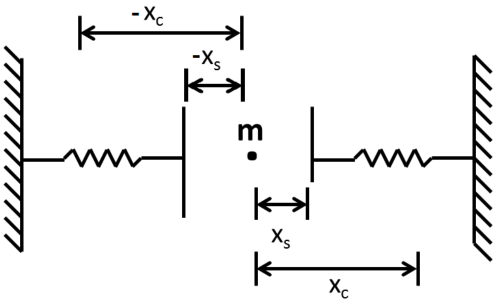

Figure 4.2: Simplified model of the SVEH

The restoring force $F_{st}(x)$ accounting for the linear stiffness of the springs and impact with the hard stops, the fully compressed springs, modeled as

- if $-x_s \leq x \leq x_s$, no contact occurs with springs and the stiffness is set to 0
- if $x_c \leq |x| < x_s$, contact occurs with the springs and stiffness is set $k_1 = 950$ N/m
- if $x_c < |x| \leq \frac{L}{2}$, contact occurs with the fully compressed springs and stiffness is set to $k_2 = 10^5$ N/m

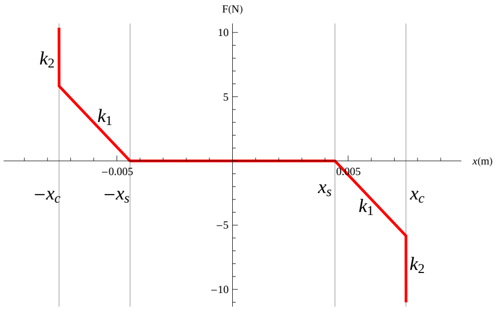

Figure 4.3: Force-displacement relationship

The linear spring stiffness k_1 was measured experimentally, while the hard stop stiffness k_2 was estimated by matching the measured voltage waveform to that predicted by the model. Therefore the restoring force-displacement relationship, Figure 4.3, can be written as follows:

$$F_{st}(x) = \begin{cases} 0 & -x_s \leq x \leq x_s \\ k_1(x - x_s) & x_s < x \leq x_c \\ k_2(x - x_c) + k_1(x_c - x_s) & x_c < x \leq \frac{L}{2} \\ k_1(x + x_s) & -x_c < x < -x_s \\ k_2(x + x_c) + k_1(x_s - x_c) & -\frac{L}{2} \leq x \leq -x_c \end{cases} \tag{4.2}$$

The cubic damping term represents mechanical energy losses present when the mass engages the end springs [62]. It mimics van der Pol damping which results in sudden velocity reversal similar to that which the mass experiences when it engages the end springs [63]. The value of the cubic damping coefficient was found using the least squares method to fit the experimental frequency-response curve data to the model's frequency-response curve.

The SVEH scavenges kinetic energy from environmental vibrations as base acceleration.

We assume the input vibrations to be harmonic represented by

$$\ddot{y} = a(t) = A_\circ \cos\omega\, t \tag{4.3}$$

where $A_\circ$ and ω are the amplitude and frequency of base acceleration.

The equation of motion, Equation (4.1), is nondimensionalized using the nondimensional variables,

$$\hat{x} = \frac{x}{L},\ \hat{t} = \omega_n\, t \tag{4.4}$$

and the nondimensional parameters,

$$\begin{aligned}
\alpha_1 &= \frac{x_s}{L},\ \alpha_2 = \frac{x_c}{L},\ A = \frac{A_0}{L\, m\, \omega_n^2} \\
\zeta_1 &= \frac{b_e + b_m}{2\, m\, \omega_n},\ \zeta_2 = \frac{b_n}{2\, m\, \omega_n},\ \Omega = \frac{\omega}{\omega_n},\ \gamma = \big(\frac{\omega_h}{\omega_n}\big)^2 \\
\hat{F_{st}}(x) &= \begin{cases} 0 & -\alpha_1 \le \hat{x} \le \alpha_1 \\ \hat{x} - \alpha_1 & \alpha_1 < \hat{x} \le \alpha_2 \\ -\alpha_1 + \alpha_2 + \gamma(\hat{x} - \alpha_2) & \alpha_2 < \hat{x} \le 1 \\ \alpha_1 + \hat{x} & -\alpha_2 \le \hat{x} < -\alpha_1 \\ \alpha_1 - \alpha_2 + \gamma(\alpha_2 + \hat{x}) & -1 \le \hat{x} < -\alpha_2 \end{cases}
\end{aligned} \tag{4.5}$$

where,

$$\omega_n = \sqrt{\frac{k_1}{m}},\ \omega_h = \sqrt{\frac{k_2}{m}} \tag{4.6}$$

The nondimensional equation of motion is written as,

$$\ddot{x} + 2\,\dot{x}\,(\zeta_1 + \zeta_2\, x^2) - F_{st}(x) = A\, \cos(2\pi\, \Omega\, t) \tag{4.7}$$

where the hats have been dropped for the sake of brevity.

4.2 Experimental Results

The experimental setup is comprised of a LabWorks electromagnetic shaker, model ET-126B [64], an amplifier, model $Pa-138$, a Vibration Research control unit, VibrationView software interface [65], an accelerometer DYTRAN 3055B [66], and an oscilloscope. The electromagnetic shaker, shown in Figure 4.4, acts as a source of base acceleration, while the control unit maintains the commanded amplitude of base acceleration as the impedance level of the harvester varies. We set the parameter space for base accelerations to the frequency range 5–25 Hz and amplitude range 0.05 g–0.6 g at zero angle to the horizontal. The harvester is attached by double adhesive tape to an L-shape platform mounted to the shaker head, Figure 4.4. The accelerometer is glued to the L-shape platform along the direction of motion. The frequency-response curves are obtained by measuring the harvester's open-loop RMS output voltage across the coil terminals during frequency sweeps. The output waveforms at a given base acceleration are measured using the oscilloscope.

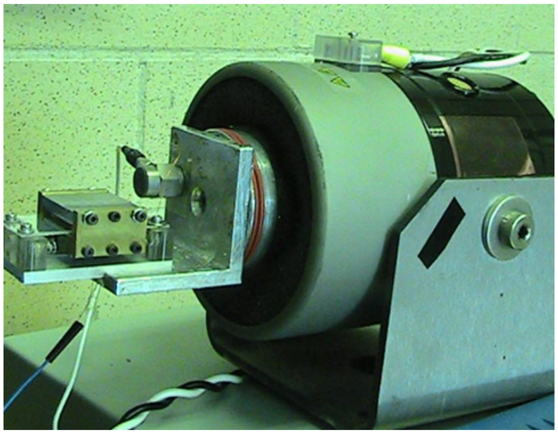

Figure 4.4: Experimental setup for the horizontal SVEH

Figures 4.5 and 4.6 show the open circuit output voltage across 25 and 40 turns coils respectively. The waveforms were obtained in each case for a base acceleration amplitude

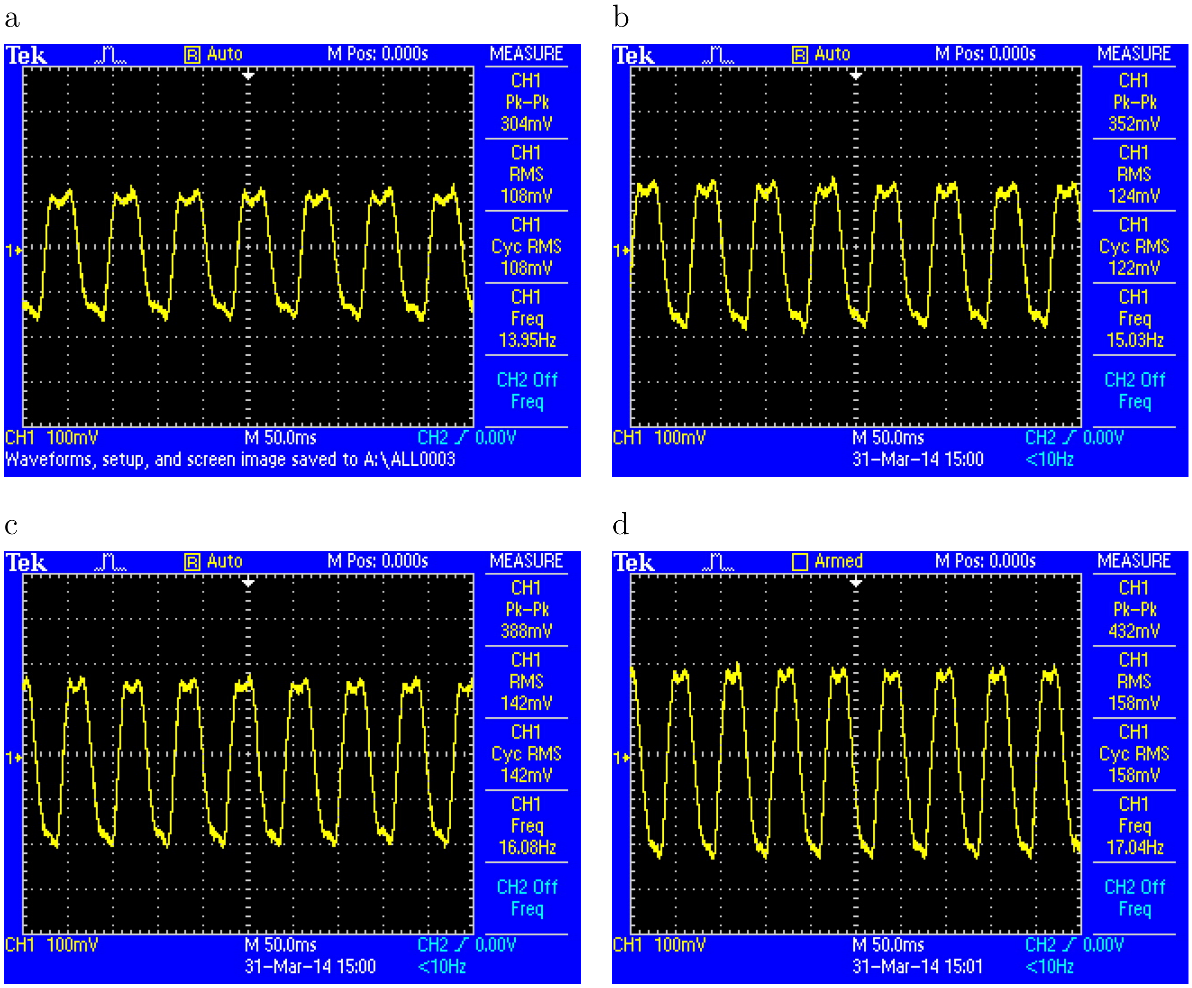

a

Tek ⎍ R Auto M Pos: 0.000s MEASURE

CH1 Pk−Pk 304mV

CH1 RMS 108mV

CH1 Cyc RMS 108mV

CH1 Freq 13.95Hz

CH2 Off Freq

CH1 100mV M 50.0ms CH2 ⁄ 0.00V

Waveforms, setup, and screen image saved to A:\ALL0003

b

Tek ⎍ R Auto M Pos: 0.000s MEASURE

CH1 Pk−Pk 352mV

CH1 RMS 124mV

CH1 Cyc RMS 122mV

CH1 Freq 15.03Hz

CH2 Off Freq

CH1 100mV M 50.0ms CH2 ⁄ 0.00V

31−Mar−14 15:00 <10Hz

c

Tek ⎍ R Auto M Pos: 0.000s MEASURE

CH1 Pk−Pk 388mV

CH1 RMS 142mV

CH1 Cyc RMS 142mV

CH1 Freq 16.08Hz

CH2 Off Freq

CH1 100mV M 50.0ms CH2 ⁄ 0.00V

31−Mar−14 15:00 <10Hz

d

Tek ⎍ ☐ Armed M Pos: 0.000s MEASURE

CH1 Pk−Pk 432mV

CH1 RMS 158mV

CH1 Cyc RMS 158mV

CH1 Freq 17.04Hz

CH2 Off Freq

CH1 100mV M 50.0ms CH2 ⁄ 0.00V

31−Mar−14 15:01 <10Hz

Figure 4.5: Output voltage waveforms for base acceleration amplitude of $A_\circ = 0.4$ g and frequencies of: a) $\omega = 14$ Hz, b) $\omega = 15$ Hz, c) $\omega = 16$ Hz, and d) $\omega = 17$ Hz using a 25 turns coil

of $A_\circ = 0.4\,g$ at four frequencies along the resonant branch of the harvester. The measured output voltages across the coil terminals are listed in Tables 4.1 and 4.2.

From the figures, we observe the SVEH's anharmonic output voltage waveforms. In

Table 4.1: Output voltage RMS for base acceleration amplitude of $A_\circ = 0.4$ g across terminals of a 25 turns coil

Base acceleration frequency (Hz)	Output voltage (V)
14	108
15	124
16	142
17	158

Table 4.2: Output voltage waveforms for base acceleration amplitude of $A_\circ = 0.4$ g using a 40 turns coil

Base acceleration frequency (Hz)	Output voltage (V)
15	125
17	158
17.86	175
19.72	204

particular, we note the existence of two closely spaced peaks during each half-cycle. The time domain distortions indicate the existence of nonlinearities in the system response, as a result of the impact of the seismic mass on the limiters.

Figure 4.7 shows the frequency-response curves of the 25 turns SVEH under frequency up- and down-sweeps. The frequency of base acceleration was swept up and down the frequency range 5–25 Hz, while maintaining the amplitude fixed at $A_\circ = 0.3g$, $0.4g$, 0.5 g, or 0.6 g. The SVEH frequency-response demonstrates coexisting high and low output voltage branches corresponding to large (resonant) impact oscillations and small non-impact oscillations. These branches coexist within hysteretic band limited from the right by a jump

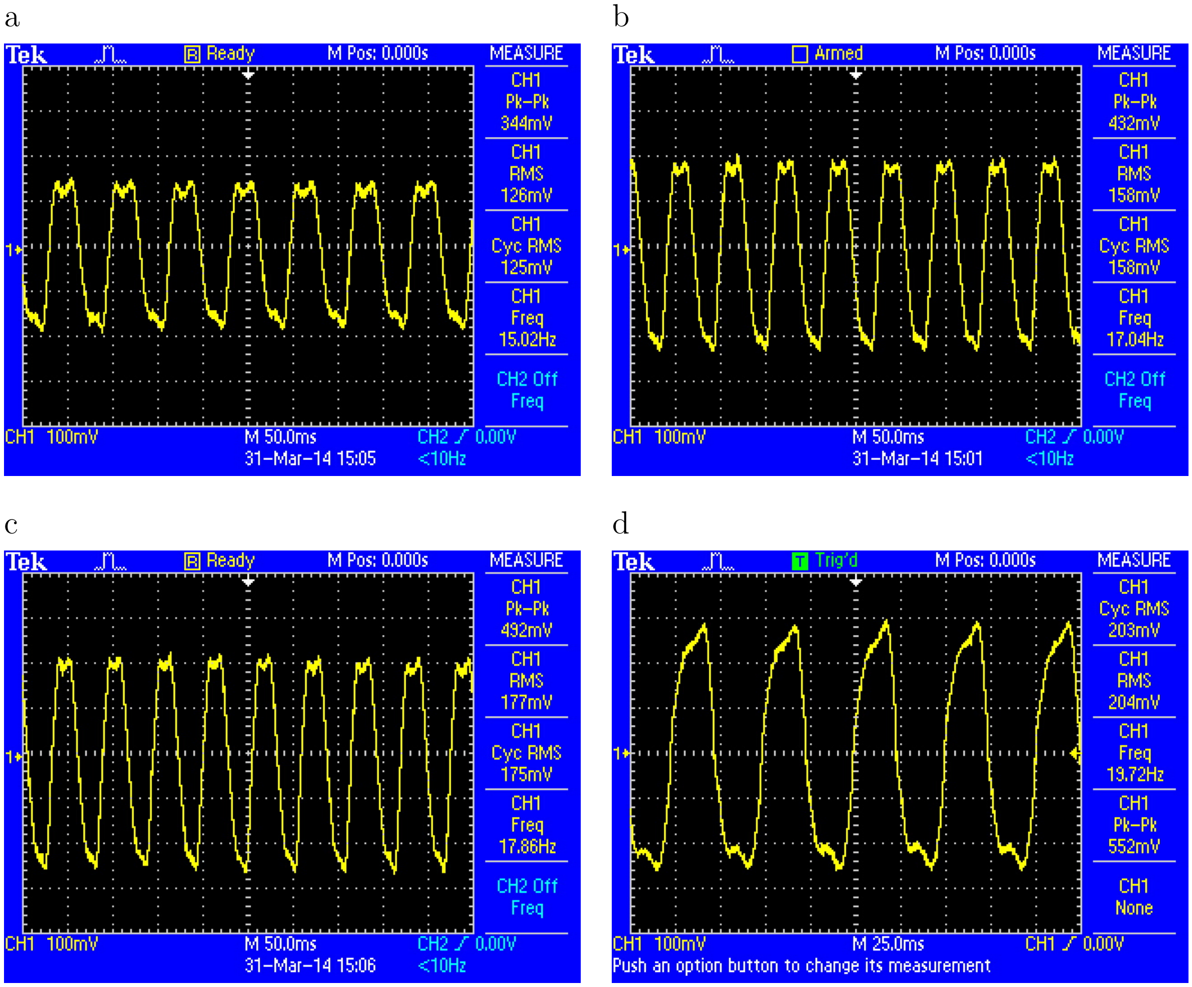

Figure 4.6: Output voltage waveforms across the 40 turns coil for base acceleration amplitude of $A_\circ = 0.5$ g and frequencies of: a) $\omega = 15$ Hz, b) $\omega = 17$ Hz, c) $\omega = 17.86$ Hz, and d) $\omega = 19.72$ Hz

down during up-sweeps and from the left by a jump up during down sweeps. The harvester's output voltage attains maximum value at the peak of the frequency-response curve. The frequency-response curves and the hysteretic band extend further to the right (with the peak voltage appearing at higher frequencies) as the amplitude of base acceleration and, therefore, input power is increased

Along the high voltage (resonant) branch, the voltage is almost linearly proportional to the frequency regardless of the base acceleration amplitude. This phenomenon is attributed to the seismic mass motions filling the entire track between the two springs. When the mass motions reach the maximum allowable displacement,

$$d \approx x_t + x_s - x_c$$

it remains almost constant as the excitation level increases, since it is limited by the two hard springs k_2. As a result, the velocity along this branch can be approximated as,

$$\dot{x} \approx \omega d \sin(\omega t + \phi)$$

substituting $\dot{x}$ in $V = B\,l\,\dot{x}$ we can write the output RMS voltage as

$$V = \frac{B\,l\,d}{\sqrt{2}}\omega \tag{4.8}$$

As a result, the measured output voltage in this branch varies linearly with the frequency, Figure 5.7, in accordance with Equation (4.8). Further, since base acceleration amplitude does not appear in equation (4.8), the voltage output falls on the same line for all acceleration amplitudes reported here.

The harvesting bandwidth increases with increasing acceleration amplitude. The harvesting bandwidth is defined as the difference between the frequencies at peak voltage V_{peak} and the half-power point $\frac{V_{peak}}{\sqrt{2}}$ on the upper (up-sweep) branch. A wide harvesting bandwidth during frequency up-sweeps only. The bandwidth of the down-sweep is not considered as it falls below the half-power point.

Similar experiments were conducted to obtain the frequency-response curves for the 40 and 60 turns SVEHs at base acceleration amplitude of $A_\circ = 0.5$ g. Figure 4.8 compares those results to that of the 25 turns SVEH. As the number of turns is increased

Table 4.3: Peak RMS output voltage, frequency and harvesting bandwidth of the SVEH for input acceleration amplitudes $A_\circ = 0.3\ g, 0.4\ g, 0.5\ g$ and 0.6 g

Amplitude $A_\circ$ (g)	Peak RMS Voltage (V)	Peak Frequency(Hz)	Bandwidth (Hz)
0.3	0.28	13.8	5
0.4	0.45	17.3	5
0.5	0.55	18.5	6
0.6	0.57	19.8	7

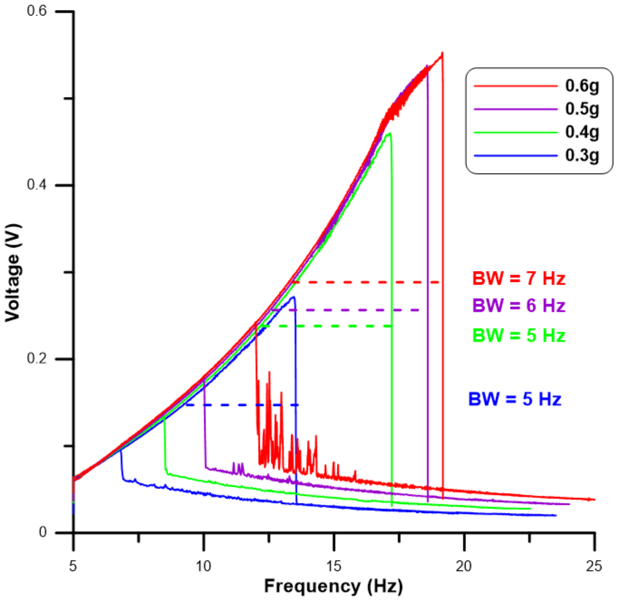

Figure 4.7: SVEH experimental frequency-response curves for base acceleration amplitudes of $A_\circ = 0.3\ g, 0.4\ g, 0.5\ g$ and $0.6\ g$

the electromechanical coupling (harvesting efficiency) results in increased output voltage and harvesting bandwidth. Figure 4.8 shows that the SVEH peak voltage increases with

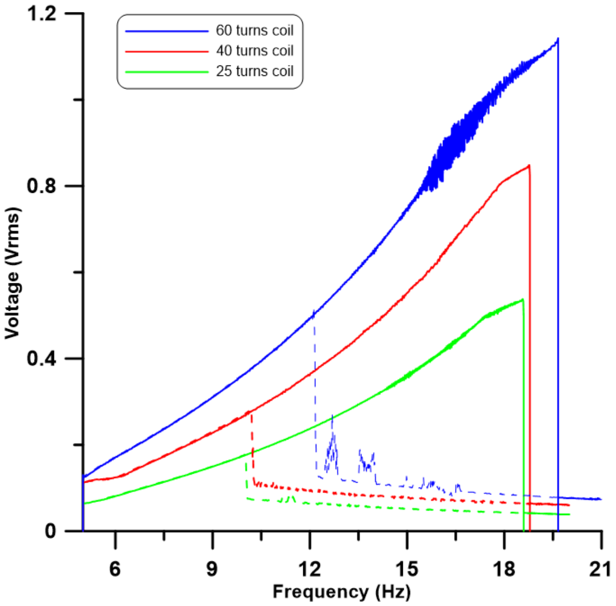

Figure 4.8: Experimental frequency response curves for SVEHs with $25, 40$ and 60 turns coils at a base acceleration amplitude of $A_{\circ} = 0.5$ g

an increase in the coil number of turns. The 60 turn SVEH reached a peak voltage of 1.14 V, while the 40 and 25 turns SVEHs reached a maximum voltage of 0.85 and 0.54 V respectively. Elliot and Zelleti [67] derived a coil figure of merit (FoM) given by:

$$FoM = \frac{(B\,l)^2}{R_p} \tag{4.9}$$

The coil parasitic resistance R_p is given by:

$$R_p = \frac{\rho\,l}{A} \tag{4.10}$$

where ρ is the coil's material resistivity and l and A are its length and cross-sectional area. Substituting R_p in Equation (4.9) we obtain:

$$FoM = \frac{B^2\,l\,A}{\rho} = \frac{B^2\,V}{\rho} \tag{4.11}$$

where, V is the coil volume. Equation (4.11) indicates that the coil FoM (electromechanical coupling efficiency) increases linearly with its copper volume. Using Equation (4.9), the coil FoM for the 25, 40, and 60 turns SVEHs are listed in Table 4.4.

Table 4.4: SVEH coil FoM for coils with 25, 40, and 60 turns

Coil Turns	R_p (Ω)	FoM	Copper Volume (m^3)
25	2.6	0.698	0.019
40	3.6	1.193	0.032
60	4.4	2.195	0.059

4.3 Output Power

In this section we investigate the optimal output power of the SVEH. A resistive load R_L was connected across the harvester's coil terminals and the base acceleration frequency was swept up and down the range ω = 5–20 Hz while the amplitude was held constant. The frequency sweeps were repeated for different values of the resistive load. Since the measured coil's inductance were negligible, less than 100 μWatts, the load can be assumed to be purely resistive and the output power can be evaluated as $P = V^2/R_L$, where V is the output voltage measured across the load resistor R_L.

For an acceleration amplitude $A_\circ = 0.2$ g, the output power frequency curves are shown in Figure 4.9 for five values of the load resistance in the range $R_L = 2.5 - 30.2\ \Omega$. The a maximum output power $P \approx 1.2$ mW was achieved for a load resistor $R_L = 3.2\ \Omega$. The frequency output power curves for input acceleration amplitudes of $A_\circ = 0.3$ and 0.4 g

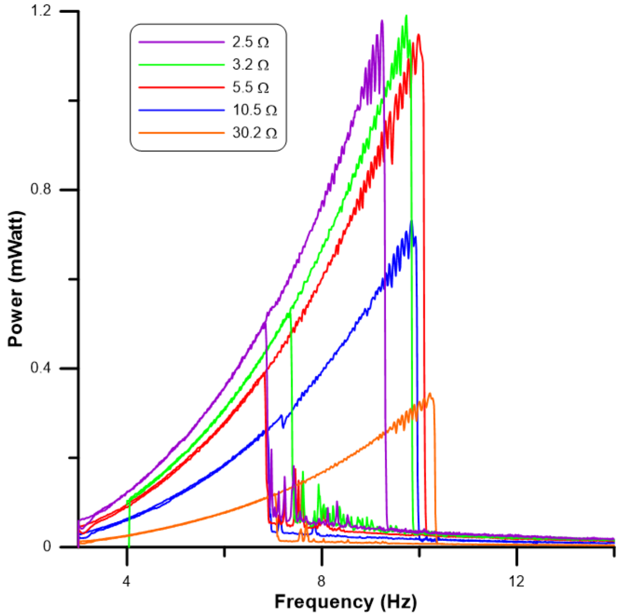

Figure 4.9: The frequency-power curves of the SVEH for input acceleration $A_\circ = 0.2\ g$ and optimal load resistance $R_L = 2.5$–$30.2\ \Omega$

are shown in Figures 4.10 and 4.11, the corresponding optimal output power $P \approx 5$ and 8 mW, and optimal resistances are $R_{opt} = 2.8$ and $3.2\ \Omega$ respectively.

Figures 4.12 shows the 60 turns SVEH frequency output power curve for a base acceleration of $A_\circ = 0.5\,\text{g}$. The output power is a function of the load resistance is shown in Figure 4.13 for 25, 40 and 60 SVEHs. We conclude that the optimal power of the 25, 40 and 60 SVEHs is 5.4, 8.5 and 12 mW respectively, and the optimal load resistance is 2.2, 3.2 and 3.8 Ω.

Power conditioning circuits are required to rectify the time-varying output of the SVEH. The anharmonic waveform of the SVEH raises a question of how efficiently can its output be rectified compared to traditional (linear) VEHs that produce harmonic output voltage.

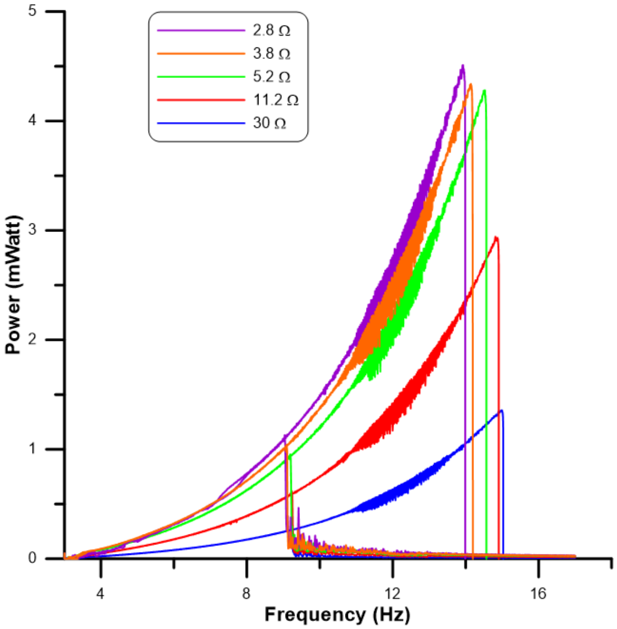

Figure 4.10: The frequency-power curves of the SVEH for input acceleration $A_\circ = 0.3\ g$ and load resistance $R_L = 2.8–30\ \Omega$

To answer this question, Yilmaz et al's [68] high-efficiency full-wave MOSFET rectifier was used to rectify the output voltage of the 40 turns SVEH excited with base acceleration amplitude and frequency of $A_\circ = 0.4\,\mathrm{g}$ and $\omega = 18\,\mathrm{Hz}$. The raw and rectified output voltage are shown in Figure 4.14. The figure also shows the output voltage after a 100 μF smoothing capacitor was connected in parallel with the load resistance.

The RMS voltage of the raw signal is 575 mV, while that of the rectified signal is 535 mV. The smoothed voltage signal has a DC voltage of 525 mV reflecting a rectification efficiency of 93 %, close to the high-end of the rectification efficiency range reported by Yilmaz el al. for linear VEHs [68]. This is expected since an important source of rectification losses is the fraction of the harvesting cycle where the output voltage is less than the rectifier

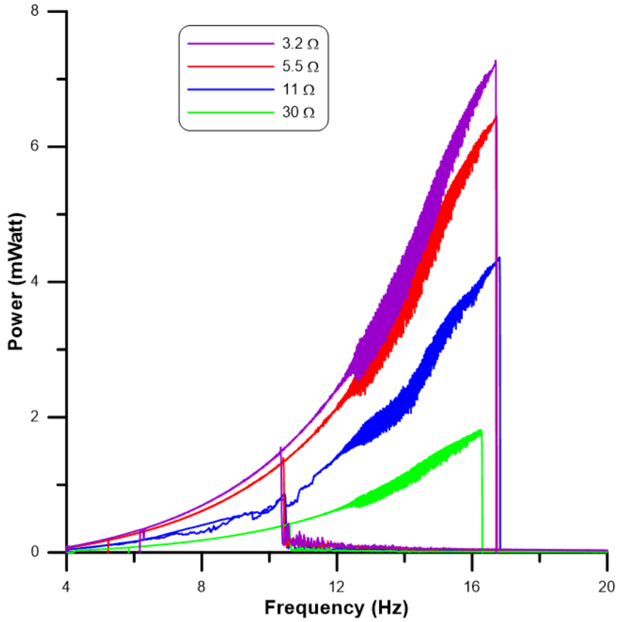

Figure 4.11: The frequency-power curves of the SVEH for base acceleration $A_\circ = 0.4\ g$ and load resistance $R_L = 3.2$–$30\ \Omega$

threshold voltage. The loss fraction is smaller for SVEH voltage waveform, where voltage reverse sign almost instantaneously during mass impacts with the walls, than it is for the linear VEH harmonic (more gradual) waveform.

4.4 Numerical Frequency Response

The response of nonlinear dynamic systems can be determined numerically using long-time integration. However, long-time integration does not converge to periodic solutions easily near bifurcation points, provides no information about their stability, and can not converge to the unstable solutions relevant to the study of system stability. Therefore, a

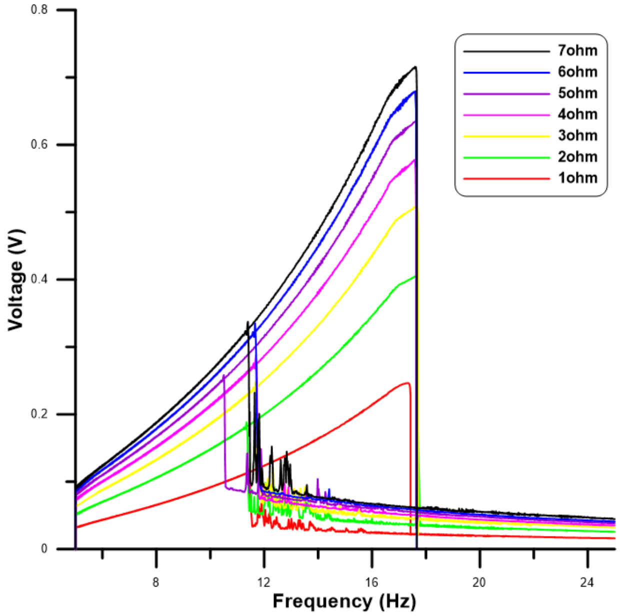

Figure 4.12: The frequency-power curves of the 60 turns SVEH for base acceleration $A_\circ = 0.5\ g$ and a coil with 60 turns for loads $R = 1$ to $7\ \Omega$

shooting method in conjunction with Floquet theory is used to obtain periodic solutions and determine their stability [69]. The method calls for an iterative process where the system equations are integrated numerically for a period T starting from an initial guess. Since periodicity requires the start and end points of the orbit to be identical, the difference between them is used to correct the initial guess after each iteration in a Newton-Raphson scheme. The desired orbit is obtained when the correction to the initial guess falls within a predefined tolerance [69].

The SVEH's equation of motion, Equation (4.1), can be written as a system of two first

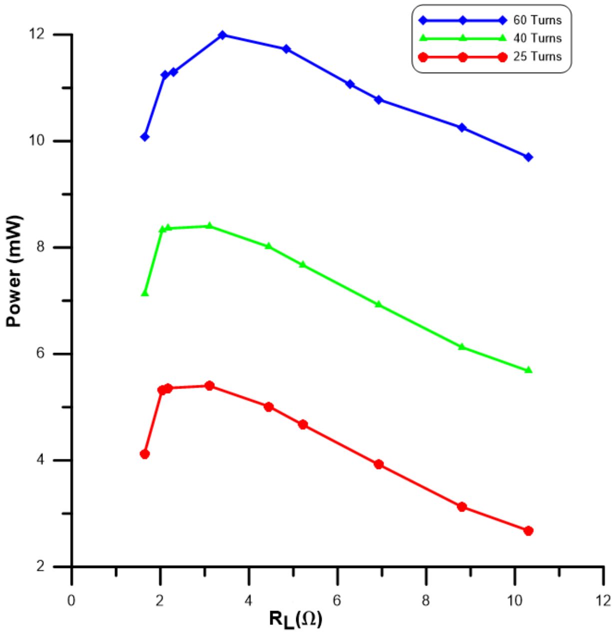

Figure 4.13: Harvester's power versus load for input acceleration amplitude $A_\circ = 0.5$ g for 25, 40 and 60 turns coil

order differential equations

$$\dot{x}_1 = x_2 \tag{4.12}$$

$$\dot{x}_2 = -\frac{b_e + b_m}{m} x_2 - \frac{b_n}{m} x_2\, x_1^2 - \frac{F_{st}(x_1)}{m} - \ddot{y} \tag{4.13}$$

which may be generalized in the form;

$$\dot{\mathbf{x}} = \mathbf{F}(\mathbf{x}, t) \tag{4.14}$$

where $\mathbf{x}$ is the state vector and $\mathbf{F}$ is the right hand side vector.

The objective of the shooting method is to find a periodic solution, $\mathbf{x}(t) = \mathbf{x}(t + T)$,

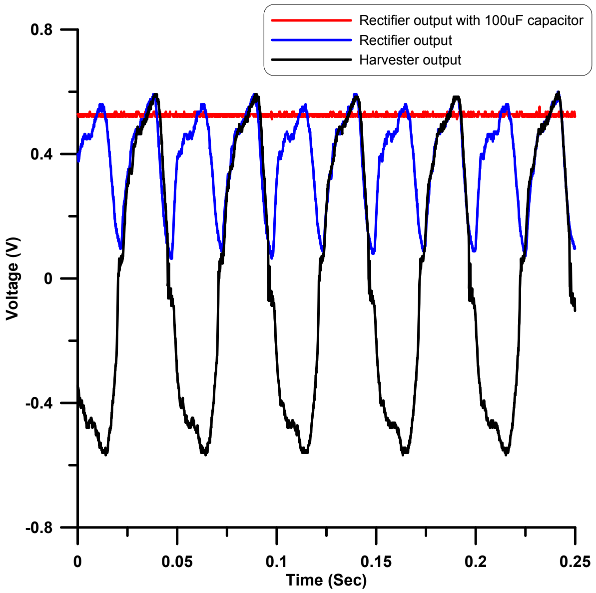

Figure 4.14: The raw and rectified output voltage of the 60 turns SVEH excited with base acceleration $A_{\circ} = 0.5\ g$ and $\omega = 18\,\mathrm{Hz}$

that satisfies Equation (4.14) by solving the boundary-value problem

$$\begin{gathered}\dot{\mathbf{x}} = \mathbf{F}(\mathbf{x}, t) \\ \mathbf{x}(0) = \boldsymbol{\eta},\ \boldsymbol{x}(T) = \boldsymbol{\eta}\end{gathered} \tag{4.15}$$

where $\boldsymbol{\eta}$ is the vector of unknown initial conditions. We begin by making a guess for the initial conditions $\boldsymbol{\eta}_0$. Defining $\Delta\,\boldsymbol{\eta}$ such that

$$\Delta\,\boldsymbol{\eta} = \boldsymbol{\eta} - \boldsymbol{\eta}_0 \tag{4.16}$$

Integrating the system of Equations (4.15) from the initial condition $\boldsymbol{\eta}_0 + \Delta\,\boldsymbol{\eta}$ for a period T, we obtain the following relationship

$$\mathbf{x}(T, \boldsymbol{\eta}_0 + \Delta\,\boldsymbol{\eta}) - (\boldsymbol{\eta}_0 + \Delta\,\boldsymbol{\eta}) = 0 \tag{4.17}$$

Expanding the first term of Equation (4.17) in a Taylor series about $\boldsymbol{\eta}_0$

$$\mathbf{x}(T, \boldsymbol{\eta}_0 + \Delta\,\boldsymbol{\eta}) \;\approx\; \mathbf{x}(T, \boldsymbol{\eta}_0) + \frac{\partial \mathbf{x}}{\partial \boldsymbol{\eta}}(T, \boldsymbol{\eta}_0)\,\Delta\,\boldsymbol{\eta} + \dots \tag{4.18}$$

combining Equations (4.17) and (4.18) gives the following:

$$\left[\frac{\partial \mathbf{x}}{\partial \boldsymbol{\eta}}(T, \boldsymbol{\eta}_0) - I\right]\Delta\,\boldsymbol{\eta} = \boldsymbol{\eta}_0 - \mathbf{x}(T, \boldsymbol{\eta}_0) \tag{4.19}$$

where I is the identity matrix. The coefficient matrix $\frac{\partial \mathbf{x}}{\partial \eta}(T, \eta_0)$ is the slope of the trajectory $\mathbf{x}(t, \eta_0)$ with respect to $\boldsymbol{\eta}$. Differentiating the two elements of Equations (4.15) with respect to $\boldsymbol{\eta}$ we obtain

$$\begin{aligned}\frac{\partial}{\partial \boldsymbol{\eta}}\frac{d\mathbf{x}}{dt} &= \frac{\partial}{\partial \boldsymbol{\eta}}\mathbf{F}(\mathbf{x}, t) = D_{\mathbf{x}}\mathbf{F}(\mathbf{x}, \mathbf{t})\frac{\partial \mathbf{x}}{\partial \boldsymbol{\eta}} \\ \frac{\partial}{\partial \boldsymbol{\eta}}\mathbf{x}(0) &= \frac{\partial \boldsymbol{\eta}}{\partial \boldsymbol{\eta}} = I\end{aligned} \tag{4.20}$$

To find the coefficient matrix, we change the order of integration in the left hand side of Equation (4.20), combine Equations (4.15) and (4.20) and integrate the resulting coupled system

$$\begin{aligned}\dot{\mathbf{x}} &= \mathbf{F}(\mathbf{x})\\ \mathbf{x}(0) &= \eta_0\\ \frac{d}{dt}\Big[\frac{\partial \mathbf{x}}{\partial \eta}\Big] &= \big[D_{\mathbf{x}}F(\mathbf{x})\big]\frac{\partial \mathbf{x}}{\partial \eta}\\ \frac{\partial \mathbf{x}}{\partial \eta}(0) &= I\end{aligned} \tag{4.21}$$

for a period T to obtain $\frac{\partial \mathbf{x}}{\partial \eta}(T, \eta_0)$ and $\mathbf{x}(T, \eta_0)$. Substituting these values in Equation (4.19), we determine $\Delta\,\eta$, which is then used to update the guess value of the initial conditions according to $\eta_{i+1} = \eta_i + \Delta\,\eta_i$. This procedure is repeated iteratively until $\Delta\,\eta_i$ falls within a predefined tolerance.

Applying the shooting algorithm to the harvester's model given by Equation (4.12), we obtain the following system of differential equations

$$\begin{aligned}&\dot{x}_1 = x_2\\ &\dot{x}_2 = -\frac{b_e + b_m}{m}x_2 - \frac{b_n}{m}x_2x_1^2 - \frac{F_{st}}{m} - \ddot{y}(t)\\ &\frac{d}{dt}\frac{\partial x_1}{\partial \eta_1} = \frac{\partial x_2}{\partial \eta_1}\\ &\frac{d}{dt}\frac{\partial x_1}{\partial \eta_2} = \frac{\partial x_2}{\partial \eta_2}\\ &\frac{d}{dt}\frac{\partial x_2}{\partial \eta_1} = -\frac{b_e + b_m}{m}\frac{\partial x_2}{\partial \eta_1} - \frac{b_n}{m}\frac{\partial (x_2\, x_1^2)}{\partial \eta_1} - \frac{1}{m}\frac{\partial F_{st}}{\partial x_1}\frac{\partial x_1}{\partial \eta_1}\\ &\frac{d}{dt}\frac{\partial x_2}{\partial \eta_2} = -\frac{b_e + b_m}{m}\frac{\partial x_2}{\partial \eta_2} - \frac{b_n}{m}\frac{\partial (x_2\, x_1^2)}{\partial \eta_2} - \frac{1}{m}\frac{\partial F_{st}}{\partial x_1}\frac{\partial x_1}{\partial \eta_2}\\ &\mathbf{x}(0) = \boldsymbol{\eta}_0\\ &\frac{\partial x_1}{\partial \eta_1}(0) = 1,\ \frac{\partial x_1}{\partial \eta_2}(0) = 0,\ \frac{\partial x_2}{\partial \eta_1}(0) = 0,\ \frac{\partial x_2}{\partial \eta_2}(0) = 1\end{aligned} \tag{4.22}$$

To start the shooting algorithm an initial guess value of the periodic solution is required. The harvester's equation of motion, Equation (4.12), is solved by long-time integration for a given base acceleration and a point $\mathbf{x}_0$ on the steady-state orbit is selected as an initial guess $\boldsymbol{\eta}_0$. The initial guess is used to solve the system of Equations (4.22) until convergence is obtained. Convergence to a periodic solution is achieved when the change in the initial guess between two iterations falls within a tolerance of $||\Delta\boldsymbol{\eta}|| \leq 10^{-4}$.

The stability of the orbits $\mathbf{x}(t, \boldsymbol{\eta})$ obtained from this process can be assessed using the Floquet theory [69]. It analyzes the eigenvalues of the Monodromy matrix $\frac{\partial \mathbf{x}}{\partial \boldsymbol{\eta}}(T, \boldsymbol{\eta})$, known as the Floquet multipliers λ_i, and determines stability of the underlying periodic solutions $\boldsymbol{x}(T, \boldsymbol{\eta})$ for a non-autonomous system, such as the SVEH, and the type of bifurcations they undergo as follows:

- If all multipliers λ_i are located inside the unit circle of the complex plane, Figure 4.15, then the periodic solution is stable
- If any multipliers λ_i is located outside the unit circle, then the periodic solution is unstable
- If a multiplier λ_i exists the unit circle through +1, Figure 4.15, then the system experiences a cyclic-fold (CF), transcritical, or symmetry-breaking (SB) bifurcation on the number and stability of the solution available either side of the bifurcation point.
- If a multiplier λ_i exists the unit circle through -1, Figure 4.15, then the system experiences a period-doubling (PD) bifurcation
- If a conjugate pair of multipliers λ_i and $\bar{\lambda}_i$ exits the unit circle away from the real axis, Figure 4.15, then the system experiences a Hopf bifurcation (HB)

Typically, period-doubling bifurcation occur in succession, called cascade, as a control parameter α is varied. Feingenbaum constant δ which relates the distance among of succes-

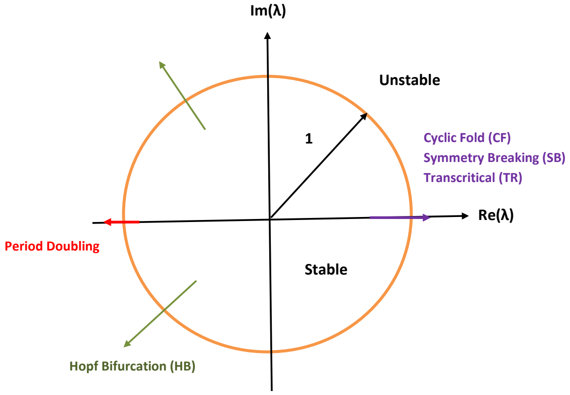

Figure 4.15: Floquet multipliers: Bifurcation and stability of periodic solutions

sive period-doubling bifurcations in a cascade [70]. Fiegenbaum showed that the distance among a sequence of period-doubling bifurcation along α scales according to a universal constant defined as;

$$\delta = \lim_{n \to \infty} \frac{\alpha_{n-1} - \alpha_{n-2}}{\alpha_{n-1} - \alpha_n} = 4.6629... \tag{4.23}$$

As we approach chaos (an aperiodic motion where $n \to \infty$), separating period doubling bifurcations gets the distance smaller by a factor approaching δ. Equation 4.23 will be used in the bifurcation analysis to calculate the Feingenbaum constant for period-doubling bifurcations.

Since the response of the SVEH consists of stable and unstable branches and a number of bifurcation points, one of the difficulties of running the shooting algorithm is to determine the path (branch) to follow after each bifurcation point. There are tools that claim to detect and compute the bifurcating branches automatically, such as AUTO97 [71], however these are very specialized tools guaranteed to work only for specific systems. The alternative and most assured way to determine the different branches at the system bifurcation points is to run the code implementing the shooting algorithm manually. This is performed by chasing a range of the control parameter, frequency or amplitude of base acceleration, and the iteration step size, the shooting algorithm is then executed over the specified range. The Floquet multipliers are monitored after each run to check when a change happens. The switch from stable to unstable branch happens when the Floquet multiplier exit the unit circle. The range of the bifurcation parameter is then updated and the process is repeated until the target control parameter range is covered and the stable and unstable branches are obtained.

4.5 Model Validation

In this section the model presented in section 4.1 is validated by matching numerical and experimental SVEH results. For validation, we compare the model response to the experimental results in the time and frequency domains. A procedure that uses Mathematica's Levenberg function, and the least squares method is used to identify the nonlinear damping b_n by minimizing the sum of the squares of the residuals, difference between measured and calculated mass displacement $x(t)$. We define the differential equation governing the harvester's dynamics as a function with b_n as a variable. The sum of the residuals is defined as the objective function to be minimized to find the best fit through the set of experimental points. was developed to estimate and the hard-stop stiffness k_2.

4.5.1 Time-Domain Validation

The time-response of the SVEH is obtained by integrating the harvester's equation of motion, Equation (4.12), for a given base acceleration. Figure 4.16 shows the open circuit waveform of 25 turns SVEH voltage obtained numerically and experimentally for accel-

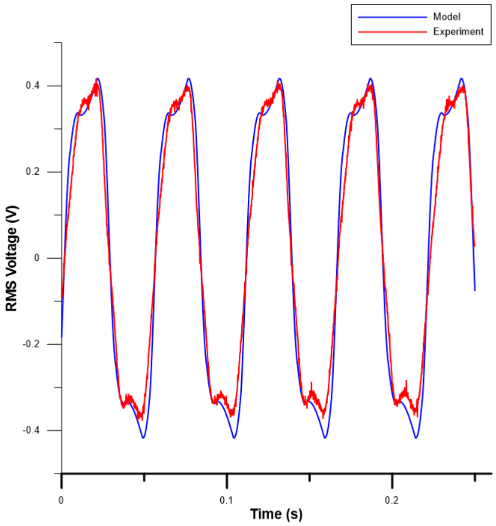

Figure 4.16: The 25 turns SVEH experimental and model open circuit voltage for input acceleration $A_\circ = 0.5\ g$ and frequency $\omega = 18\ Hz$s

eration amplitude $A_\circ = 0.5$ g and frequency $\omega = 18$ Hz. From the figure we observe a close match between numerical and experimental results, which indicate that the model captures and reproduces the behavior of the SVEH throughout the harvesting cycle.

Detailed analysis of the harvester time-domain response is carried out to investigate the underlying causes for the anharmonic output voltage waveform along the impacting branch. The seismic mass displacement $x(t)$, the base displacement $y(t)$, and the output voltage $V(t)$ were obtained numerically for base acceleration amplitude $A_\circ = 0.5\,$g and a frequency along the impacting branch ($\omega = 18.89\,$Hz) and another along the non-impacting branch ($\omega = 22\,$Hz). The results sre shown in Figures 4.17 and 4.18, respectively. Comparing the waveforms of the displacement and voltage along the impacting branch, Figure 4.17, show that voltage reversal occurs in the vicinity of maximum displacement, while the mass engages the walls. The trough between each two similar-signed peaks in the voltage

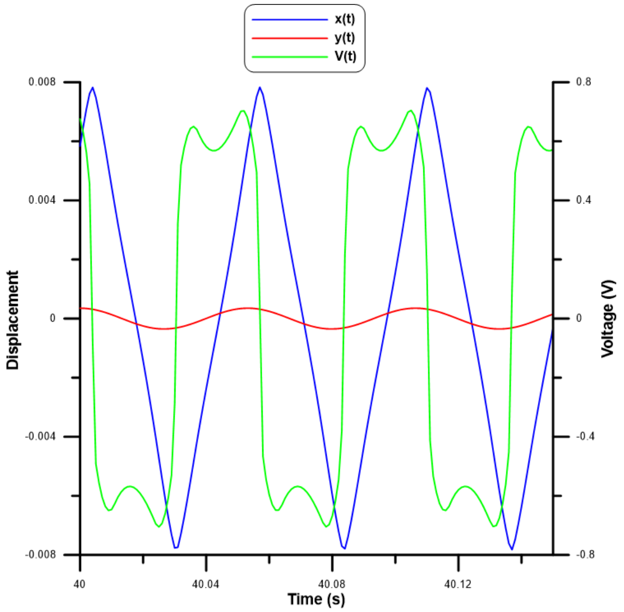

Figure 4.17: The 25 turns SVEH seismic mass displacement $x(t)$, base displacement $y(t)$, and output voltage $V(t)$ for base acceleration amplitude $A_\circ = 0.5\ g$ and frequency $\omega = 18.89\,\mathrm{Hz}$

waveform is due to mechanical and electromagnetic energy losses along the track as the mass rebounds away from the wall. Because the phase angle between the mass and base displacements is small, as the mass crosses the origin those losses dominate the energy supplied by the base. As the mass approaches the other wall, the energy supplied by the base grows fast and dominates energy losses, thereby increasing the mass velocity and leading to a second peak in the waveform just before impact with the wall.

On the other hand, all the waveforms of the non-impacting orbit at $\omega = 22\,\mathrm{Hz}$ are harmonic, Figures 4.18. The phase delay between the seismic mass and base displacements is almost 180°, indicating that the mass merely follows base acceleration (forcing). This is a characteristic of all orbits along the non-impacting branch. We conclude that the

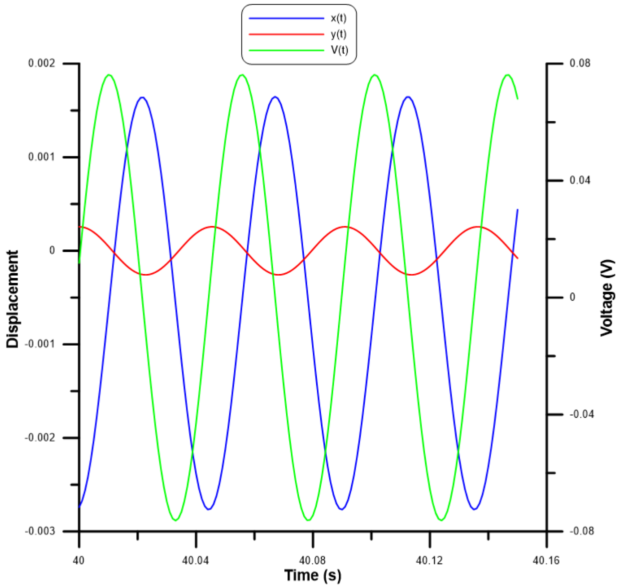

Figure 4.18: The 25 turns SVEH seismic mass displacement $x(t)$, base displacement $y(t)$, and output voltage $V(t)$ for base acceleration amplitude $A_\circ = 0.5\ g$ and frequency $\omega = 22\,\mathrm{Hz}$

box-like double-peak voltage waveform is a fundamental characteristic of desirable SVEH orbits indicating high energy harvesting along the impacting branch.

Figure 4.19 shows the Fast Fourier Transforms (FFT) of the impacting (blue) and non-impacting (red) SVEH waveforms. The FFT of the impacting waveform shows peaks at the forcing frequency, $\omega = 18.8$ Hz, as well as higher harmonics at $2\,\omega$ and $3\,\omega$, with significant peak at $3\,\omega$. The FFT of the non-impacting waveform shows a single peak at the forcing frequency. The existence of $2\,\omega$ peak is due to the existence of quadratic nonlinearity in the system, while 3ω is due to a cubic nonlinearity. The existence of a hardening cubic nonlinearity is expected due the existence and symmetry of the hard stops (k_2) at the walls [61, 72]. The quadratic nonlinearity appears due to the electromagnetic field distribution

[37].

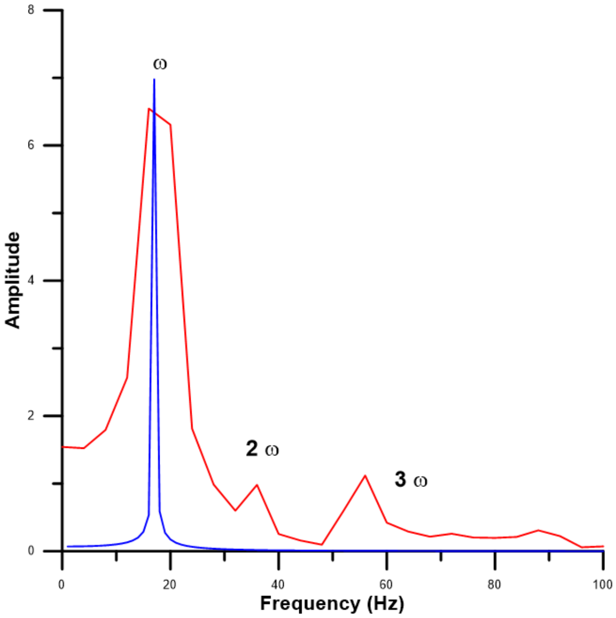

Figure 4.19: FFT of 25 turns SVEH response for base acceleration $A_\circ = 0.5$ g and frequency $\omega = 18.8$ Hz

4.5.2 Frequency-Domain Validation

Figure 4.20 shows the experimental and numerical frequency-response curves of the SVEH for base acceleration amplitude $A_\circ = 0.5$ g in the frequency range 4–25 Hz. The frequency-response curves are made of two branches, an impacting branch that jumps down to a non-impacting branch at $\omega = 18.945$ Hz for the experimental curve and $\omega = 18.5$ Hz for the numerical curve. Comparison of the two curves shows that the model captures the main features of the harvester response including switching between impacting and non-impacting oscillations.

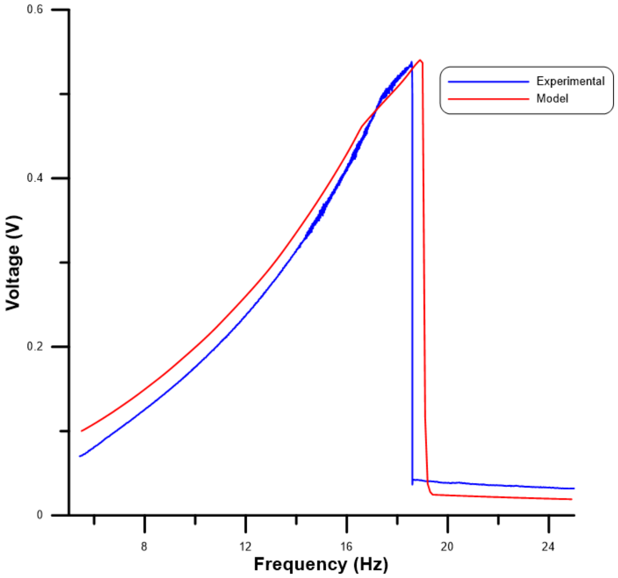

Figure 4.20: The 25 turns SVEH experimental and numerical frequency response curves for base acceleration amplitude of $A_\circ = 0.5\ g$

The numerical frequency-repose and phase curves of the 25 turns SVEH for base acceleration amplitude $A_\circ = 0.5\ g$are shown in Figure 4.21. The phase curve shows the phase delay of the mass displacement with respect to the base displacement. The phase delay of the mass increase form a low number along the impacting branch to reach 107° at the peak. On the other hand, the phase difference along the non-impacting branch is almost 180°.

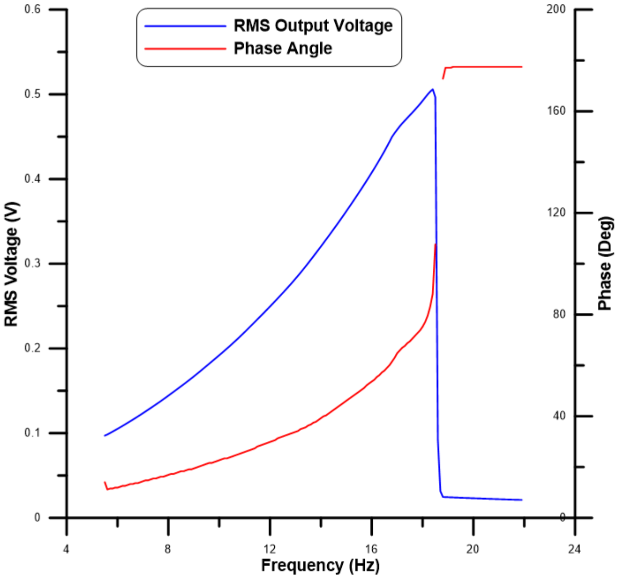

for base acceleration amplitude $A_\circ = 0.5\ g$

Figure 4.21: The 25 turns SVEH numerical frequency-response and phase curves for base acceleration amplitude $A_\circ = 0.5\ g$

4.6 SVEH Analytical Solution

The averaging method is used to obtain an approximate closed-form periodic solution of the harvester's equation of motion [73], Equation (4.7). We seek a solution in the form:

$$x(t) = a\ \sin(\Omega\, t + \beta) \tag{4.24}$$

where a and β are slowly varying amplitude and phase. Differentiating Equation (4.24) with respect to time we obtain;

$$\dot{x}(t) = a\, \Omega\ \cos(\Omega\, t + \beta) \tag{4.25}$$

subject to the constraint:

$$\dot{a}\ \sin\phi + a\, \dot{\beta}\ \cos\phi = 0 \tag{4.26}$$

where $\phi = \Omega\,t + \beta$. Substituting Equations (4.24) and (4.25) in Equation (4.7), we obtain a second constraint:

$$\begin{aligned}&\Omega\,\dot a\cos\phi + 2\,a\,\Omega\,\zeta_1\cos\phi + 2\,a^3\,\Omega\,\zeta_2\,\cos\phi\,\sin(\phi)^2 \;+ F(\phi) = \\ &a\,\Omega + \dot\beta)\sin\phi + A\,\cos(\Omega\,t).\end{aligned} \tag{4.27}$$

Solving Equations (4.26) and (4.27) for $\dot a$ and $\dot\beta$ yields the modulation equations governing the evolution of a and β:

$$\begin{aligned}\dot a &= \frac{\cos(\phi)}{\Omega}\Big[-2a^3\zeta_2\Omega\sin^2(\phi)\cos(\phi) - 2a\zeta_1\Omega\cos(\phi) + a\Omega^2\sin(\phi) + A\cos(\beta-\phi) - F(\phi)\Big] \\ a\,\dot\beta &= -\frac{\sin(\phi)}{\Omega}\Big[-2a^3\zeta_2\Omega\sin^2(\phi)\cos(\phi) - 2a\zeta_1\Omega\cos(\phi) + a\Omega^2\sin(\phi) + A\cos(\beta-\phi) - F(\phi)\Big]\end{aligned} \tag{4.28}$$

Next, we use Equation (4.24) to write the phase angle as: $\phi = \arcsin(\frac{x}{a})$. The restoring force can then be written in terms of the phase angle as [74].

$$F(\phi) = \begin{cases} 0 & 0 \le \phi \le \phi_1 \\ a\sin\phi - \alpha_1 & \phi_1 \le \phi \le \phi_2 \\ a\gamma\sin\phi + \alpha_2(1-\gamma) - \alpha_1 & \phi_2 \le \phi \le \pi - \phi_2 \\ 0 & \pi - \phi_1 \le \phi \le \phi_1 + \pi \\ a\sin\phi + \alpha_1 & \phi_1 + \pi \le \phi \le \phi_2 + \pi \\ a\gamma\sin\phi + \alpha_2(\gamma - 1) + \alpha_1 & \phi_2 + \pi \le \phi \le 2\pi - \phi_2 \\ a\sin\phi + \alpha_1 & 2\pi - \phi_2 \le \phi \le 2\pi - \phi_1 \\ 0 & 2\pi - \phi_1 \le \phi \le 2\pi \end{cases} \tag{4.29}$$

where

$$\phi_1 = \sin^{-1}\left(\frac{\alpha_1}{a}\right), \quad \phi_2 = \sin^{-1}\left(\frac{\alpha_2}{a}\right)$$

are the phase angles corresponding the seismic mass engaging the linear spring at $x = x_s$ and the fully compressed spring at $x = x_c$, respectively. The diagram shown in Figure 4.22 illustrates the transformation of the restoring force expression from x to ϕ.

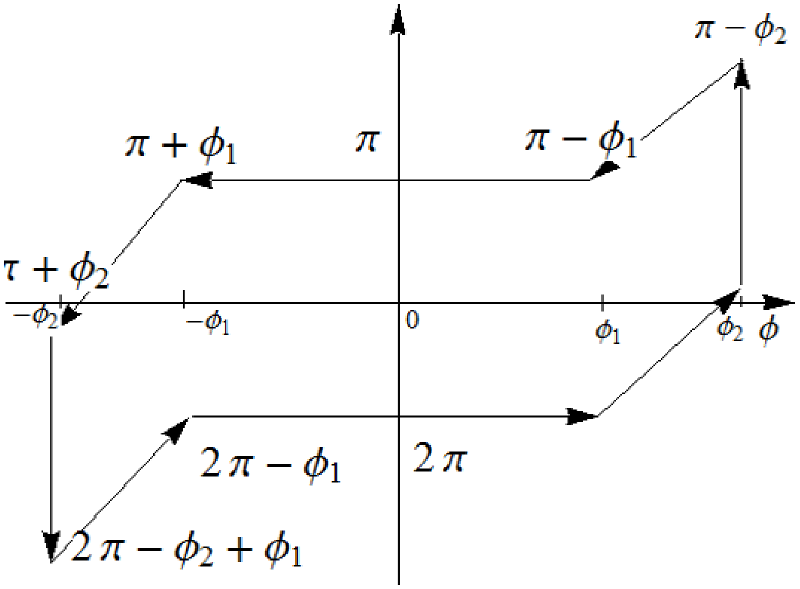

Figure 4.22: Phase transformation diagram

Integrating Equations (4.28) over a period of the fast time-scale $(0,\, 2\pi)$ and averaging the result we obtain the modulation equations

$$\begin{aligned} \dot{a} &= -\frac{1}{4}a^3\,\zeta_2 - a\,\zeta_1 + \frac{A\,\cos(\beta)}{2\Omega} \\ a\,\dot{\beta} &= \frac{1}{2\pi\, a\,\Omega}\Big[-2\alpha_2(\gamma-1)\sqrt{1-\frac{\alpha_2^2}{a^2}} - 2\alpha_1\sqrt{1-\frac{\alpha_1^2}{a^2}} \\ &\quad + a\left(-2(\gamma-1)\sin^{-1}\left(\frac{\alpha_2}{a}\right) - 2\sin^{-1}\left(\frac{\alpha_1}{a}\right) + \pi\,\gamma\right)\Big] \\ &\quad - \frac{a\,\Omega^2 + A\,\sin(\beta)}{2a\,\Omega} \end{aligned} \tag{4.30}$$

We define a detuning parameter σ describing the difference between the forcing frequency

Ω and the normalized natural frequency as

$$\Omega = 1 + \sigma$$

we rewrite the modulation equations in autonomous form as

$$\begin{aligned}
\dot{a} =& -\frac{1}{4}a^3\,\zeta_2 - a\,\zeta_1 + \frac{A\,\cos(\beta)}{2(\sigma+1)} \\
a\,\dot{\beta} =& \frac{1}{2\,\pi\,a\,(\sigma+1)} - 2\alpha_2(\gamma-1)\sqrt{1-\frac{\alpha_2^2}{a^2}} - 2\alpha_1\sqrt{1-\frac{\alpha_1^2}{a^2}} \\
& + a\left(-2(\gamma-1)\sin^{-1}\left(\frac{\alpha_2}{a}\right) - 2\sin^{-1}\left(\frac{\alpha_1}{a}\right) + \pi\,\gamma\right) \\
& - \frac{a\,(\sigma+1)^2 + A\,\sin(\beta)}{2a\,(\sigma+1)}
\end{aligned} \tag{4.31}$$

Steady-state periodic oscillations of the harvester correspond to fixed points (a_0, β_0) of the modulation Equations (4.31). These equations are solved numerically for the fixed points as a function of the detuning parameter σ.

The harvester response obtained from the modulation equations, Equation (4.24), is compared to its response obtained from the shooting method is shown in Figures 4.25 and 4.24 for $\Omega = 1$. Figure 4.25 shows the seismic mass displacement and Figure 4.24 shows its velocity as functions of time. The response obtained analytically, from time averaging, is shown in blue lines and that obtained numerically, from the shooting method, is shown in red lines. The results show that the analytical solution captures the amplitude and frequency but not the waveform of the response. The existence of higher harmonics in the impact oscillator response requires the use of more than one fast-time harmonic in the assumed solution, Equation (4.24).

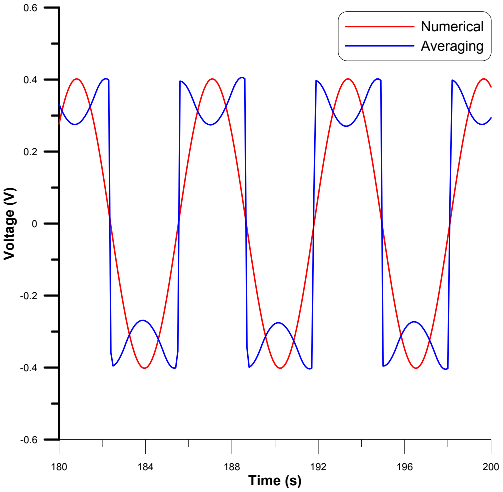

Figure 4.23: The numerical (red) and analytical (blue) output voltage for base acceleration amplitude and frequency of $A_0 = 0.6$ g and $\omega_n = 19.62\,\text{Hz}$

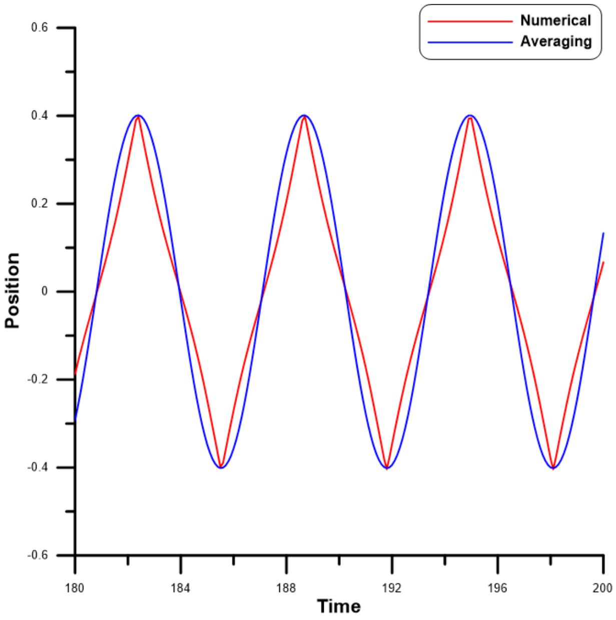

Figure 4.24: The numerical (red) and analytical (blue) displacement of the seismic mass m for base acceleration amplitude and frequency of $A_0 = 0.6$ g and $\omega_n = 19.62\,\mathrm{Hz}$

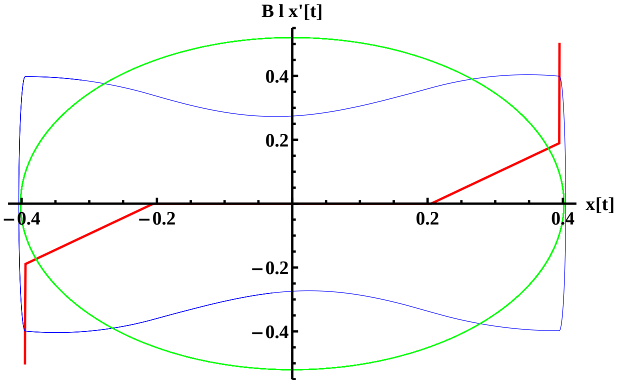

Figure 4.25: Numerically (blue) and analytically (green) obtained SVEH orbits for a base acceleration amplitude and frequency of $A_0 = 0.6$ g and $\omega_n = 19.62\,\mathrm{Hz}$

4.7 Bifurcation Analysis

As the SVEH seismic mass moves between the two end limiters, its motions settle down on various impacting and non-impacting attractors. We deploy bifurcation analysis to search the parameter space of environmental vibrations for regions where attractors amenable to energy harvesting are available. This is achieved by constructing bifurcation diagrams as a control parameter, frequency or amplitude of base acceleration, is varied.

Frequency Bifurcation Diagram: The bifurcation diagram for the frequency of base accelerations, Figure 4.26, is constructed by setting the amplitude to $A_\circ = 0.5$. The figure shows the existence of stable (solid line) and unstable (dashed line) branches, a number of bifurcations, and a region of multivaluedness.

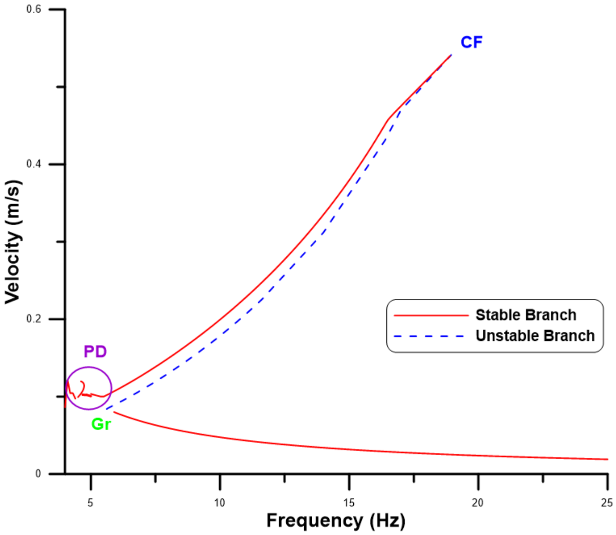

Figure 4.26: The SVEH frequency bifurcation diagram for base acceleration amplitude of $A_\circ = 0.5\,\mathrm{g}$

The grazing bifurcation (Gr) at $Gr = 5.5$ Hz signifies a fundamental change in the harvester response. At this bifurcation point the seismic mass touches the spring with zero velocity. As a result, the non-impacting (lower stable) branch is born to the right of Gr. It corresponds to the frequency where the amplitude of base displacement is equal to the free track length $x_L = \frac{A_\circ}{Gr^2}$. Beyond the grazing bifurcation point ($\omega \geq Gr$), the amplitude of base displacement becomes smaller than the track length, which allows for stable non-impacting oscillations, such as that shown in Figure 4.27(b), to appear. We note that the non-impacting branch is obtained through long time integration since it does not involve a restoring force, and therefore lacks a stiffness term, leading to a a one-state equation of motion and a singular Jacobian matrix, therefore precluding the use of the shooting method as defined in Equation (4.22).

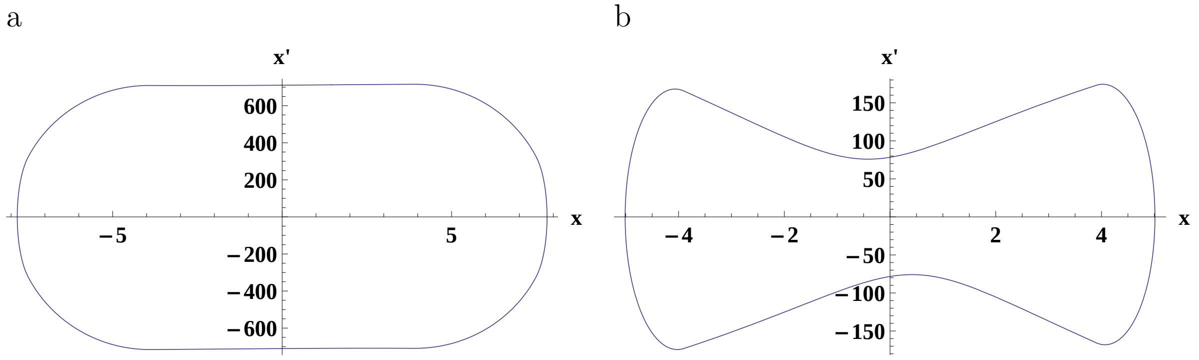

Figure 4.27: Phase portraits of a) the stable impacting orbit at $\omega = 18.89$ and b) stable non-impacting orbit at $\omega = 19.84$ Hz

Two impacting branches, Figure 4.27, coexist with the non-impacting branch beyond the grazing bifurcation point. The larger is a stable impacting branch while the smaller is an unstable impacting branch. The two impacting branches meet and disappear at a cyclic-fold bifurcation at $CF_1 = 18.945$ Hz. Along the large stable branch, the harvester output voltage grows as the frequency of base acceleration increases. This is apparent in Figure 4.28 where the size of the blue orbits grows with increase in frequency. The unstable branch stretches between the cyclic-fold at $CF_1 = 18.945$ Hz and 5.5 Hz where it disappears.

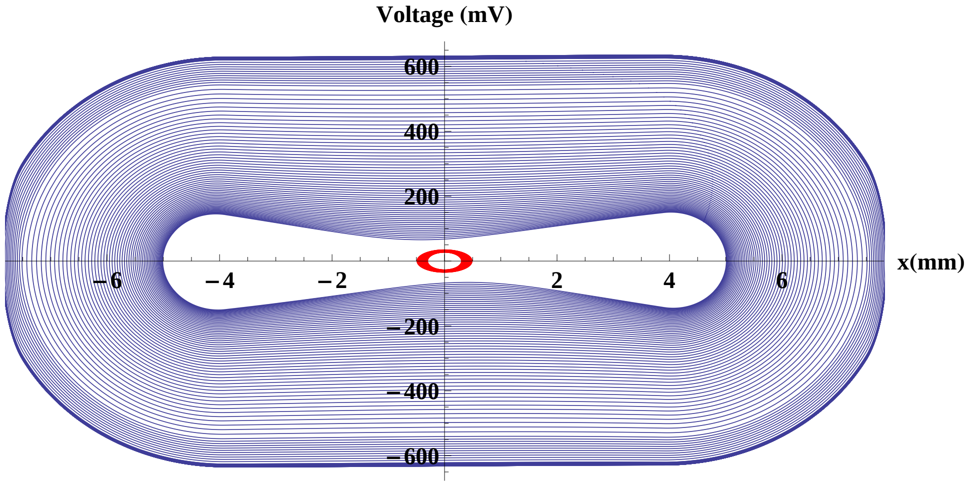

Figure 4.28: Impacting orbits (blue) grow with frequency (5.5−18.945 Hz). Non-impacting orbits (red) shrink as frequency is increased beyond the CF bifurcation (18.945 − 25 Hz)

When the frequency is increased beyond $CF_1 = 18.945$ Hz the response jumps down to the lower stable (non-impacting) branch. Experimental and numerical results, Figures 4.7 and 4.26, indicate that the basin of attraction of the non-impacting branch shrinks as the frequency of base acceleration approaches CF_1. As the frequency of base acceleration is decreased from values larger than CF_1, the harvester response follows the non-impacting branch before jumping up to the stable impacting branch. We found that the jump consistently occurs before reaching the grazing bifurcation point Gr due to external disturbances.

An estimate for the grazing bifurcation $\hat{Gr}$ can be obtained by noting that at this point the non-impacting orbit fills the track length x_t touching the end springs with velocity zero. We can write the linearized equation of motion at $\hat{Gr}$ as

$$\ddot{x} + 2\zeta\,\omega_n\,\dot{x} = A_\circ\,\cos(2\pi\,\hat{Gr}\,t) \tag{4.32}$$

assuming a harmonic response $x(t) = d\,\cos(2\pi\,\hat{Gr}\,t - \phi)$, and substituting it into the equation of motion to obtain

$$4\pi^2\,d\,\hat{Gr}^2\,\cos(2\pi\,\hat{Gr}\,t + \phi) + 4\zeta_1\,\pi\,\hat{Gr}\,d\,\sin(2\pi\,\hat{Gr}\,t + \phi) = A_\circ\cos(2\pi\,\hat{Gr}\,t)$$

Therefore, we can write

$$16\,\pi^4\,d^2\,\hat{Gr}^4 + 16\,{\zeta_1}^2\,\pi^2\,\hat{Gr}^2\,d^2 = A_\circ^2$$

and obtain a closed form estimate of $\hat{Gr}$ as:

$$\hat{Gr} = \frac{1}{2\pi}\sqrt{\frac{\sqrt{d^2\,\left(A_\circ^2 + 4\,d^2\,\zeta_1^2\right)} - 2d^2\,\zeta_1^2}{d^2}}$$

In fact, as base acceleration amplitude is increased, thereby providing an environment richer in external disturbances, this jump happens at earlier points in the sweep down further away from the grazing bifurcation, Figure 4.7 and Table 4.5. Furthermore, at higher base acceleration amplitudes, the the RMS voltage output is non-smooth, Figure 4.7, indicating outbursts of higher output voltage impacting orbits within the regular lower output voltage non-impacting orbits.

As the frequency of base acceleration is decreased along the stable impacting, the SVEH response exhibits complex dynamics, Figures 4.29. First, the impacting oscillations undergo a symmetry-breaking bifurcation at $SB = 5.471\,\text{Hz}$. The symmetric orbit, 4.30, then disappears via the cascade of period-doubling bifurcations PD listed in Table 4.6. After the third period doubling bifurcation, a period-eight orbit (P8) emerges at $PD8 = 4.681$ Hz only to disappear at $\omega = 4.68$ Hz.

Table 4.5: Jump-Up location along the non-impacting branch

$A_\circ$ (g)	$\hat{Gr}$ (Hz)	Jump-Up (Hz)
0.3	3.09	6.84
0.4	3.57	8.51
0.5	3.99	10.05
0.6	4.37	12.3

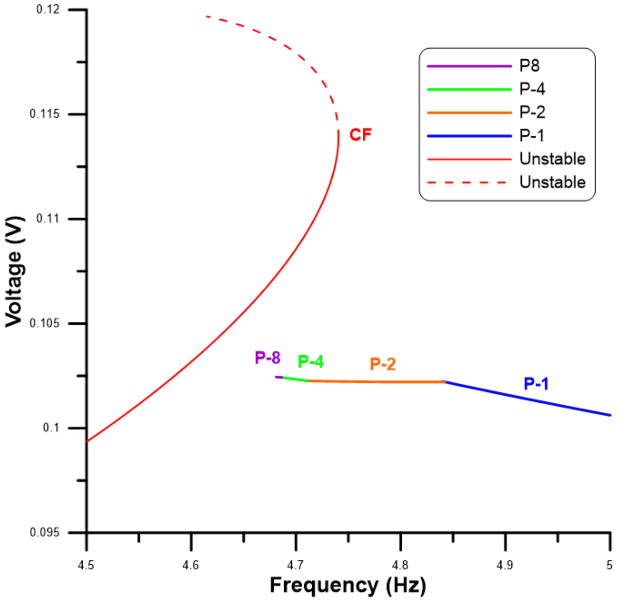

Figure 4.29: The SVEH bifurcation diagram for input acceleration $A_\circ = 0.5\ g$

Using the control parameter ω values listed in Table 4.6 and Equation (4.23), we determine the Fiegenbaum number δ_1 as;

$$\delta_1 = \frac{P4 - P2}{P8 - P4} = 4.349 \tag{4.33}$$

which is close to the Feugenbaum universal constant $\delta = 4.669201$.The difference is due to the fact that the universal constant δ is the limit of the ratio of successive period-doubling

Table 4.6: Bifurcation points in the frequency bifurcation diagram

Bifurcation Point	Base acceleration amplitude (g)
CF_1	18.9451
Gr	5.5934
SB	5.471
CF_2	4.7453
PD1	5
PD2	4.84207
PD4	4.7111
PD8	4.6805

bifurcations as the number of period-doubling bifurcations approaches infinity.

At lower frequencies, two isolated impacting branches are available, a small stable branch and a large unstable branch. They meet at a cyclic-fold bifurcation at $CF_2 = 4.7453$ Hz and disappear beyond this point. The isolated branches co-exist with the terminal stretch of the period doubling cascade.

We conclude that the optimal region for energy harvesting (resonant) branch between the symmetry-breaking bifurcation $SB = 5.471\,\text{Hz}$ and the cyclic-fold (CF) at $CF_1 = 18.95$ Hz. As the base acceleration frequency drops below SB the size of the orbits shrink significantly as indicated by the change in the slope of the RMS voltage-frequency curve in Figure 4.26. In addition, the dynamics of the harvester become more complex encountering a cascade of period-doubling bifurcations and another branch of stable orbits. In this region, the harvester's output voltage is significantly reduced, which is an undesirable operating condition.

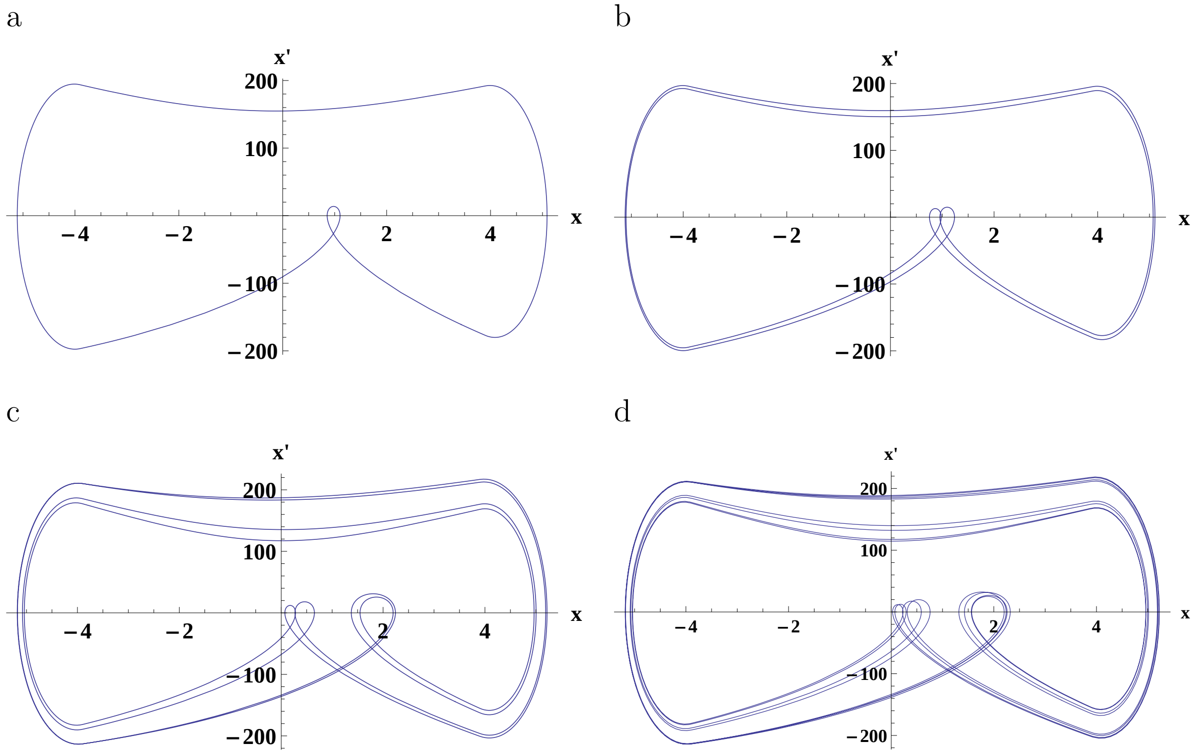

Figure 4.30: Phase portraits of orbit on a) the upper stable branch, b) lower stable branch, a) P1 at $\omega = 5$ Hz, and b) P2 at $\omega = 4.84$ Hz , c) P4 at $\omega = 4.71$ Hz, and d) P8 at $\omega = 4.68$ Hz.

Force Bifurcation Diagram: The bifurcation diagram shown in Figure 4.31 presents the RMS voltage of the harvester as the base acceleration amplitude varies from $A_\circ = 0.1$ to 0.2 g, while the acceleration frequency is held constant at $\omega = 6.5$ Hz. A branch of stable non-impacting orbits appears at $A_\circ = 0.1$ g and terminates at the grazing bifurcation. It coexists with a branch of larger (impacting) stable orbits. The impacting branch is born out of a cyclic-fold bifurcation at $A_\circ = 0.103$ g. A branch of stable non-impacting orbits is present at $A_\circ = 0.1$ g and terminates at the grazing bifurcation. It coexists with a branch of larger (impacting) stable orbits. The impacting branch is born out of a cyclic-fold bifurcation at $CF = 0.103$ g. The grazing bifurcation appears at base acceleration amplitude $Gr = 0.6665$ g, for amplitudes larger than $(A_\circ \leq Gr)$ the stroke of the base displacement is larger than the free track length x_t, thereby precluding non-impacting orbits.

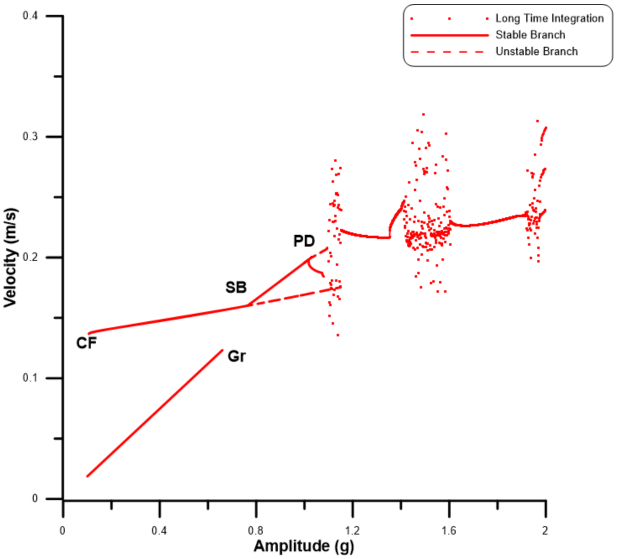

Figure 4.31: Bifurcation diagram for input frequency $\omega = 6.5$ Hz and $A_\circ = 0.1$ to 2 g

The only available response beyond the grazing bifurcation is a branch of symmetric impacting orbits. It undergoes a symmetry breaking bifurcation at $SB = 0.7631$ g, resulting in a branch of unstable symmetric orbits and a branch of stable asymmetric orbits. Figure 4.33(b) shows the asymmetric orbit (blue line) obtained at $A_\circ = 0.772$ g and its image (red line) under the symmetry transformation $(x \longrightarrow -x, \dot{x} \longrightarrow -\dot{x})$. The two orbits are not identical, which proves loss of symmetry.

As the acceleration amplitude is increased further, the branch of asymmetric orbits undergo a cascade of period-doubling bifurcations starting $PD1 = 1.019$ g and culminating

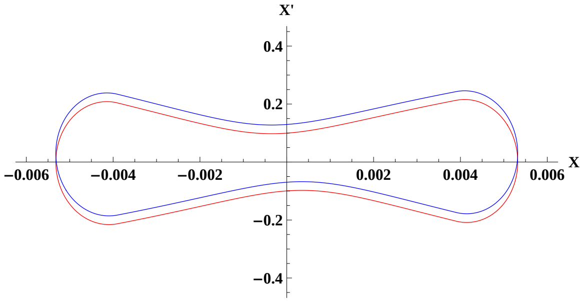

Figure 4.32: The asymmetric orbit at base acceleration amplitude $A_\circ = 0.772$ g

in a chaotic attractor at $A_\circ = 1.0959$ g. Selected orbits within the period doubling cascade are shown in Figure 4.7 demonstrating swift progression from P1 to P2, P4, P8, and P-16 orbits as $A_\circ$ increases. We note that these orbits are not suitable for energy harvesting, since the velocity, and therefore output voltage, of the seismic mass drops to cross zero along its path from the right to the left sides of the track. This can be seen in the bifurcation diagram where the RMS voltage drops beyond the first period doubling bifurcation.

Table 4.7: Location of bifurcation points in the amplitude bifurcation diagram

Bifurcation Point	Value (g)
CF	0.1
Gr	0.6665
SB	0.763
PD2	1.039
PD4	1.084
PD8	1.0938
PD16	1.0959

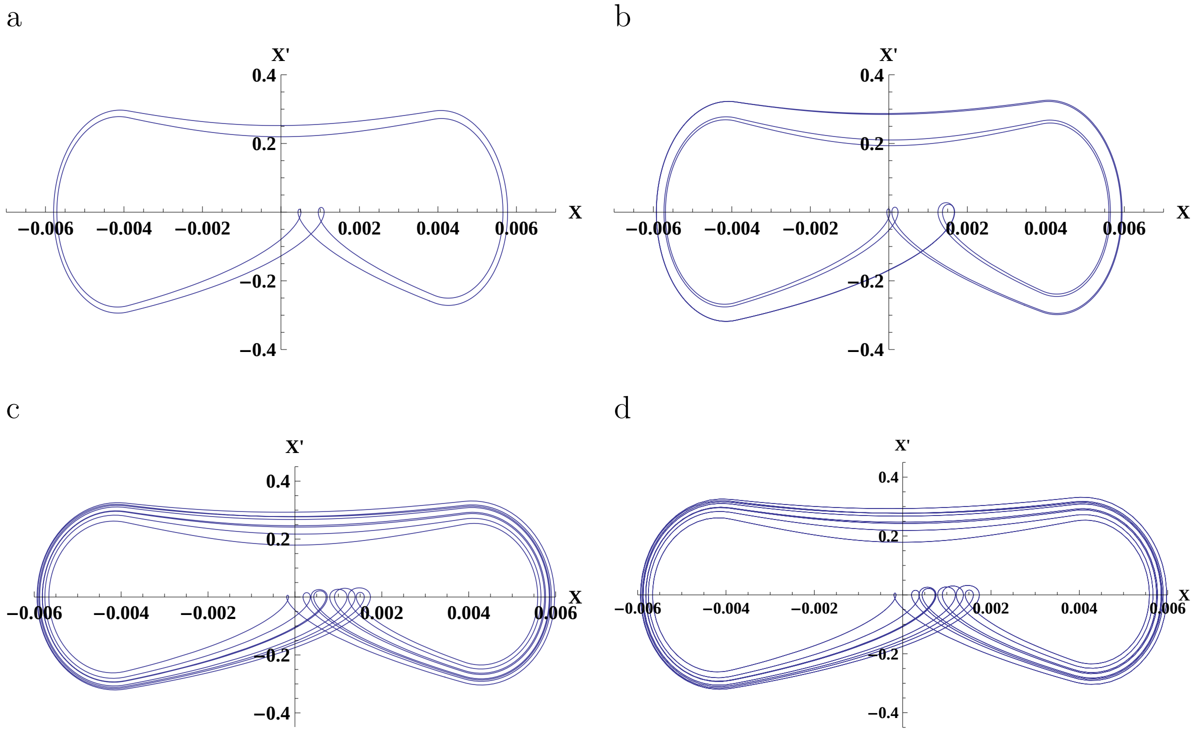

Figure 4.33: Phase-portrait orbits within the period-doubling cascade a) P2 at $A_\circ = 1.025$ g, b) P4 at $A_\circ = 1.084$ g, c) and P8 at $A_\circ = 1.094$ g, d) P16 at $A_\circ = 1.0959$ g

Using the locations period-doubling bifurcation listed in Table 4.7, and Equation (4.23), we determine the Feigenbaum numbers of the period-doubling cascade as

$$\delta_1 = \frac{PD4 - PD2}{PD8 - PD4} = 4.592 \tag{4.34}$$

and

$$\delta_2 = \frac{PD8 - PD4}{PD16 - PD8} = 4.666 \tag{4.35}$$

At the end of the period-doubling cascade, the SHEV lands on a chaotic attractor starting at $A_\circ \approx 1.1$ g and ending at $A_\circ \approx 1.2$ g. Beyond $A_\circ = 1.2$ g, a new stable branch is born followed by a number of bifurcations culminating in a wider second region of chaos.

We conclude that the harvester's optimal range of operation is along the stable impacting branch between the cyclic fold at $CF = 0.103$ g and the first period-doubling bifurcation at $PD1 = 1.019$ g. In this region, the output voltage of the harvester increases with base acceleration amplitude and reaches a maximum, ($V_{PD1} = 0.6$ V). At amplitudes larger than the first period-doubling bifurcation, the output voltage drops.

4.8 Comparison of Linear and Nonlinear VEHs

We investigate the value added by the SVEH architecture by comparing its performance to that of an equivalent linear vibration energy harvester (VEH), consisting of a magnetic seismic mass m permanently attached to a linear spring k_1. Similar mass moves along a linear guide with respect to a fixed coil when subjected to base excitations with no walls to limit its motions. The VEH equation of motion can be written as:

$$m\,\ddot{x} + (\hat{b_m} + b_e)\dot{x} + k_1\,x = -m\,\ddot{y} \tag{4.36}$$

where $\hat{b_m} = b_m + b_n$ and k_1, are identical to those of the SVEH.

Figure 4.35 shows the frequency response curves of the open-circuit RMS output voltage of the VEH and SVEH when excited by the same base acceleration amplitudes $A_\circ = 0.4, 0.5$ and 0.6 g over the frequency range $\omega = 5 - 25$ Hz. At base acceleration amplitude $A_\circ = 0.5$ g, the VEH's maximum output voltage is 558 mV obtained close to resonance ($\omega = \omega_n$), the SVEH produced output voltage is 537 mV using the model and 541 mV experimentally. The results for all base acceleration amplitudes are listed in Table 4.8.

The harvesting bandwidth of the SVEH exists along the impacting branch only. Whether the SVEH harvests energy within that frequency range depends on the current excitation it experiences and its response to previous excitations. On the other hand, the VEH harvests energy whenever the frequency of excitation lies within its harvesting bandwidth. With this caveat, we compare of the harvesting bandwidth of VEH to the SVEH's model and experimental bandwidths and find that the SVEH bandwidth is 300 % to 450 % wider than that of the VEH. Finally, we note that the response of the VEH to acceleration amplitudes $A_\circ = 0.6\,\mathrm{g}$ slightly exceeds that of the SVEH because motions of the VEH in the vicinity of its natural frequency $f = 19.9\,\mathrm{Hz}$ exceed the SVEH track length.

Table 4.8: Performance comparison among the LVEH model/ SVEH model/ SVEH experiment for three levels of base acceleration amplitude

Amplitude (g)	Peak Voltage (mV)	Bandwidth (Hz)
0.4	450/420/460	0.85/2.4/2.6
0.5	558/537/541	0.95/3.98/4.1
0.6	680/635/646	1.14/5.3/5.5

We define a figure of merit to describe a harvester's energy conversion efficiency as the integral of the output voltage $V(f)$ over the harvesting bandwidth weighed by the probability $P(f)$ of producing that voltage:

$$FoM = \int_{f_H}^{f_L} P(f)V(f)\,df \tag{4.37}$$

where f_L and f_H are the lower and upper ends of the harvesting bandwidth. For linear harvesters, $P(f) = 1$. For nonlinear harvesters, $P(f) < 1$ for frequencies where more than one stable response are available.

To determine $P(f)$ for the SVEH, we obtained the basins of attraction of available solutions at discrete base acceleration frequencies and amplitude $A_\circ = 0.5\,\mathrm{g}$. The basins of attraction were found by dividing the phase-space region ($x = -x_s \longrightarrow x_s, \dot{x} = -0.4 \longrightarrow 0.4$) into 250 evenly spaced pixels. The SVEH equation of motion, Equation (4.1), was integrated for 200 excitation periods $200\,T$ starting from an initial condition at the lower left corner of each pixel, and the RMS of the velocity in the last 8 periods was evaluated to represent the steady-state response in that pixel. Note the integration time was set larger than the settling time $> Q\,T$ to guarantee steady-state response. Without loss of generality, we calculated the probabilities of impacting orbits at four frequencies $f = 6.5$, 10, 13.5 and 14 Hz, and an averaged value over the frequency range 6.5–14/.Hz was used.

The basins of attraction at $f = 6.5$, 10, 13.5 and 14 Hz are shown in Figure 4.34. All basins of attraction were normalized such that 1 corresponds to the RMS velocity of the symmetric impacting orbit and 0 corresponds to the non-impacting orbit. Phase space was also normalized to ($x = -1 \longrightarrow 1, \dot{x} = -1 \longrightarrow 1$). Blue pixels correspond to resonant impacting orbits, white pixels correspond to non-impacting orbits, and green pixels correspond to a coexisting chaotic attractor available only in the $f = 6.5$ Hz basin of attraction. The basins of attraction at $\omega = 15$ and 18 Hz were also evaluated. It was found that region of interest in phase-space lies fully within the basin of attraction of the non-impacting orbit. On the other hand, experimental results show that the jump-down from an impacting orbit to a non-impacting orbit occurs at $\omega = 18.8$ Hz which indicates the presence of a finite uninterrupted basin of attraction for the impacting orbit in the frequency range 15–18.8 Hz. This discrepancy between numerical and experimental results indicate an over estimate of damping in the model.

From Table 4.9, we note that the efficiency of the SVEH is up to 232% better than that of the VEH.

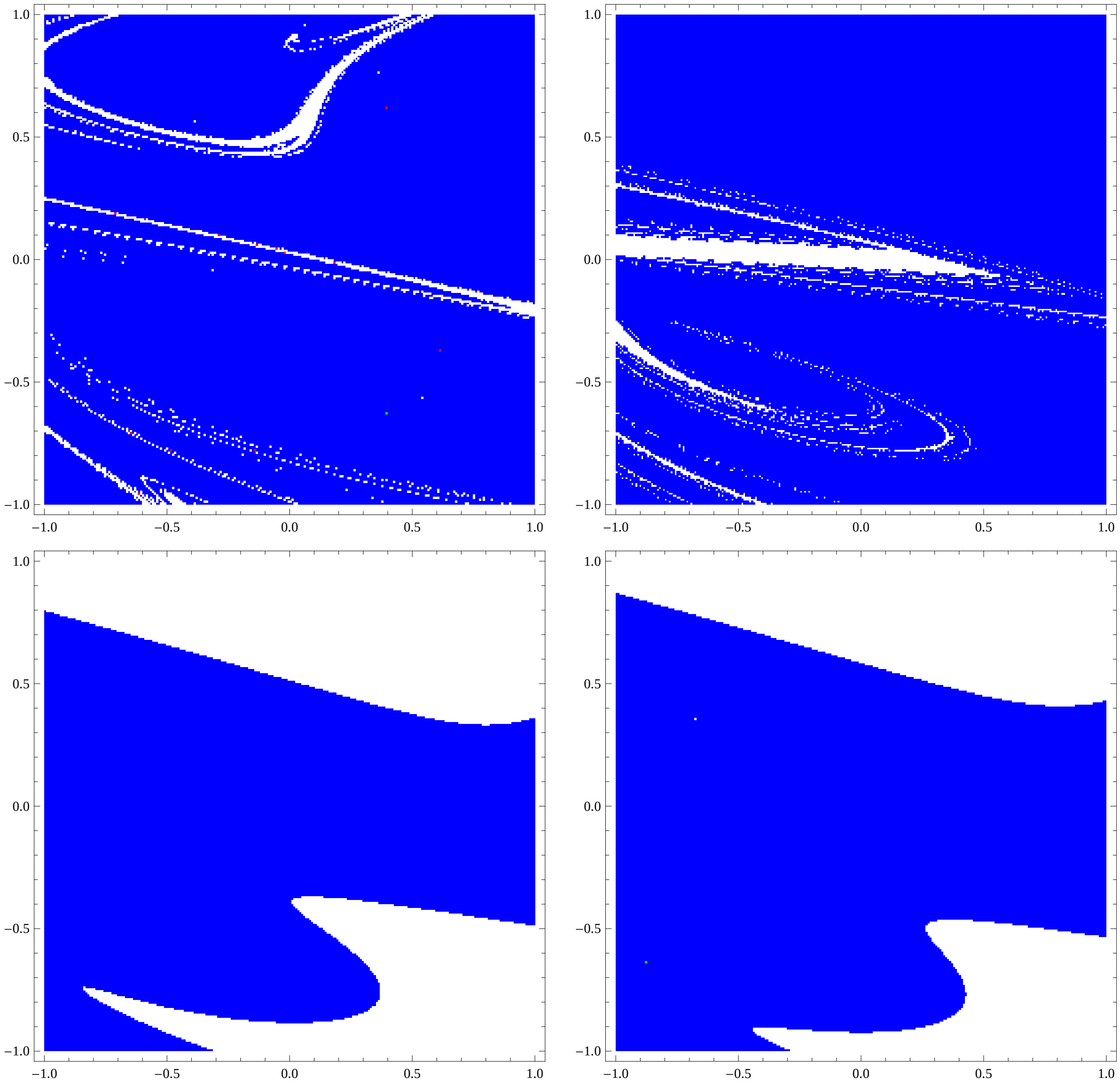

Figure 4.34: Basin of attraction for frequencies $\omega = 6.5$, 10, 13.5, and 14 Hz

Table 4.9: The SVEH efficiency in comparison with the VEH

$A_\circ$ (g)	VEH (mV.Hz)	SVEH (mV.Hz)	% Increase
0.4	0.446	1.035	92.4%
0.5	0.477	1.87	204.4%
0.6	0.534	2.26	232.2%

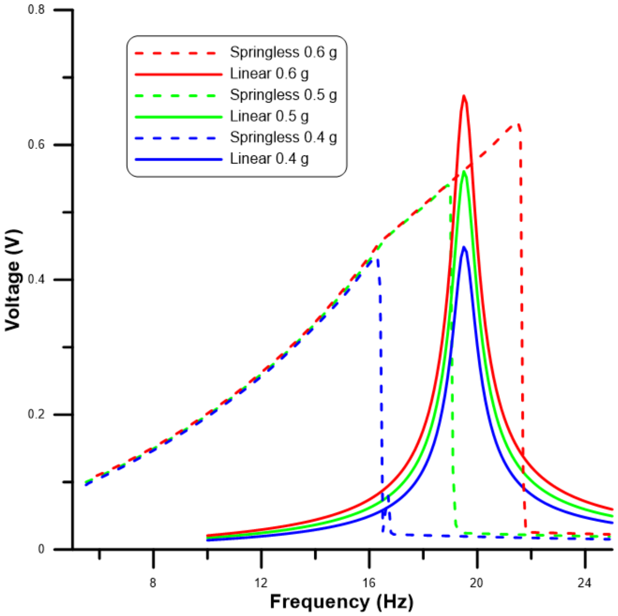

Figure 4.35: Frequency response curves of VEH and SVEH for amplitudes $A_\circ = 0.4$, 0.5, and 0.6 g

4.9 Summary

In this chapter, a model of the horizontal SVEH was developed and numerical and experimental results were presented. The shooting method in conjunction with the Floquet theory were used to perform bifurcation analysis of the base acceleration parameter space $(\omega, A_\circ)$. The Method of Averaging was then used to obtain an approximate close-form expressions for the harvester's response.

Experimental and numerical results show, the SVEH can harvest energy from vibrations with amplitudes as low as 0.1 g and frequencies in the range 5 and 19 Hz. The optimal output power of the horizontal harvester is 12 mW, using a 60 turns coil, and the corresponding optimal load is 4.4 Ω. Experimental and numerical results are in agreement, which indicate that the model is a good representation of the SVEH and can be used to analyze and optimize its design.

Bifurcation analysis revealed that the harvester is efficient in harvesting vibrations in the upper branch of the frequency-response curve, which is approximately in the range 5 to 19 Hz. Above 19 Hz and below 5 Hz, the dynamics of the harvester become complex (period-doubling cascade, acyclic-fold, and symmetry breaking bifurcations) and its energy harvesting capabilities suffer as a consequence.

Base acceleration amplitude bifurcation analysis revealed that the SVEH can harvest energy from amplitudes between 0.1 and 1 g. As the base acceleration amplitude is increased above 1 g, the response of the harvester starts to exhibit complex dynamics, such as period doubling and chaos, that reduce the harvested power significantly.

Chapter 5

Vertical SVEH

The vertical configuration of the SVEH is suitable for environments where motions are predominantly in the vertical direction. In this chapter we study the response of harvester in the vertical configuration. Experimental results of SVEH showed that, depending on the magnitude of base acceleration, the harvester possesses three distinct regions of operation; linear, single-impact and double-impact. Experimental and numerical results of the vertical SVEH, in all three regions of operation, are presented and analyzed.

5.1 Vertical SVEH

Figure 5.1 shows a schematic of the vertical SVEH. In this configuration, the linear guide is aligned vertical along the direction of gravity of ($\theta = 90°$). The seismic mass moves in the vertical direction when subjected to base accelerations. For low base acceleration amplitudes, the seismic mass remains attached to the lower spring throughout motion and the oscillation are essentially linear in response to low amplitude base accelerations.

For moderately larger amplitudes, the mass is detached from the lower spring without impacting the upper one. In this region, the seismic mass bounces up and down in response to base accelerations impacting the lower spring in the process. For significantly higher amplitudes, the mass impacts both springs during motion and its response is that of a double-impact oscillator.

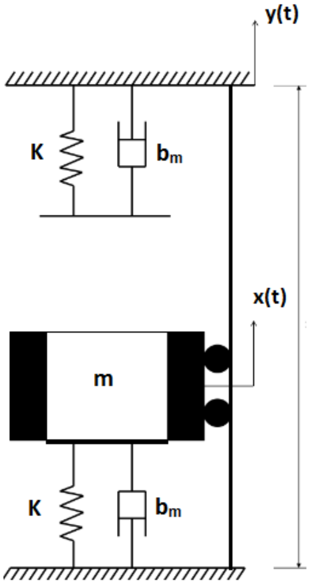

Figure 5.1: Schematic of the Vertically-aligned SVEH

The equation of motion of the vertical SVEH can be obtained form Equation (3.2)

$$m\,\ddot{x} + (b_e + b_m)\;\dot{x} + F_{st}(x) + m\,g\;=-\,m\,\ddot{y} \tag{5.1}$$

The seismic mass m is treated as a point mass, as shown in Figure 5.1. The origin of the coordinate system is placed at the point where mass m rests on the lower spring. The restoring force $F_{st}(x)$ varies with the position of the seismic mass m according to the piecewise function:

$$F_{st}(x) = \begin{cases} 0 & 0 \leq x \leq x_t \\ k_1 x & x_c - x_s < x \leq 0 \\ k_1(x_c - x_s) + & \\ k_2(-x_c + x_s + x) & -x_s \leq x \leq x_c - x_s \\ k_1(x - x_t) & x_t < x < -x_c + x_s + x_t \\ k_1(x_s - x_c) + & -x_c + x_s + x_t < x < x_s + x_t \\ k_2(x_c - x_s - x_t + x) & \end{cases} \tag{5.2}$$

The force-displacement relationship describing the stiffness of the vertical harvester is shown in Figure 5.2. The mechanical damping coefficient b_m is calculated experimentally from the SVEH's experimental frequency-response curve when operating in the linear regime. The quality factor Q of the SVEH is defined as:

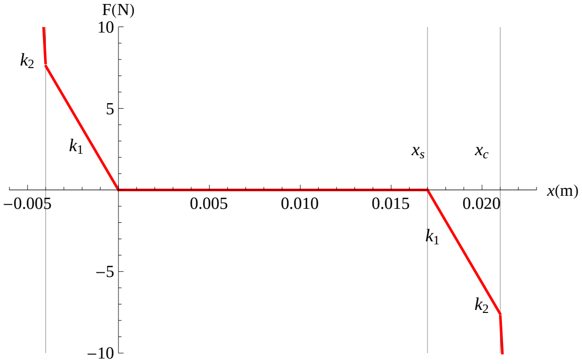

Figure 5.2: Restoring force-displacement relationship

$$Q_m = \frac{f_0}{\Delta f} \tag{5.3}$$

where f_0 is the center frequency, $\Delta f = f_2 - f_1$, and f_1 and f_2 are the two half-power frequencies. The quality factor for the open-loop harvester Q_m, where $b_e = 0$, is then used to calculate the b_m using the following formula;

$$Q_m = \frac{m\,\omega}{b_m} \tag{5.4}$$

The center frequency and half-power bandwidth were found from the frequency-response curve for the base acceleration amplitude of $A_\circ = 0.05\,\mathrm{g}$. The linear mechanical damping of the harvester was calculated from Equation 5.3 $b_m = 1.16\,\mathrm{kg/s}$. The values of the VEH's parameters are listed in Table 5.1.

Table 5.1: Dynamic parameters of the SVEH

Parameter	Value
Mass m (kg)	0.12
Stiffness k_1 (N/m)	950
Center Frequency f_0 (Hz)	21
Low cut off frequency f_1 (Hz)	20.2
High cut off frequency f_1 (Hz)	22.5

5.2 Experimental Results

A prototype of the 25 turns SVEH is mounted on an electromagnetic shaker as shown in Figure 5.3, and base acceleration is applied as input excitation while the open-circuit voltage across the harvester's coil terminals is measured.

Experimental frequency-response curves of the harvester for different base acceleration amplitudes were used to identify the SVEH's regions of operation. The results show that for base acceleration amplitudes in the range $(A_\circ \leq 0.1\,g)$ the response is linear. For moderate base acceleration amplitudes ($0.1\,g < A_o < 0.5\,g$), the SVEH's response is that of a single-impact oscillator (mass impacts on the lower spring). For high base acceleration amplitudes ($A_o > 0.5\,g$), the SVEH's response is that of a double-impact oscillator (mass impacts on the upper and lower springs).

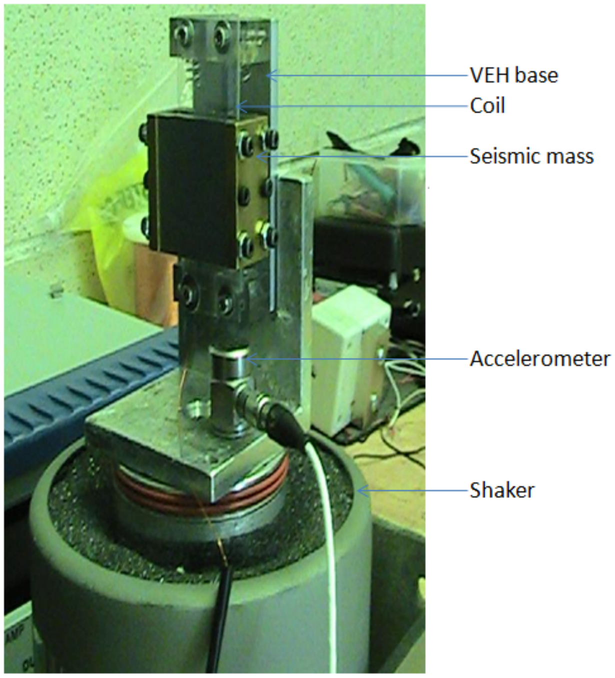

Figure 5.3: Experimental setup of the vertical SVEH

5.2.1 Linear Regime: $A_\circ \leq 0.1$ g

In this case, the mass remains in contact with the lower spring and its response is that of a forced, damped single degree of freedom spring-mass-damper. The frequency-response curve of the SVEH is obtained by holding the base acceleration amplitude constant at $A_\circ = 0.05g$, while the frequency is varied in the range 5–35 Hz. The measured frequency-response curve of the open-circuit voltage (RMS) resembles that of a narrow band linear VEH. The peak frequency is located at 21 Hz and the harvesting bandwidth is 1 Hz.

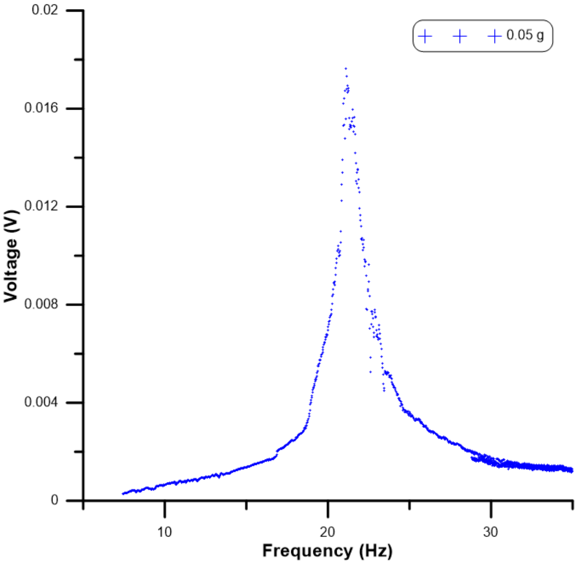

Figure 5.4: The experimental frequency-response curve of the vertical SVEH for input acceleration $A_0 = 0.05$ g

5.2.2 Single-impact Regime: 0.1 g $\leq A_\circ \leq$ 0.5 g

The experimental frequency-response curves of the SVEH open-circuit voltage for base acceleration amplitudes in the range 0.2–0.5 g are shown in Figure 5.5. The figure shows the up- and down-sweeps in the frequency range 5–35 Hz. We note the existence of nonlinear phenomena in this regime, such as hysteresis between the up and down frequency sweeps and jumps between an upper and a lower branch of the frequency-response curves. The size of the hysteretic band increases with base acceleration amplitude from 1 Hz for base acceleration amplitude $A_\circ = 0.2\,\mathrm{g}$ to 3 Hz for $A_\circ = 0.5\,\mathrm{g}$. We note, the reduction in the

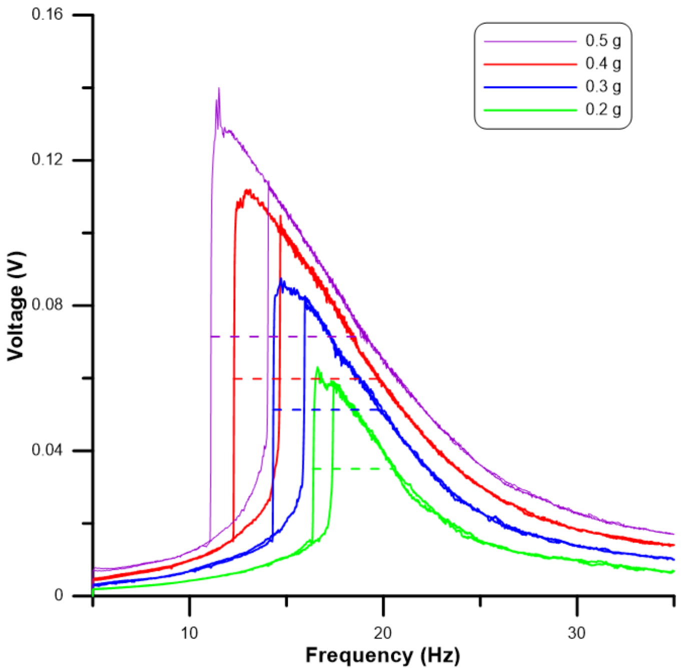

Figure 5.5: The open-circuit frequency-response curves of the vertical SVEH under base acceleration amplitudes in the range of $A_\circ = 0.2$–0.5 g.

harvester's effective stiffness shifts the peak frequency down from $f_c = 21\,\text{Hz}$ the base acceleration amplitude is increased, see Table 5.2. The shift in the peak frequency to the lower values indicates the presence of a softening type nonlinearity due to the flight of the mass unsupported during portion of each cycle of oscillations. As the level of excitations increases and the time the mass spends in flight per cycle increases, the strength of the softening nonlinearity increases.. Meanwhile, the maximum output voltage continues to increase with base acceleration amplitude as expected.

Test results for the 60 turns SVEH were also obtained for the linear and single impact regimes and are shown in Figure 5.2.2. The increase in coil copper volume increased the output voltage of the harvester. For input base amplitude acceleration $A_\circ = 0.4$ g an

Amplitude $A_\circ$ (g)	Peak RMS Voltage (V)	Peak Frequency (Hz)	Bandwidth (Hz)
0.2	0.06	16	4
0.3	0.09	14.3	5.6
0.4	0.12	12.5	6
0.5	0.14	11	8

Table 5.2: SVEH output voltage, peak frequency and bandwidth for base acceleration amplitudes $A_\circ = 0.2, 0.3, 0.4$ and 0.5 g

output voltage of $V = 350$ mV was recorded.

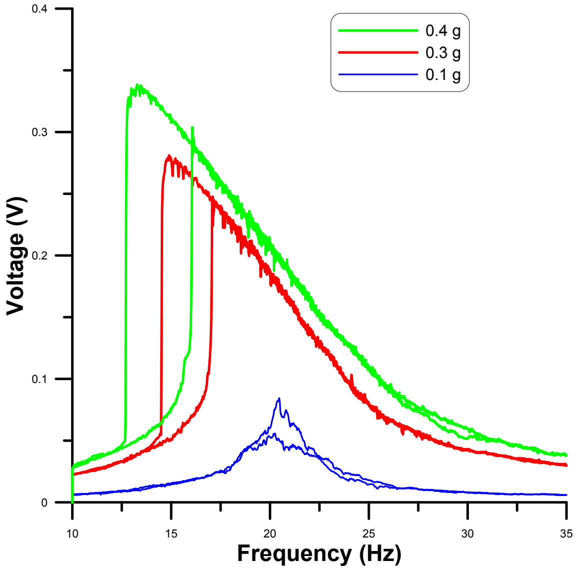

Figure 5.6: The open-circuit frequency-response curve 60 turns SVEH at base acceleration amplitude $A_\circ = 0.1$–0.4 g.

5.2.3 Double-impact Regime: $0.5 < A_\circ$

For large excitations, the base acceleration amplitude was set to values in the range of $A_\circ = 0.6$–1 g. Figure 5.7 shows the frequency-response curves obtained for the open-circuit voltage of the vertical from up and down-sweeps of the frequency range of 5–35 Hz. As in the case of single impact, we note the up and down jumps between a lower an an upper branches of response and hysteretic band limited by those jumps. In addition, a new branch of responses appears in the harvester's frequency-response. Two additional jumps appear to the right (at higher frequency) of the two original jumps in the frequency-response curves leading up to the new branch during frequency down-sweeps and down from it during up-sweeps. For instance, at base acceleration amplitude $A_\circ = 0.8$ g the new jumps occur at

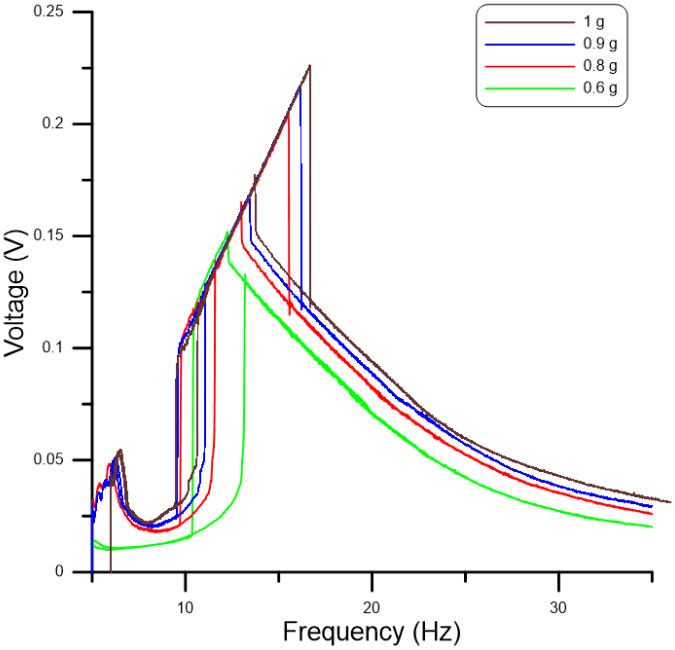

Figure 5.7: Frequency-response curves of the SVEH for base acceleration amplitude in the range of $A_\circ = 0.6$–1 g using a 25 turns coil.

$\omega = 13$ Hz and $\omega_c = 15$ Hz. Along this branch, the vertical SVEH oscillations saturate as noted in the case of the horizontal SVEH resulting in a linear relationship between output voltage and frequency pf excitation regardless of the amplitude of base acceleration.

At low frequencies between 7 and 5 Hz we observe in Figure 5.7 the existence of the superharmonic resonance of order two in response to acceleration amplitude $A_\circ = 0.8$, 0.9, 1.0 g, which is caused by quadratic nonlinearities. This resonance harvest energy at low frequencies.

Frequency response-curves of the 60 turns SVEH at base acceleration amplitudes $A_\circ =$ 0.6–0.8 g are shown in Figure 5.8. Maximum output voltage of $V = 0.5$, 0.75, and 0.9 V are obtained for amplitude accelerations $A_\circ = 0.6$, 0.7, and 0.8 g respectively, otherwise the response is identical to that of the 25 turns SVEH.

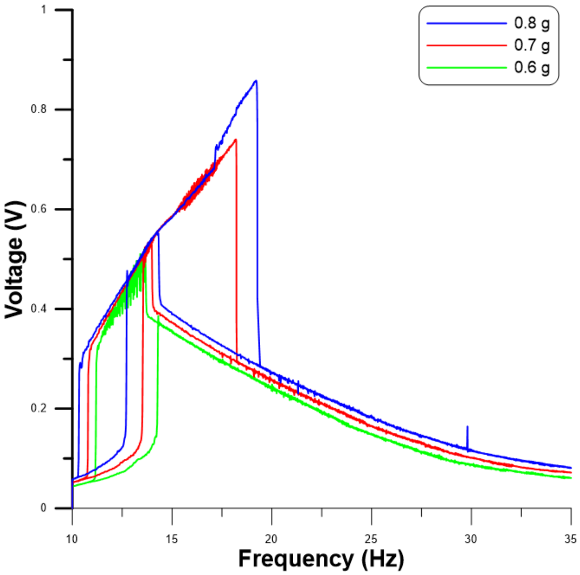

Figure 5.8: Frequency-response curves of the SVEH with 60 turns coil and base acceleration amplitude in the range of $A_\circ = 0.6$–0.8 g

The open-circuit voltage waveforms for the three regimes, shown in Figure 5.9, were obtained experimentally for amplitudes of base acceleration at different frequencies for the 40 turns SVEH. The harvester's waveforms for base acceleration amplitudes $A_0 = 0.05$ g and 0.01 g, Figure 5.9(a) and (b), is harmonic which is typical for linear VEHs. For base acceleration amplitudes in the single-impact regime, the waveform deforms as the excitation level increases, Figure 5.9(c)–(f), to approach a triangular waveform.

5.3 Power Analysis

Optimal power analysis of the SVEH in the three regimes is presented in this section. Base acceleration amplitudes $0.05, 0.4$, and 0.6 g were applied to the harvester with a resistive load R_L connected between the coil terminals. A frequency sweep was then performed on the harvester using different load resistance in order to identify the optimal power and optimal load in each regime.

Figure 5.10 shows the frequency-output power curves of the SVEH in the linear regime for load resistance of $R_L = 5.5$–$40\,\Omega$, and base acceleration and the measured optimal power is 30 μWatts at an optimal load of $R_L = 5.2\ \Omega$.

Figure 5.11 shows the the frequency-output power curve of the 25 turns SVEH for base acceleration amplitude $A_\circ = 0.4$ g to realize the single-impact regime. The measured optimal power in this regime, Figure 5.11, is 2.2 mWatts and the optimal load is $R_L = 2.5\,\Omega$.

Similarly, we measured the optimal power of the harvester in the double-impact regime for base acceleration amplitude $A_\circ = 0.6$ g. The measured optimal power in this regime, Figure 5.12, is 3.5 mWatts and the optimal load is $R_L = 2.5\ \Omega$.

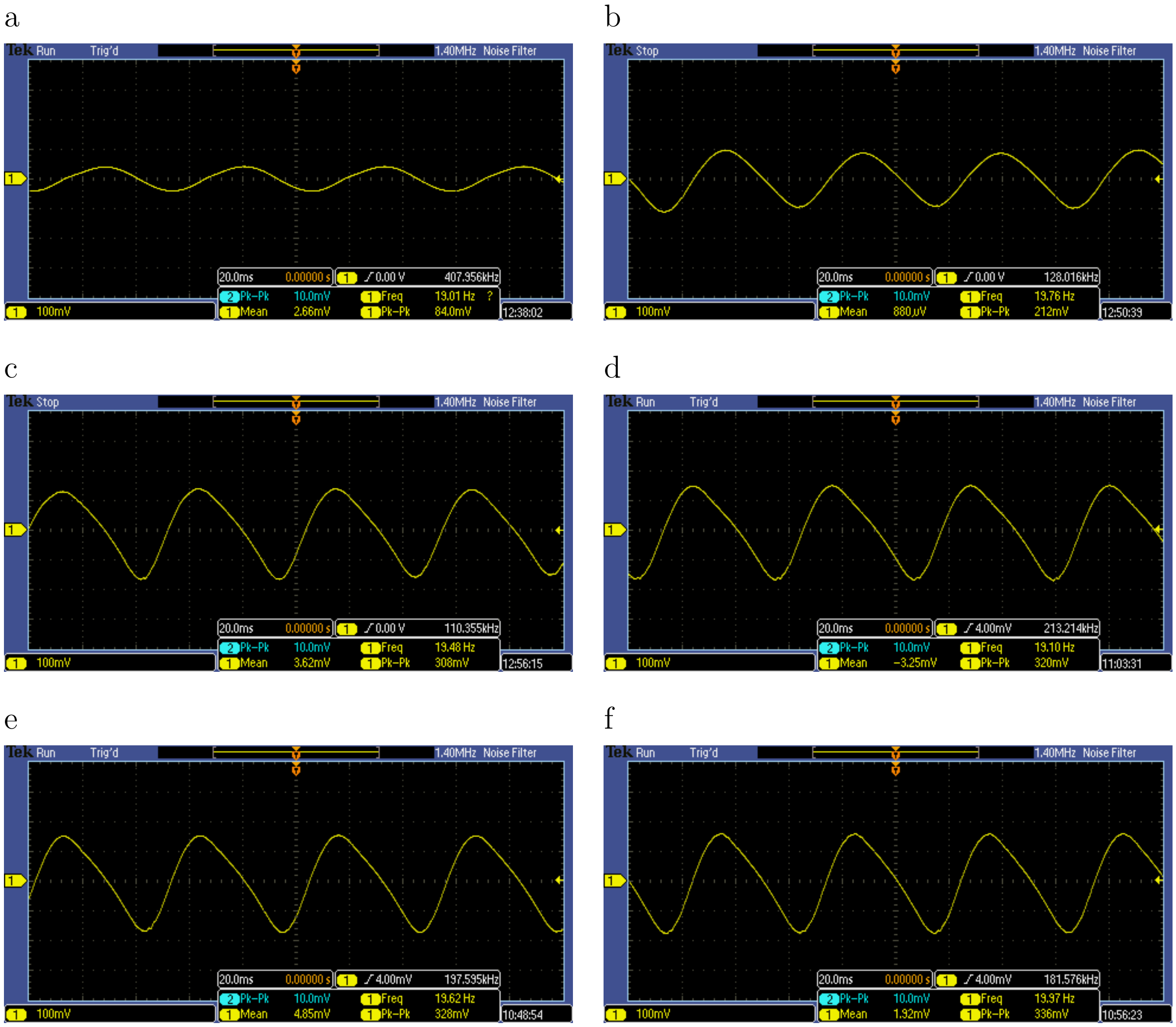

Figure 5.9: 40 turns SVEH Vertical SVEH voltage waveforms for base acceleration amplitudes and frequencies: a) $A_0 = 0.05$ g and $\omega = 19$ Hz, b) $A_0 = 0.1$ g and $\omega = 13.75$ Hz, c) $A_0 = 0.2$ g and $\omega = 19$ Hz, and d) $A_0 = 0.3$ g and $\omega = 13$ Hz, e) $A_0 = 0.4$ g, and f) $A_0 = 0.5$ g.

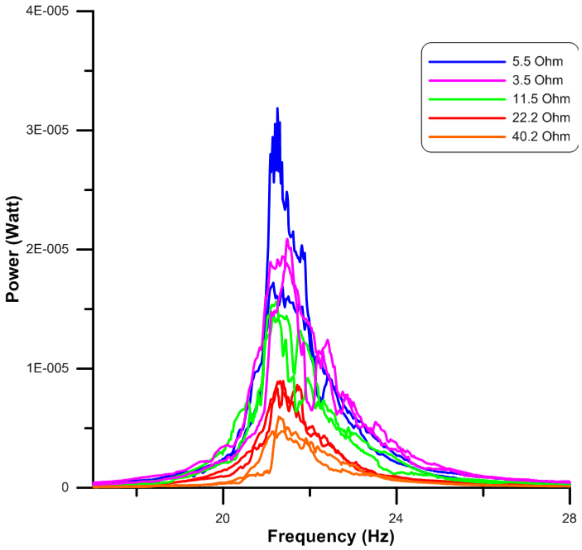

Figure 5.10: Frequency-output power curves for the 25 turns SVEH at base acceleration amplitude $A_\circ = 0.05$ g

5.4 Numerical Results

Applying the shooting method, described in section 4.4 to the vertical SVEH equation of motion, Equation 5.1, we obtain its frequency-response curves numerically and determine

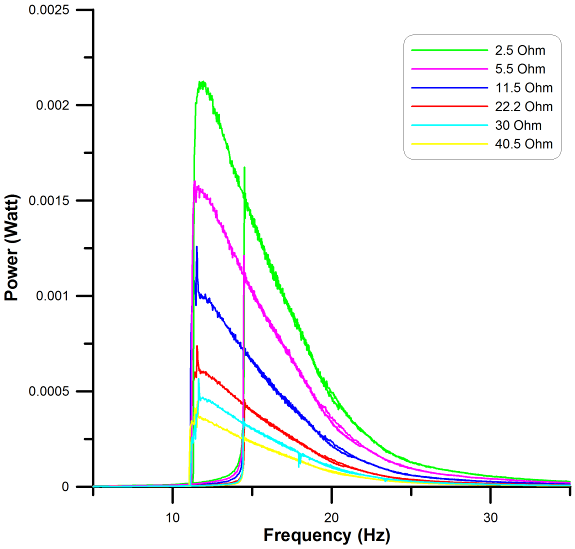

Figure 5.11: Power frequency-response curves of the SVEH with 25 turns coil and amplitude $A_\circ = 0.4$ g

their stability.

$$\begin{aligned}
&\dot{x}_1 = x_2 \\
&\dot{x}_2 = -\frac{c_e + c_m}{m} x_2 - \frac{F_{st}}{m} - \ddot{y} - g \\
&\frac{d}{dt}\frac{\partial x_1}{\partial \eta_1} = \frac{\partial x_2}{\partial \eta_1} \\
&\frac{d}{dt}\frac{\partial x_1}{\partial \eta_2} = \frac{\partial x_2}{\partial \eta_2} \\
&\frac{d}{dt}\frac{\partial x_2}{\partial \eta_1} = -\frac{c_e + c_m}{m}\frac{\partial x_2}{\partial \eta_1} - \frac{1}{m}\frac{\partial F_{st}}{\partial x_1}\frac{\partial x_1}{\partial \eta_1} \\
&\frac{d}{dt}\frac{\partial x_2}{\partial \eta_2} = -\frac{c_e + c_m}{m}\frac{\partial x_2}{\partial \eta_2} - \frac{1}{m}\frac{\partial F_{st}}{\partial x_1}\frac{\partial x_1}{\partial \eta_2} \\
&\mathbf{x}(0) = \eta_0 \\
&\frac{\partial x_1}{\partial \eta_1}(0) = 1,\ \frac{\partial x_1}{\partial \eta_2}(0) = 0,\ \frac{\partial x_2}{\partial \eta_1}(0) = 0,\ \frac{\partial x_2}{\partial \eta_2}(0) = 1
\end{aligned} \tag{5.5}$$

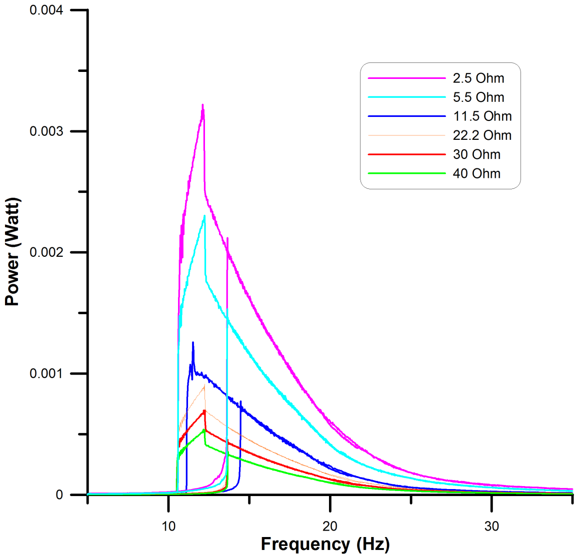

Figure 5.12: Frequency-output power curves of the vertical 25 turns SVEH for base acceleration amplitudes $A_\circ = 0.05$ g

As in the experiments, the range of base acceleration amplitudes was chosen to explore the three identified regimes of the vertical SVEH and the frequency was swept from 10 to 30 Hz.

5.4.1 Linear Regime

In this regime restoring force F_{st} reduces to a linear spring and the equation of motion reduces to:

$$\ddot{x} = -\frac{b_m}{m}\,\dot{x} - \frac{k_1}{m}\,x - \ddot{y} - g \tag{5.6}$$

which can be written as:

$$\ddot{x} + 2\,\zeta\,\omega_n\,\dot{x} + \omega_n^2\,x = -\ddot{y} - g, \tag{5.7}$$

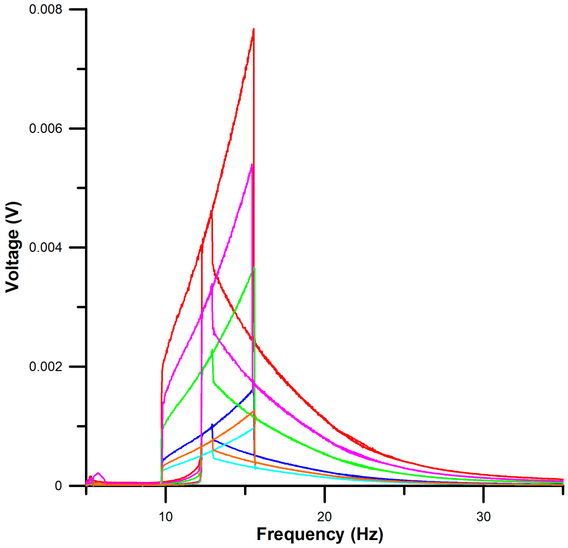

Figure 5.13: Frequency-output power curves of the 25 turns SVEH for base acceleration amplitude $A_\circ = 0.6$ g

The numerical response of the harvester is obtained by substituting the parameter values listed in Table 5.1 into Equation (5.7) and numerically integrating the resulting system. The open circuit output voltage of the SVEH is obtained from Equation (2.11). Numerical and experimental results, Figure 5.14, show the frequency-response curves for base acceleration amplitude $A_\circ = 0.05$ g over the frequency range 5 to 35 Hz. The figures show a good agreement between the experimental and numerical results. The harvester's maximum output open-circuit voltage is 18 mV obtained at the center frequency $f_c = 21\,Hz$ with harvesting bandwidth of 3 Hz.

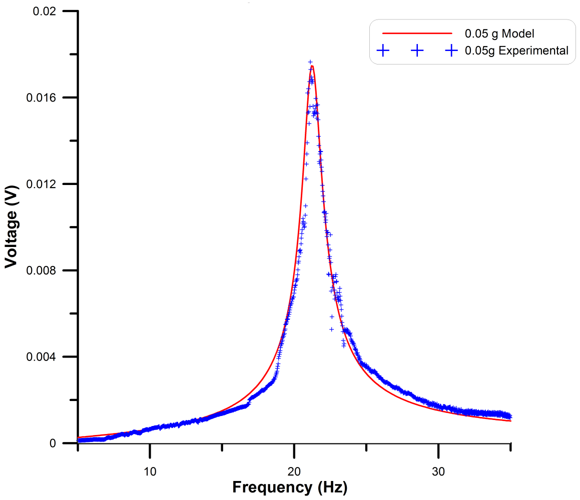

Figure 5.14: Numerical (red line) and experimental (blue +) open circuit voltage (RMS) frequency-response curves for amplitude $A_\circ = 0.05$ g

5.4.2 Single-impact Regime

Figure 5.15 shows the SVEH's experimental and numerical up and down sweeps of the frequency-response for base acceleration amplitude $A_\circ = 0.4$ g. The results obtained numerically compare reasonably well with the experimental results. In this regime, the stiffness was reduced to $k_1 = 880$ N/m, to account for the fraction of period where the mass looses contact with the lower spring thus reducing the effective stiffness of the SVEH. Unlike the linear regime, the response of the SVEh in the single impact regime is nonlinear demonstrating multi-valued and unstable responses. In this subsection we focus on the stability of periodic solutions obtained above for the impact regime 2.

Figure 5.16 shows the complete frequency-response curves of the SVEH for base acceleration amplitudes $A_\circ = 0.1$, 0.3, and 0.5 g. The solid and dashed lines represent the stable and unstable branches respectively. We observe that for higher base acceleration

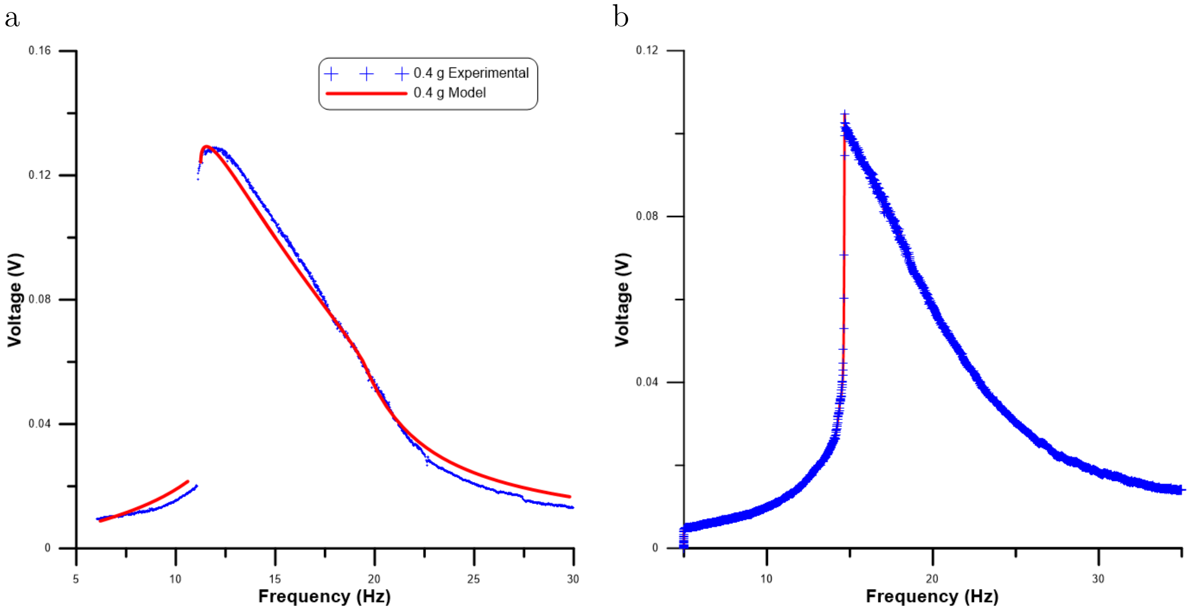

Figure 5.15: Vertical configuration up- and down-sweep frequency-response curves for input acceleration amplitude $A_\circ = 0.4$ g and different frequencies : a) up-sweep, b) down-sweep

amplitudes, the frequency-response curve consists of three branches: a lower stable branch running from A to A', an unstable branch from A' to B', and an upper stable branch from B' to B. The lower stable branch corresponds to low energy harvesting, where the mass does not lose contact with the lower spring, while the upper stable branch corresponds to higher energy harvesting where the mass takes flight.

The stable lower branch meets an unstable branch in a CF bifurcation point at A'. At the second CF bifurcation point B', the unstable branch meets the upper stable branch. Figure 5.17 shows the corresponding Floquet multipliers of the stable and unstable branches. The Floquet multipliers of the unstable branch $A' - B'$ lie outside the unit circle, while those corresponding the stable branches $A - A'$ and $B' - B$ remain inside the unit circle.

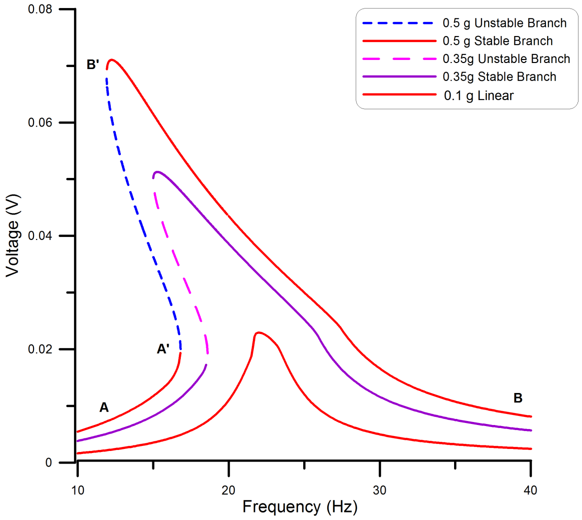

Figure 5.16: The open circuit voltage of the 60 turns SVEH for base acceleration amplitudes $A_\circ = 0.1$, 0.3, and 0.5 g.

From the bifurcation analysis we, conclude that the sweet spot for energy harvesting is along the upper stable branch from point B'. However, frequencies close to B' in the case of the vertical harvester frequencies close to the upper CF bifurcation point must be avoided in order to maximize the harvested energy.

5.5 Summary

The vertical SVEH was investigated numerically and experimentally in this chapter. The results show that the vertical SVEH possess three regions of operations, linear, sing-impact, and double-impact. In the linear regime the response of the harvester is that of a forced, damped, single degree of freedom oscillator under base excitation. The performance of the harvester in this regime ($A_\circ < 0.5$ g) is not desirable since its bandwidth is narrow and

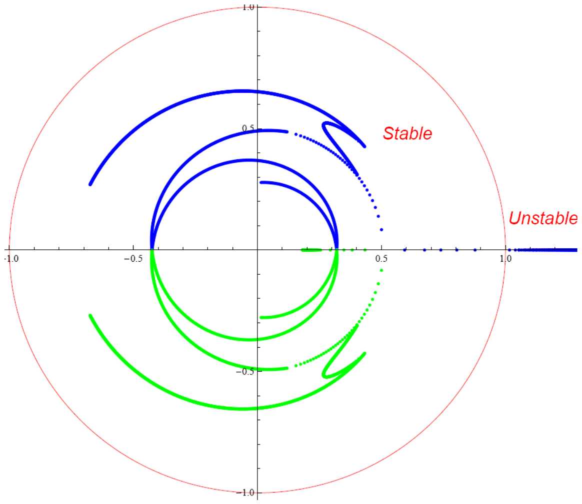

Figure 5.17: Floquet multipliers corresponding to the SVEH frequency-response for base amplitude acceleration $A_\circ = 0.5$ g

output power is low. In the single-impact regime, the harvester's frequency-response curve exhibits the nonlinear phenomena typical of impact oscillators including a shift of the peak frequency as the amplitude of base acceleration in increased, indicating a softening type nonlinearity. This softening allows for energy harvesting from low frequency vibrations. The numerical analysis performed on the model show very close match between numerical and experimental results for the linear and single-impact regimes. Bifurcation analysis shows the existence of cyclic-fold bifurcations that cause the harvester's output voltage to suddenly drop from large impacting orbits to small non-impacting orbits. The desirable operation range of the vertical SVEH in the single-impact regime lies along the resonant impacting branch, while remaining away from the upper CF bifurcation.

Chapter 6

Other Prototypes and Model Pitfalls

Many prototypes of the SVEH were designed, built, and analyzed. The prototypes' designs differed in a number of ways, but the features of the harvester that made significant change to the harvester's performance was the type of coil used in the electromagnetic transducer and the magnetic circuit. One of the prototypes used a distributed PCB coil, its performance was very poor, in particular the low output voltage. The poor performance of this prototype prompted the design of the prototype presented in previous chapters.

In this chapter we present experimental results of the prototype with the distributed coil to show the shortcomings of using such coil. The experimental results are analyzed, discussed, and conclusions are made.

6.1 Distributed Coil

The prototype of the SVEH investigated here is similar to the one analyzed and discussed in the previous chapters, with the exception of the electromagnetic transducer. The trans-

Table 6.1: Magnet Specifications

Dimensions (mm)	25.4 x 6.35 x 1.588
Material	Sintered Neodymium
Weight	4 gr
Surface Field (B)	12600 Gauss

ducer used a PCB coil and a weak magnetic circuit shown in Figure 6.1. The coil used is a double-sided PCB coil distributed along the track of the harvester, while the magnetic circuit used thin and magnets separated by an air gap equal in length to the magnet's width. The interaction between the coil and the magnetic field is of great significance in vibration energy harvesting. The greater the interaction between the coil and the magnets the greater the harvested energy. Analysis of the magnetic circuit discussed in the next subsection reveal some interesting results that explain why the prototype with distributed coil performed so poorly.

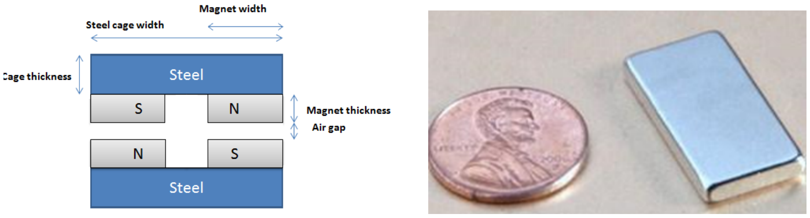

Figure 6.1: Magnetic circuit of harvester prototype with distributed coil

6.1.1 Magnetic Circuit Analysis

A model of the SVEH magnetic circuit, shown in Figure 6.1, is developed and simulated using ANSYS. The model consists of permanent magnets with dimensions listed in Table

6.1, a steel cage, an air gap between the magnets, an air gap separating the upper and lower plates of the steel cage, and the air region surrounding the cage. Similarly, the boundaries were set at five times the cage thickness to count for any stray magnetic field lines. The relative permeability of air, steel, and permanent magnets were set to $\mu_a = 1$, $\mu_s = 4000$, and $\mu_m = 1$, respectively. A top view of the simulated magnetic flux density within the cage is shown in Figure 6.1.1

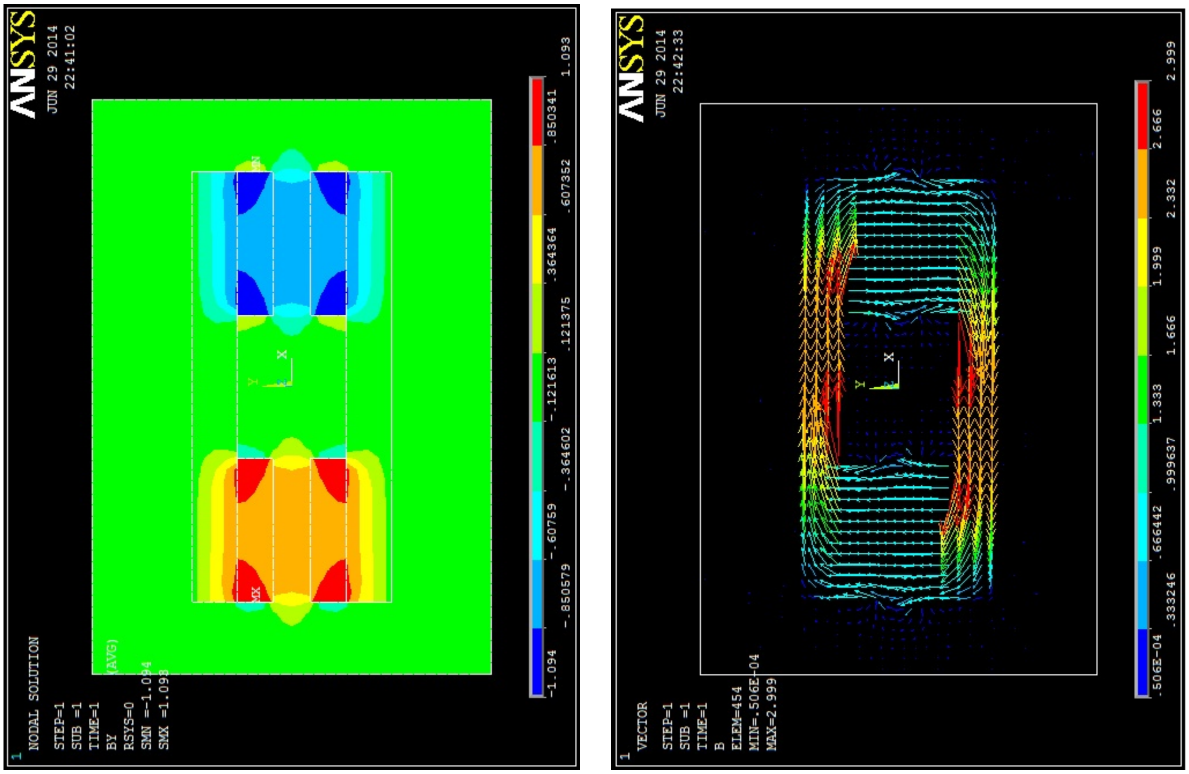

Figure 6.2: Distributed coil SVEH simulated magnetic field flux density and flux lines

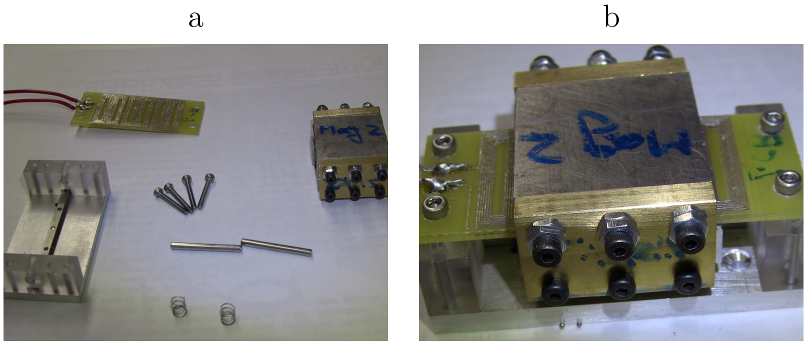

Figure 6.3: PCB harvester, a: harvesters components and b: built prototype

6.2 Experimental Results

In this section we present the experimental results of the first prototype in the vertical and horizontal configurations. Testing of the VEH was conducted using an electromagnetic shaker unit with accelerometer feedback which provide excitations with amplitudes and frequencies that are suitable for our studies. Measurements of SVEH output is done using VibrationView software that allows tests over a range of acceleration levels and frequencies.

6.2.1 Vertical Configuration

In the vertical configuration the harvester is aligned vertically as shown in Figure 6.4. A base acceleration is applied to the housing unit as base excitation and the output voltage across the harvester's coil terminals is measured using VibrationView.

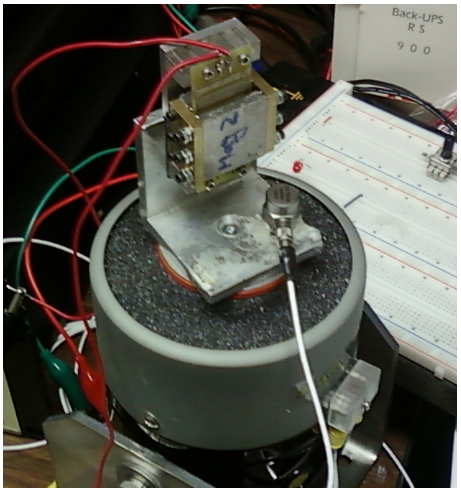

Figure 6.4: Vertical VEH experimental setup

Linear Regime: $(A_\circ \leq 0.05\,g)$

The SVEH linear regime is tested by applying a constant low base acceleration amplitude, $A_\circ = 0.03g$, while the frequency is swept up and down in the range 12 to 30 Hz. In this regime, the seismic mass remains in contact with the lower spring and oscillates when subjected to low harmonic input acceleration amplitudes. The test results show that the response of the SVEH is linear with the output voltage peaking at resonance frequency $\omega \approx 16$ Hz. Figure 6.5 shows the measured frequency-response curves of the voltage (RMS) across the open circuit terminals of the coil.

Single-impact Regime: $(0.05\,g < A_\circ < 0.5\,g)$

The experimental frequency-response curves of the voltage across the open circuit terminals of the coil for base acceleration amplitudes in the range 0.2 to 0.5 g are shown in Figure 6.6. The figure shows the up- and down-sweeps in the frequency range $5-35$ Hz. The test

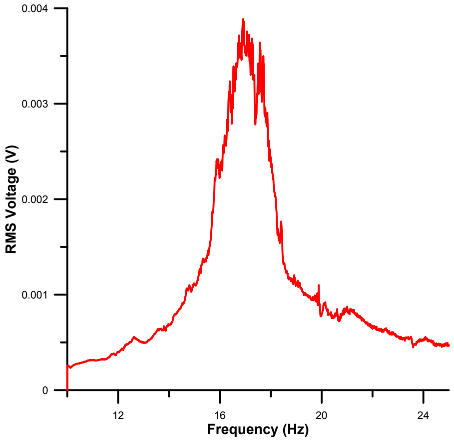

Figure 6.5: Distributed coil SVEH linear regime frequency-response

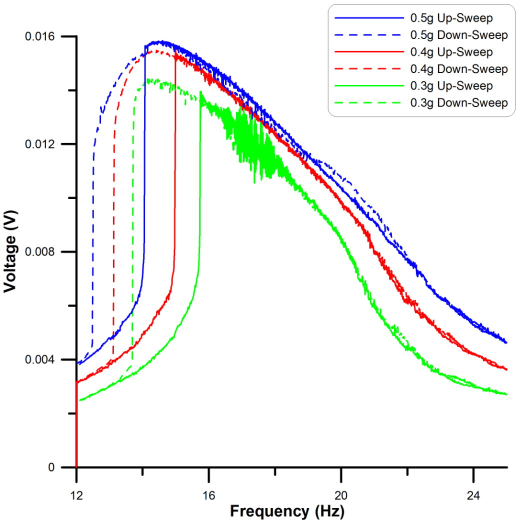

Figure 6.6: Distributed coil SVEH single-impact regime frequency-response

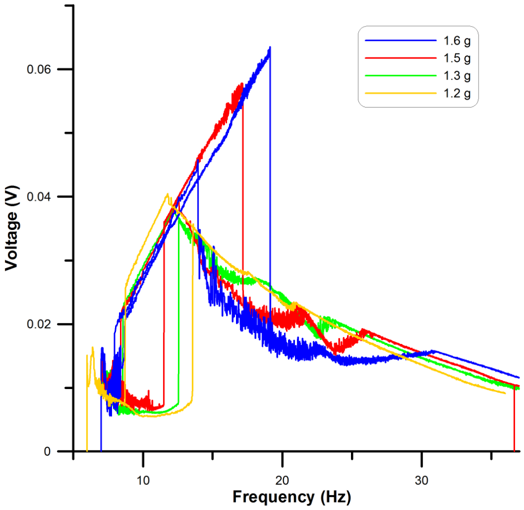

Figure 6.7: Distributed coil SVEH double-impact regime frequency-response

results of single-impact VEH shown in Figure 6.6 represent the open-load output voltage of the harvester. We note that the maximum output voltage of the harvester for an input acceleration $A_0 = 0.5$ g is 16 mV.

Double-impact Regime: $(A_o > 0.5\,g)$

For large excitations, the base acceleration amplitude was set to the range of $A_\circ = 0.6 - 1$ g. Figure 6.7 shows the frequency-response curves obtained for the open-circuit output voltage of the VEH. As the base acceleration amplitude is increased beyond 0.5 g, te seismic mass engages the two springs resulting in a double-impact oscillator that caused the output voltage to increase slightly and attains a peak value of 60 mV for an base acceleration amplitude $A_0 = 1.6$ g, which is quite high for an ambient vibration.

6.2.2 Horizontal Configuration

The SVEH is mounted on an electromagnetic shaker as shown in Figure 6.8, and a base acceleration is applied as input excitation with amplitude A_o and frequency Ω. The test was conducted by applying a frequency-sweep of ω in the range $3\,Hz$ and $12\,Hz$ while holding the amplitude of base acceleration constant $A_\circ$. The VEH was tested for the following base acceleration amplitudes: $A_\circ = 0.1$ to $0.4\,\mathrm{g}$ in $0.1\,\mathrm{g}$ increments. Figure 6.9 shows the frequency-response curves of the RMS voltage for up- and down-sweeps of the different base accelerations. Test results shown in Figure 6.9 show that the output voltage of the VEH vary between $5\,\mathrm{mV}$ and $25\,\mathrm{mV}$ for input accelerations varying between $0.1\,\mathrm{g}$ and $0.4\,\mathrm{g}$.

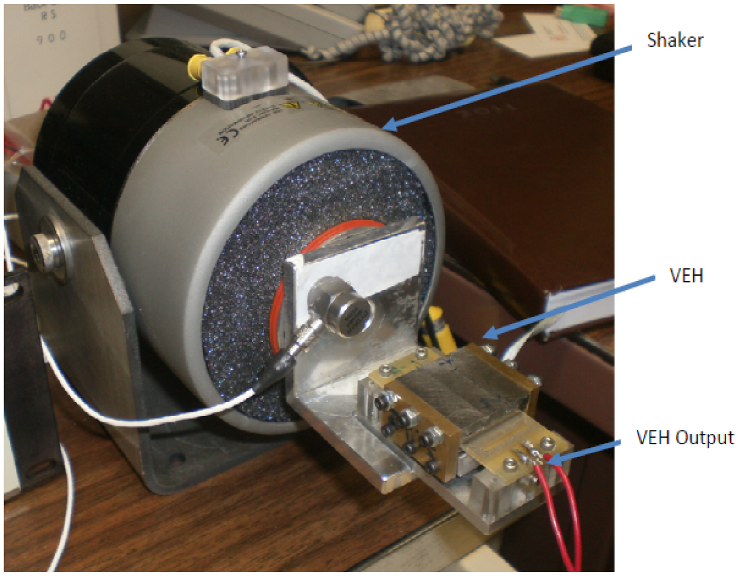

Figure 6.8: Test Setup

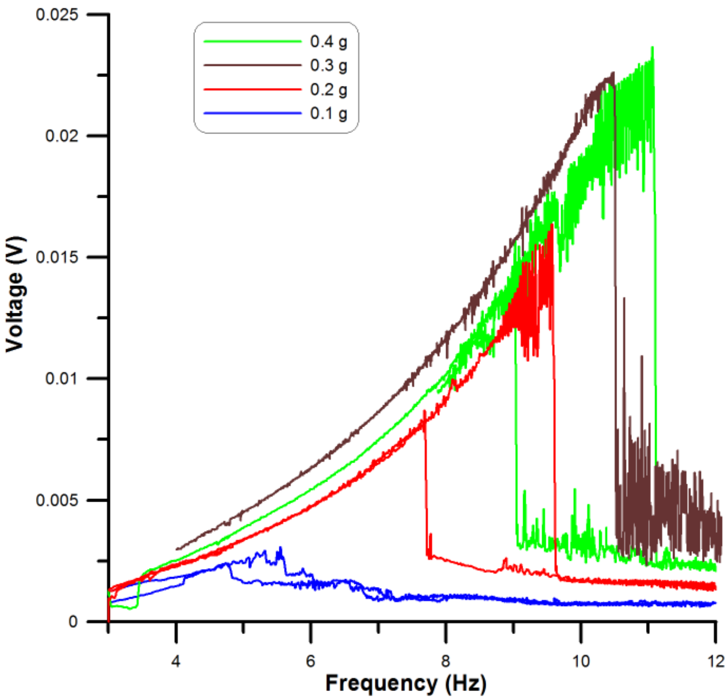

Figure 6.9: Frequency-response of the SVEH open-circuit voltage for base acceleration amplitudes of $A_0 = 0.1 - 0.4$ g and a distributed coil with length $l = 1.75$ m

6.3 Summary

The experimental results of the SVEH prototype with a distributed coil, in either the vertical and horizontal configurations, show that the harvester's output voltage is way too low. The maximum output voltage of approximately 50 mV was obtained from a base acceleration amplitude $A_\circ = 1.6$ g. On the one hand, this output voltage is very low for most applications and for power conditioning. On the other hand, it is not easy to find environmental vibration greater than 1 g. This proves that there are certain flaws in the initial design that need to be identified and addressed.

We observe from the ANSYS model of magnetic flux density, Figure 6.1.1, a wide area where the flux density is essentially zero. This means that a portion of the PCB coil will always be outside the magnetic field, reducing the effective length of the coil. And since the coil is distributed along the length of the harvester, voltage will only be induced in the part of the coil where the magnetic field is active, reducing the effective coil length even further. Since the electromagnetic force F_{em} across the coil is proportional to the effective length of the coil, this means that the lower the effective length of the coil the lower the harvested energy. This limitations prompted the redesign the harvester's coil and the magnetic circuit in order to ensure that there are no gaps where the magnetic field is low, and ensure that the entire coil remains inside the magnetic field. These two fundamental changes in the design of the magnetic circuit and the geometry of the coil resulted in a significant increase in the harvester's performance presented in the earlier chapter.

Chapter 7

Conclusions and Future Work

7.1 Conclusions

In this thesis we studied the dynamics of a new architecture of an electromagnetic vibration energy harvester, the springless VEH. We developed models of the harvester in two configurations, vertical and horizontal, and investigated their response with respect to change in the base acceleration amplitude and frequency.

We tested the vertical VEH experimentally and found that its response contains three distinct regions of operation depending on the amplitude and frequency of base accelerations. For low gs ($A_\circ \leq 0.1$ g) the response of the SVEH is linear, and for moderate ($A_\circ \leq 0.5$ g) and high ($A_\circ > 0.5$ g) base acceleration amplitudes, we observed a consistent bending of the frequency-response curves of the coil RMS voltage to the left indicating an effective softening-type nonlinearity. The softening nonlinearity appears due to the fact that the effective stiffness of the system is reduced since the seismic mass spends a certain amount of time traveling in the air between the two springs. Further, for high gs, the spring-type end-limiters were found to saturate the realizable output voltage to a maximum proportional to the track length but allow for a much wider energy harvesting bandwidth as the base excitations amplitude increases. The softening nonlinearity found in this configuration was observed numerically and experimentally. This softening effect shifted the harvester's center frequency, when in operating in the linear region, from $\omega = 21$ Hz to about 11 Hz when operating in the single-impact mode. In the third regime the frequency shifted further to the left and the a new phenomena were observed. The harvester RMS output voltage peaked at base acceleration frequency $\omega \approx 5$ Hz, indicating the existence of subharmonic resonance. And the emergence of a new branch where the output voltage increases linearly with the base acceleration frequency. These characteristics of the harvester show that in the vertical configuration, the harvester can harvest environmental vibrations with frequencies as low as 5 Hz. The maximum power that was achieved by the harvester in this configuration was 5 mW. The nonlinearities in the harvester enhanced frequency bandwidth of the harvester when compared with the linear harvester.

By contrast, analysis of the horizontal springless vibration energy harvester showed different behavior than that of the vertical configuration. From experimental, as well as numerical results, we observed a consistent bending of the frequency-response curves of the harvester output voltage to the right indicating an effective hardening-type nonlinearity and more bandwidth. A maximum output voltage of 1 V and an output power of 10 mW were achieved from base acceleration amplitudes of 0.5 g. The harvesting bandwidth of the horizontal configuration was $BW = 8$ Hz.

In terms of energy harvested, the horizontal configuration proved to be more efficient as the output power was more than twice that of the vertical configuration.

7.2 Future Work

Besides the challenges still facing vibration energy harvesters mentioned in this thesis, another difficulty is power density and the harvester size. We intend to use the lessons learned from this work to design a miniaturized version of the harvester by reducing its weight and introducing a new type of stiffness mechanism to avoid the misalignment of the springs. One option to do this is to look for MEMS technology and use it to fabricate a magnetic harvester with impact.

On the modeling side, there are few issues that need to be ironed out. Validation of the horizontal model needs to be revised in order to obtain a good match between experimental and numerical results. The least squares method used to identify the model parameters is suited for smooth systems, a more robust technique, that can handle nonsmooth systems, will be sought to improve parameter estimation of the harvester model.

References

[1] M. Mateu and F. Moll. Review of energy harvesting techniques and applications for microelectronics. volume 5837, pages 359–373, June 2005.

[2] S. P. Beeby, R. N. Torah, M. J. Tudor, P. Glynne-Jones, T. O'Donnell, C. R. Saha, and S. Roy. A micro electromagnetic generator for vibration energy harvesting. *Journal of Micromechanics and Microengineering*, 17(7):1257–1265, Jul 2007.

[3] B. P. Mann and N. D. Sims. Energy harvesting from the nonlinear oscillations of magnetic levitation. *Journal of Sound and Vibration*, 319:515–530, 2009.

[4] V. R. Challa, M. G. Prasad, and F. T. Fisher. Towards an autonomous self-tuning vibration energy harvesting device for wireless sensor network applications. *Smart Materials and Structures*, 20(2):1–12, Feb 2011.

[5] J. Ding, V. R. Challa, M. G. Prasad, and F. T. Fisher. *Vibration Energy Harvesting and Its Application for Nano-and Microrobotics. In Selected Topics in Micro/Nano-robotics for Biomedical Applications.* Springer New York, 2013.

[6] S. P. Beeby, M. J. Tudor, and N. M. White. Energy harvesting vibration sources for microsystems applications. *Measurement Science and Technology*, 17(12):R175–R195, Dec 2006.

[7] R. J. M. Vullers, R. van Schaijk, I. Doms, C. Van Hoof, and R. Mertens. Micropower energy harvesting. *Solid-State Electronics*, 53(7):684–693, July 2009.

[8] H. Vocca and F. Cottone. *Kinetic Energy Harvesting.* 2014.

[9] DP Arnold. Review of microscale magnetic power generation. *Magnetics, IEEE Transactions on*, 43:3940–3951, 2007.

[10] Battery Recycling in Canada 2009 Update - Executive Summary. Website, 2009. `http://www.ec.gc.ca/gdd-mw/default.asp?lang=En&n=52DF915F-1&offset=1&toc=show`.

[11] D. Zhu and S. Beeby. *Energy Harvesting Systems.* Springer, 2011.

[12] A. Cammarano, S. G. Burrow, and D. A. W. Barton, editors. *An Energy Harvester With Bistable Compliance Characteristics.* ASME-DETC2010-29222, ASME, 2010.

[13] T. Lihua, Y. Yaowen, and C. K. Soh. *Broadband Vibration Energy Harvesting Techniques.* Springer, 2013.

[14] Z. Hadas, M. Kluge, V. Singule, and C. Ondrusek. Electromagnetic vibration power generator. *Micromechanics and Microengineering*, 18(11):451–455, Feb 2007.

[15] S. Priya and T. D. Inman. *Energy Harvesting Technologies.* Springer, 2009.

[16] N. Fondevilla, C. Serre, M. Acero, J. Esteve, and J. Morante. Electromagnetic Harvester Device for Scavenging Ambient Mechanical Energy With Slow, Variable, and Randomness Nature . *PowerMEMS 2009*, pages 225–228, Dec 2009.

[17] S. C. Stanton, C. C. McGehee, and B. P. Mann. Nonlinear dynamics for broadband energy harvesting: Investigation of a bistable piezoelectric inertial generator. *Physica D: Nonlinear Phenomena*, 239(10):640–653, May 2010.

[18] F. Balouchi and C. Wheelock. EXECUTIVE SUMMARY : Energy Harvesting Thermoelectric Technologies for Consumer and Industrial Applications : Market Analysis and Forecasts. 2011.

[19] P. Wright. Energy Scavenging / Harvesting. 2006.

[20] M. Soliman, E. Abdel-Rahman, E. F. El-Saadany, and R. R. Mansour. A Design Procedure for Wideband Micropower Generators. *Journal of Microelectromechanical Systems*, 18(6):1288–1299, Dec 2009.

[21] M. Soliman. *Wideband Micro-Power Generators for Vibration Energy Harvesting.* Thesis, University of Waterloo, 2009.

[22] F. Lu, H. P. Lee, and S. P. Lim. Modeling and analysis of micro piezoelectric power generators for micro-electromechanical-systems applications. *Smart Materials and Structures*, 13(1):57–63, Feb 2004.

[23] P. D. Mitcheson and E. M. Yeatman. Arcitectures for vibration-driven micropower generators. *Journal of Microelectromechanical Systems*, 13:1457–1486, June 2004.

[24] S. Roundy. On the Effectiveness of Vibration-based Energy Harvesting. *Journal of Intelligent Material Systems and Structures*, 16(10):809–823, 2005.

[25] D. Guyomar and M. Lallart. Recent progress in piezoelectric conversion and energy harvesting using nonlinear electronic interfaces and issues in small scale implementation. *Micromachines*, 2:274–294, 2011.

[26] M. Mahmoud and E. Abdel-Rahmany. Battery-less electrostatic micro-power generator. *IEEEXplore*, pages 29–32, 2009.

[27] M. A. Mahmoud, E. F. El-Saadany, R. R. Mansour, and E. M. Abdel-Rahman. Springless vibration energy harvesters. volume 1, pages 451–455. ASME, June 2010. Paper number DETC2010-29046.

[28] A. M. Karami and D. Inmann. Powering pacemakers from heartbeat vibrations using linear and nonlinear energy harvesters. *Applied Physics Letters*, 2012.

[29] Innovative Energy Harvesting. Website, 2011. `http://eh-network.org/events/dissemination2011/pitches/Arveni.pdf`.

[30] Self sustaining power faucet. Website. `http://www.chicagofaucets.com/catalog/catalog.php?name=Our%20Products&part_number=116.211.AB.1`.

[31] Micro-Energy Cells. Website, 2012. `http://www.infinitepowersolutions.com/products/thinergy.html`.

[32] ECO 200 Vibration Energy Harvester. Website, 2009. `http://www.enocean.com/eco200-ptm330/`.

[33] `http://www.kinetron.eu/micro-generator-technology/`.

[34] `https://www.enocean.com/en/enocean_modules_902mhz/eco-200/`.

[35] `http://www.perpetuum.com/products/vibration-energy-harvester.asp`.

[36] C. Cepnik, O. Radler, S. Rosenbaum, T. Ströhla, and U. Wallrabe. Effective optimization of electromagnetic energy harvesters through direct computation of the electromagnetic coupling. *Sensors and Actuators A: Physical*, 167(2):416–421, 2011.

[37] M. S. Soliman, E. Abdel-Rahman, El-Saadany E., and Mansour R. R. A wide-band vibration-based energy harvester. *Micromechanics and Microengineering*, 18(11):1257–1265, Feb 2008.

[38] C. B. Williams and R. B. Yates. Analysis of a micro-electric generator for microsystems. *Sensors and Actuators*, 52:8–11, 1996.

[39] P. Glynne-Jones. *Vibration powered generators for self-powered microsystems.* Phd thesis, University of Southampton, Southampton, England, 2001.

[40] S. Roundy and P. K. Wright. A piezoelectric vibration based generator for wireless electronics. *Smart Materials and Structures*, 13(5):1131, 2004.

[41] N. H. Ching, H. Y. Wong, W. J. Li, P. H. W. Leong, and Z. Wen. A laser-micromachined multi-modal resonating power transducer for wireless sensing systems. *Sensors and Actuators A: Physical*, 97-98:685–690, Apr 2002.

[42] L. Tang, Y. Yang, and C. K. Soh. Toward broadband vibration-based energy harvesting. *Journal of Intelligent Material Systems and Structures*, 21:1876–1897, 2010.

[43] L. P. Green. *Nonlinear Energy Harvesting.* Phd thesis, University of Sheffield, Sheffield, England, October 2012.

[44] D. Zhu, M. J. Tudor, and S. P. Beeby. Strategies for increasing the operating frequency range of vibration energy harvesters: a review. *Journal of Measurement Science and Technolgy*, 21, Dec 2009.

[45] K. Seong-Il, L. Dong Ho, L. Yoon Pyo, C. Young Soo, and P. Min-Chul. Low frequency properties of micro power generator using a gold electroplated coil and magnet. *Applied Physics*, 8(2):138–141, March 2008.

[46] M. Rezaeisary, M. El Gowini, D. Sameoto, D. Raboud, and W. Moussa. Wide-bandwidth piezoelectric energy harvester with polymeric structure. *Micromechanics and Microengineering*, 25, 2004.

[47] W. Zhang and K.L. Turner. Nonlinear dynamics of micro impact oscillators in high frequency mems switch application. *Solid-State Sensors and Actuators*, 1:768–771, 2005.

[48] S. N. Duy and H. Einar. Wideband mems energy harvester driven by colored noise. *Microelectromechanical Systems*, 22(4):R175–R195, 2013.

[49] Duy S. N. and Einar H. Analysis of Vibration Energy Harvesters Utilizing s Variety of Nonlinear Springs. 2010. Unpublished.

[50] R. Harne and K. Wang. A Review of the Recent Research on Vibration Energy Harvesting Via Bistable Systems. *Smart Material and Structures*, 22, 2008.

[51] *Vibration energy harvesters with non-linear compliance*, volume 6928, 2008.

[52] B. P. Mann and B. A. Owens. Investigations of a nonlinear energy harvester with a bistable potential well. *Sound and Vibration*, 329(9):1215–1226, Apr 2010.

[53] R. Ramlan, M. J. Brennan, and I. Kovacic. Potential benefits of nonlinear stiffness in an energy harvesting device. *Journal of Nonlinear Dynamics*, 59:554–558, 2010.

[54] M. F. Daqaq, R. Masana, A. Erturk, and D. Dane Quinn. On the Role of Nonlinearities in Vibratory Energy Harvesting: A Critical Review and Discussion. *Applied Mechanics Reviews*, 66(4):040801, May 2014.

[55] E. Jacquelin, S. Adhikari, and M. Friswell. A piezoelectric device for impact energy harvesting. *Journal of Smart Materials and Structures*, 20:1–12, 2011.

[56] L. Dhakar, H. Liu, F. E. H. Tay, and C. Lee. Sensors and Actuators A : Physical A new energy harvester design for high power output at low frequencies. *Sensors & Actuators: A. Physical*, 199:344–352, 2013.

[57] I. Lien and Y. Shu. Array of piezoelectric energy harvesting by equivalent impedance approach. *Smart Material and Structures*, 21, 2012.

[58] J. Twiefel and H. Westermann. Survey on broadband techniques for vibration energy harvesting. *Journal of Intelligent Material Systems and Structures*, 24:1291–1302, 2013.

[59] I. Sari, T. Balkan, and H. Kulah. An electromagnetic micro power generator for wideband environmental vibrations. *Micromechanics and Microengineering*, 146:405–413, 2008.

[60] B. Yang, C. Lee, X. Xiang, X Xie, J. Han He, R. K Kotlanka, S. P. Low, and H Feng. Electromagnetic energy harvesting from vibrations of multiple frequencies. *Journal of Micromechanics and Microengineering*, 19(3):035001, 2009.

[61] S. W. Shaw and P. J. Holmes. A periodically forced piecewise linear oscillator. *Sound and Vibration*, 60:129–155, 1983.

[62] Y. Zhu. *Design and Development of Broadband Vibration-based Energy Harvester Through Buckled-beam Configuration.* Phd thesis, University of Toronto, Toronto, Canada, 2014.

[63] A. H. Nayfeh. *Introduction to perturbation techniques.* Wiley Classic Library, 1993.

[64] `http://www.labworks-inc.com/all_products/shakers/modal_test/mt_160.htm`.

[65] Vibration Research. *VibrationView Quick Start Guide.*

[66] `http://www.dytran.com/Model-3055B2-General-Purpose-Accelerometer-P2185.aspx`.

[67] S. J. Elliott and M. Zilletti. Scaling of electromagnetic transducers for shunt damping and energy harvesting. *Journal of Sound and Vibration*, 333(8):2185–2195, April 2014.

[68] M. Yilmaz, B. Tunkar, S. Park, K. Elrayes, A. E. M. E. Mahmoud, E Abdel-Rahman, and M. Yavuz. Energy harvesting vibration sources for microsystems applications. *Measurement Science and Technology*, 17(12):R175–R195, Dec 2006.

[69] A. Nayfeh and D. Mook. *Nonlinear Oscillations.* John Wiley and Sons, 1997.

[70] M. J. Feigenbaum. Quantitive universality for a class of nolinear transformations. *Statistical Physics*, 19(1), 1978.

[71] E. J. Doedel, A. R. Champneys, Y. A Kuznetsov, B Sandstede, and X. J Wang. Auto97: Continuation and bifurcation software for ordinary differential equations, user's guide.

[72] J. M. T. Thompson, A. R. Bokaian, and R. Ghaffari. Subharmonic resonances and chaotic motions of a bilinear oscillator. *Applied Mathematics*, 31:207–234, 1983.

[73] A. H. Nayfah and B. Balachandran. *Applied Nonlinear Dynamics: Analytical, Computational, and Experimental Methods.* John Wiley, 1997.

[74] A. H. Nayfah. *Problems in Perturbation.* John Wiley, 1985.

[75] S. Nguyen, G. Halvorson, and G. Jensen. Simple open-loop power conditioning for vibration energy harvesters. *Microelectromechanical Systems*, 22, 2013.

[76] Executive Summary: Energy Harvesting. Website, 2011. `http://solpowerpeople.com/wp-content/uploads/2012/01/Pike-EHARV-11-Executive-Summary1.pdf`.